DAY TO DAY AND LONGITUDINAL VARIABILITY OF THE NIGHTTIME LOW LATITUDE TERRESTRIAL IONOSPHERE

by

Sarah E. McDonald
A Dissertation
Submitted to the
Graduate Faculty
of
George Mason University
in Partial Fulfillment of
The Requirements for the Degree
of
Doctor of Philosophy
Computational Sciences and Informatics

Committee:

	Dr. Michael Summers, Dissertation Director
	Dr. Peter Becker, Committee Member
	Dr. Kenneth Dymond, Committee Member
	Dr. James Gentle, Committee Member
	Dr. Robert Meier, Committee Member
	Dr. John Wallin, Committee Member
	Dr. Dimitrios Papaconstantopoulos, Department Chairperson
	Dr. Peter Becker, Associate Dean for Graduate Studies, College of Science
	Dr. Vikas Chandhoke, Dean, College of Science

Date: 11/14/2007
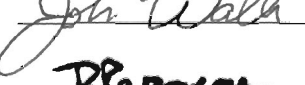
Fall Semester 2007
George Mason University
Fairfax, VA
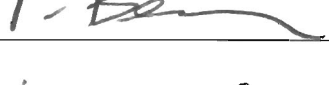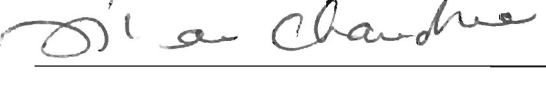
Day to Day and Longitudinal Variability of the Nighttime Low Latitude Terrestrial Ionosphere

A dissertation submitted in partial fulfillment of the requirements for the degree of Doctor of Philosophy at George Mason University

By

Sarah E. McDonald
Master of Arts
Johns Hopkins University, 1992
Bachelor of Arts
Northwestern University, 1990

Director: Michael E. Summers, Professor
Department of Physics and Astronomy

Fall Semester 2007
George Mason University
Fairfax, VA

DEDICATION

This work is dedicated to my father, William F. Conger, for providing inspiration and encouragement throughout my academic and professional career.

ACKNOWLEDGEMENTS

TABLE OF CONTENTS

LIST OF TABLES

LIST OF FIGURES

LIST OF SYMBOLS/ABBREVIATIONS/TERMS

Ap   3-hourly planetary index that measures geomagnetic activity on a
                  linear scale from 0 to 400. It is derived from the Kp index.

ARGOS   Advanced Research and Global Observing Satellite

DMSP   Defense Meteorological Satellites Program

EUV   Extreme Ultraviolet region of the electromagnetic spectrum (100.0
                  10.0 nm)

F10.7   This index is basic indicator of solar activity. It is the amount of
                  flux emitted at 2800 MHz (10.7 cm) and is usually specified in
                  units of $10^{-22}Wm^{-2}Hz^{-1}$. Typical ranges are from 50 to 300.

FoE   Critical frequency of the E region ionosphere. Frequencies below
                  this value are reflected from the E region at vertical incidence.
                  Frequencies above this value penetrate and pass through the
                  region.

FoF1   Critical frequency of the F1 region of the ionosphere

FoF2   Critical frequency of the F2 region of the ionosphere

FUV   Far Ultraviolet region of the electromagnetic spectrum (200.0 –
                  100.0 nm)

GUVI   Global Ultraviolet Imager (a prototype of SSUSI)

hmF2   Altitude of the peak electron density in the F2 region of the
                  ionosphere

HWM93   Horizontal Wind Model (released in 1993)

IFM   Ionospheric Forecast Model is a physics-based model of the
                  ionosphere

IMAGE	Imager for Magnetopause-to-Aurora Global Exploration
IMF	Interplanetary Magnetic Field
IRI	International Reference Ionosphere is an empirical model of the ionosphere.
ISR	Incoherent Scatter Radar
Kp	3-hourly planetary index that measures geomagnetic activity on a quasi-logarithmic scale from 0 (quiet) to 9 (severe storm). It is designed to measure solar particle radiation by magnetic effects.
LORAAS	Low Resolution Airglow and Aurora Spectrograph (a prototype of SSULI)
MSIS	Mass Spectrometer Incoherent Scatter empirical model of the thermosphere
NmF2	Peak electron density in the F2 region of the ionosphere
NRLMSISE00	US Naval Research Laboratory's updated version of MSIS (released in 2000) that has been extended from the ground to the exosphere
S4	Metric for indicating the amount of variation in amplitude of a signal. It is used as an index for measuring scintillation.
SAMI2	Sami2 is Another Model of the Ionosphere is a physics-based model of the low and mid latitude ionosphere.
SCINDA	Scintillation Network Decision Aid developed by the Air Force Research Laboratory
SLIM	Semi-Empirical Low-Latitude Ionosphere model
Sq	Solar quiet current system is a regular daily variation in the geomagnetic field due to ionospheric/magnetospheric effects.
SSULI	Special Sensor Ultraviolet Limb Imager
SSUSI	Special Sensor Ultraviolet Spectrographic Imager
TEC	Total Electron Content

TIMED	Thermosphere Ionosphere Mesosphere Energy and Dynamics satellite
TOPEX/Poseidon	TOPography EXperiment for ocean circulation to track changes in sea-level height with radar altimeters (launched in 1992)
USU-GAIM	Utah State University Global Assimilation of Ionospheric Measurements
UV	Ultraviolet region of the electromagnetic spectrum (400.0 – 10.0 nm)

ABSTRACT

DAY TO DAY AND LONGITUDINAL VARIABILITY OF THE NIGHTTIME LOW
LATITUDE TERRESTRIAL IONOSPHERE

Sarah E. McDonald, Ph.D.

George Mason University, 2007

Dissertation Director: Dr. Michael E. Summers

The Earth's ionosphere is the region of upper atmosphere that is a partially ionized gas. It

extends from the mesosphere and through the thermosphere to altitudes ~1000 km where

it ultimately merges with the magnetosphere. The strong coupling of the ionosphere to

the dense regions below and the solar-driven magnetosphere above make it the most

variable component of the atmosphere. Sources of ionospheric variability or "weather"

originate from solar and geomagnetic activity and meteorological influences.

One motivation for studying the ionosphere is to improve techniques to predict

ionospheric weather that affects space-borne and ground-based technological systems

used for communication, navigation, surveillance and basic research. Geomagnetic

storms can be particularly disruptive leading to significant satellite systems failures. Even

quiet-time disturbances, such as scintillation and spread-*F* events, can impact high

frequency radio communications, especially in the equatorial and high-latitude regions. To improve prediction capabilities, a better understanding of the drivers of the variability is needed.

In this study we used recent ionospheric measurements, particularly remote ultraviolet (UV) sensing of the airglow, along with recently developed analysis techniques to better characterize the day to day and longitudinal variability of the nighttime low-latitude ionosphere and to advance the understanding of the origins of such variations. We performed a case study of the longitudinal variability in the occurrence of equatorial scintillation on 22-23 March 2002 and found evidence of longitudinal differences in the daytime and evening vertical plasma drifts that may affect the conditions for the occurrence of scintillation. This work prompted an investigation the day to day variability of the nighttime ionosphere using UV remote sensing data from the Low Resolution Airglow and Aurora Spectrograph (LORAAS). UV limb scans from March 2001 and March 2002 were used to determine the density and morphology of the post-midnight (~0230 LT) Equatorial Anomaly (EA), a prominent feature of the nighttime ionosphere. The most variable feature was the latitude and separation of the EA crests (46-67% variation about the mean). The least variable was the height of the peak densities in the EA crests (< 10% variation about the mean). The monthly mean values of the EA features are in agreement with the International Reference Ionosphere (IRI-90), a climatology model.

We used the LORAAS data along with a physics-based model of the ionosphere (SAMI2) to investigate a wavelike pattern in the longitudinal variation of ionospheric densities in the EA region. We discovered a pronounced hemispheric asymmetry in the longitudinal variations of the EA crests and showed that this is due to both longitudinally varying thermospheric winds and effects associated with the offset of the geographic and geomagnetic equators.

1 Introduction

1.1 Background

The Earth's ionosphere is a partially ionized gas that extends from the mesosphere and through the thermosphere up to altitudes of roughly 1000 km where it ultimately merges with the magnetosphere (Figure 1-1). The ionosphere is the most variable component of the atmosphere. Dynamical processes are driven by solar extreme ultraviolet (EUV) and ultraviolet (UV) heating, waves and tides propagating upward from the mesosphere, ion drag interactions, and energy and momentum sources associated with auroral region processes. Ionospheric densities and distributions vary with local time, latitude, season and solar cycle by as much as a factor of ten [e.g. *Kelley*, 1989; *Rees*, 1989]. Figure 1-2 shows typical ionospheric density profiles at day and night during solar maximum. The ionosphere is also strongly affected by geomagnetic storms. Spatial variations, due to thermospheric neutral winds and atmospheric instabilities, occur on global, regional, and local scales.

1.2 Composition of the Ionosphere

The ionosphere is a region where free electrons and ions are under the control of Earth's gravitational and magnetic fields. The ions are produced either directly by

photoionization and impact ionization of neutral atoms and molecules, or indirectly by

subsequent ionic-chemical reactions. The processes that govern the formation of the

ionosphere change with altitude since the composition and density of the neutral

atmosphere are dependent on height. Thus, the ionosphere can be roughly divided into

four overlapping regions (*D*, *E*, *F*1, and *F*2) that are roughly identified by peaks in

electron density, as illustrated in Figure 1-2. Each region is associated with different

physical processes, which are summarized in Table 1-1.
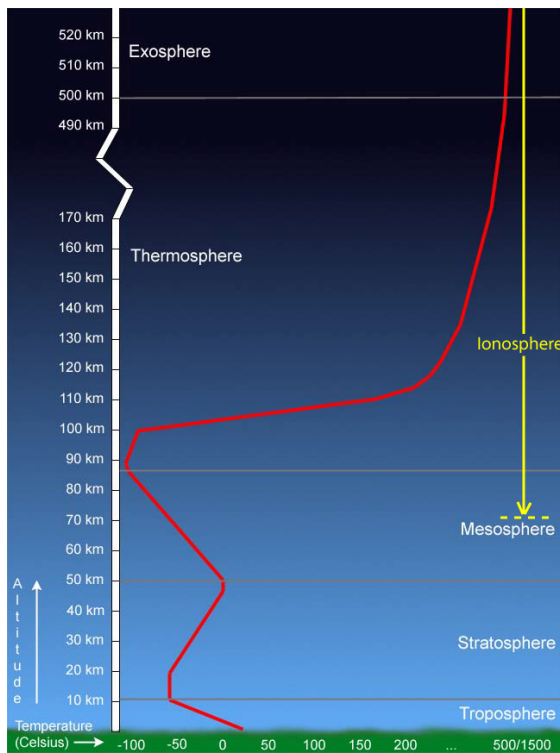
Figure 1-1 Atmospheric layers and temperature profile. (Courtesy of Windows to the Universe, http://www.windows.ucar.edu)
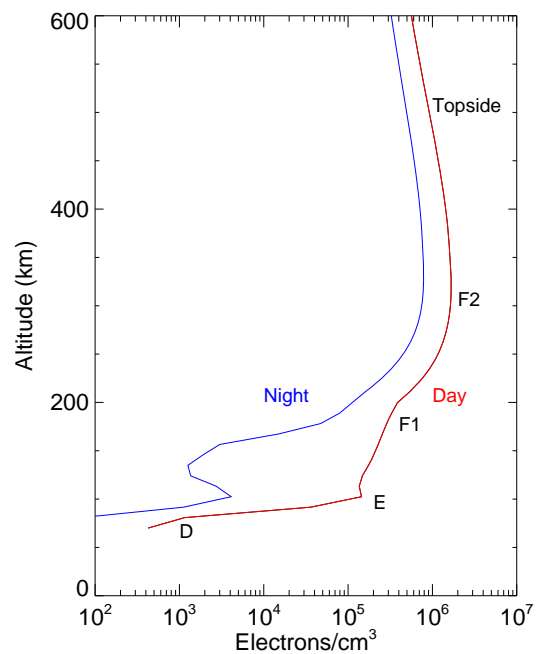
Figure 1-2 Typical daytime and nighttime ionospheric electron density profiles at solar maximum. Ionospheric regions are labeled.

The *D*-region exists from 70 to 90 km and is primarily composed of O_2 ions and

electrons. This region almost completely disappears at night when the electrons

recombine with the molecular oxygen ions. The E region (95-140 km), like the D region, is primarily composed of molecular ions. Here, ionization is present at night, but much diminished. The F region extends from 140 km to the magnetosphere and contains the highest concentration of free electrons that results from ionization of neutral atoms. During the day there is a small $F1$ layer (140-200 km), and above it a more highly ionized, dominant $F2$ layer (200-400 km). At night, the $F1$ layer disappears but the $F2$ layer persists. The topside ionosphere is the name given to the ionosphere above the F region peak.

Table 1-1 Ionospheric Constituents

Region	Altitude	Major Constituents	Primary Production Cause
D	70-90 km	NO^+, O_2^+	Lyman Alpha (121.6 nm), X-rays (< 0.8 nm), Cosmic Rays
E	90-140 km	O_2^+, NO^+	EUV radiation (80.0-102.6 nm), Soft X-rays (1.0-10.0 nm)
F1	140-200 km	NO^+, O_2^+	UV Lines and Continuum (100-800 Å), He II
F2	200-400 km	O^+	UV Lines and Continuum (100-800 Å), He II
Topside F	> 400 km	O^+, H^+	Transport from Below
Plasmasphere	> 1200 km	H^+	Transport from Below

1.3 Ionospheric Density Profiles

The ionosphere is maintained by ion-pair production, chemical loss mechanisms and transport processes according to the equation of continuity. This can be expressed as

$$\frac{\partial n_{i,e}}{\partial t} - \nabla \cdot (n_{i,e}v) = q(n,\Phi) - L(n_{i,e})$$ (1-1)

where $n_{i,e}$ is the plasma (electron or total ion) density, q is the ion production rate which depends on the neutral constituent density n and the ionizing radiation flux Φ, $L(n_{i,e})$ is the chemical loss rate and $\nabla \cdot (n_{i,e}v)$ is the divergence of a flux $F = n_{i,e}v$ due to mass transport with velocity v.

E region ions are produced mainly from O_2 molecules by photoionization. Rapid charge-exchange and atom-ion interchange also produces O_2^+ and NO^+ ions. Recombination occurs through dissociative recombination [*Chamberlain and Hunten*, 1987]. In the F1 region, photoionization produces mainly O^+ with some contribution from NO^+ and N_2^+. The dominant recombination mechanism in the F1 region also differs from that in the E region. Since radiative recombination of O^+

$$O^+ + e \rightarrow O + hv$$ (1-2)
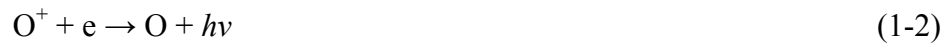
is extremely slow compared to dissociative recombination, the F1 region primarily recombines by a two step atom-ion interchange process followed by dissociative recombination [*Chamberlain and Hunten*, 1987]:

$$O^+ + O_2 \ \rightarrow \ O_2^+ + O$$ (1-3a)

4

$$O^+ + N_2 \rightarrow NO^+ + N \qquad\qquad (1\text{-}3b)$$

$$O_2^+ + e \rightarrow O + O \qquad\qquad (1\text{-}4a)$$

$$NO^+ + e \rightarrow N + O \qquad\qquad (1\text{-}4b)$$
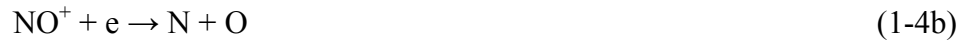
Though the E and $F1$ regions differ in their chemistry, the general shape of the ion density profiles can be explained by considering simply the production and loss of ions due to direct photoionization and recombination. Ionizing solar photons produce more ions as they penetrate deeper into the atmosphere. As photoionization occurs, the flux of photons is attenuated until a depth is reached where photoionization production drops. A layer of ionization peaking near the altitude of maximum production is created.

Sydney Chapman first treated the problem of the formation of the ionosphere [*Chapman*, 1931]. The idealized problem treated by Chapman assumes absorption of a beam of parallel, monochromatic radiation impinging on a plane-parallel atmosphere of uniform composition in which the density varies exponentially with height. The photoionization production rate can then be expressed as

$$q_i = \sigma_i n_j(z) \Phi_\infty e^{-\tau} \qquad\qquad (1\text{-}5a)$$

where σ_i is the ionization cross section, n_j is the number density of the ionizable component at altitude z, Φ_∞ is the solar flux outside the atmosphere and the optical depth τ is given by

$$\tau = \sigma_a \sec \chi \int_z^\infty n\, dz \qquad (1\text{-}5b)$$

where σ_a is the absorption cross section and χ is the solar zenith angle.

Equation (1-5) is the classical Chapman formula. Using the Chapman formula for ionization, it is possible to determine a simple approximation for the altitude profile of electron density (see for example *Chamberlain and Hunten* [1987]). The profile can be approximated by setting the production rate equal to the loss rate in equation (1-1) and assuming that the main loss process is ion-electron recombination with an effective recombination coefficient of α_{eff}, so that

$$L = \alpha_{eff} n_i n_e \approx \alpha_{eff} n_e^2 \qquad (1\text{-}6)$$

where the number of ions is approximately equal to the number of electrons. The electron density at any height in equilibrium can then be expressed as

$$n_e = n_{em} \exp\left\{\frac{1}{2}\left[1 - \frac{z}{H} - \sec \chi \exp\left(-\frac{z}{H}\right)\right]\right\}$$
(1-7)

where $n_{em} = (q_m/\alpha_{eff})^{1/2}$ and q_m is the maximum ion production rate.

The collision frequencies of ions and electrons with neutrals play a key role in the dynamics of the ionosphere. When the collision frequency of a charged particle is significantly larger than its gyrofrequency about the magnetic field, the dominant motion of the particle is parallel to the applied forces as if no magnetic field were present (Figure 1-3a). When the collision frequency is much smaller than the gyrofrequency, the particle motion is along the magnetic field in the plane parallel to the magnetic field and perpendicular to the applied forces in the plane perpendicular to the magnetic field (Figure 1-3b). For example, in the presence of an electric field, $\mathbf{E}$, and magnetic field, $\mathbf{B}$, the ions and electrons move at a velocity equal to $\mathbf{E} \times \mathbf{B}/B^2$ perpendicular to $\mathbf{B}$.
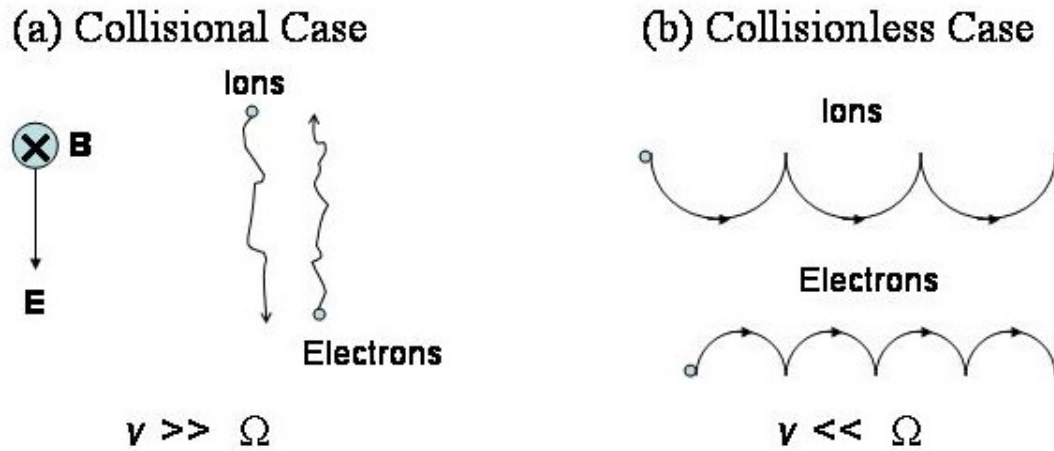
Figure 1-3 Ion and electron trajectories for a (a) collisional plasma and (b) collisionless plasma [after *Kelley*, 1989].

Above about 75 km, the electron-neutral collisions become infrequent. However the ion collision frequency remains greater than its gyrofrequency up to ~130 km [*Kelley*, 1989]. The electrons move along the field lines, while the ions are influenced by the motions of the neutral atmosphere. Differences in the motions of the ions with respect to the electrons lead to the generation of currents and electric fields, as will be discussed in more detail in Section 1.5.

At higher altitudes (between 130 km and 300 km) the dynamical transport time for diffusive flow becomes shorter than the lifetime of the ions. Thus, in the *F*2 region, diffusion becomes an important factor in plasma transport and energy exchange. In this region, electrons and ions diffuse through the ambient neutral atmosphere. That is, both the electrons and ions move at nearly the same velocity along the field lines and move

perpendicular to applied forces. As discussed below in Section 1.4, thermospheric neutral winds generate a vertical plasma drift. At the equator, where the magnetic field is nearly parallel to Earth's surface, the plasma is strongly affected by the E region electric fields and drifts upward with an $\mathbf{E} \times \mathbf{B}$ drift velocity.

The field-aligned motion is influenced by gravity, and density and temperature gradients. In midlatitude regions, electrons travel upward along the nearly vertical magnetic field lines, whereas the ions are bound by gravity. The slight separation between the ions and electrons generates a significant electric field, known as the ambipolar electric field, which prevents the electrons from moving away from the ions.

In the $F2$ region, the continuity equation must include the divergence of mass transport term

$$\nabla \cdot (n v_D) \approx \frac{\partial}{\partial z} (n v_D) \qquad (1\text{-}8)$$

where the ambipolar diffusion velocity in an isothermal atmosphere is given by

$$v_D = -D_a \left[\frac{1}{n} \frac{\partial n}{\partial z} + \frac{1}{H_1} \right] \qquad (1\text{-}9)$$

where H_1 is the scale height of the ambient atmosphere and D_a is the ambipolar diffusion coefficient. In the $F2$ region charge exchange reactions dominate over dissociative recombination in limiting the rate of recombination. Instead of the loss rate being proportional to n_e^2, as in the E and $F1$ regions, it is proportional to n_e. The continuity equation, therefore, is written as

$$\frac{\partial n}{\partial t} = -\beta(z)n_e + \frac{\partial}{\partial z}\left[D(z)\left(\frac{\partial n_e}{\partial z} + \frac{n_e}{2H_1}\right)\right]. \tag{1-10}$$

$\beta(z)$ is the recombination rate coefficient in the F2 region and is given by

$$\beta(z) = \beta_0 \exp[-(z-z_0)/H(X)] \tag{1-11}$$

where $H(X)$ is the weighted scale height of O_2 and N_2.

In the steady state solution, a Chapman-like profile, as shown in Figure 1-4 is recovered.
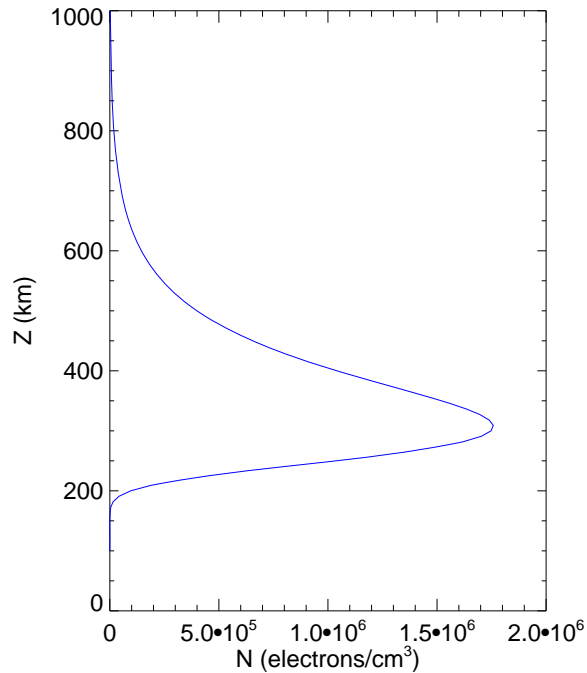
Figure 1-4 A typical Chapman profile of the nighttime *F* region ionosphere. The density peaks at ~300km.

Until this point, we have restricted our discussion to a single ionizable component in a plane parallel, isothermal plasma. It is worth briefly discussing some of the equations that must be considered in a more realistic description of the ionosphere. For example, when multiple ion species are present, there must be consideration for differing flow velocities of the species, ion-ion friction effects and electric field coupling [e.g. *Banks and Kockarts*, 1973]. Much of Earth's ionospheric processes can be characterized by the 5-moment approximation to the transport equations with the additional assumption that there are small relative drifts between interacting species (cf. Equations (1-26a – 1-26d)). A comprehensive discussion of the transport equations can be found in *Schunk and Nagy* [2000].

11

Generally, Equations (1-26) must be solved numerically, but we can obtain

expressions for the electron and ion densities by making some additional assumptions.

The diffusion approximation can be used in regions of the ionosphere where plasma flow

is subsonic and the time constant for plasma processes is long. In this case, the left hand

side of Equation (1-26b) goes to zero. Following the discussion in *Banks and Kockarts*

[1973], we can additionally restrict ourselves to plasma flow along the magnetic field in a

topside *F* region ionosphere, which is dominated by diffusion. In diffusive equilibrium,

the ion momentum equation for flow along a magnetic field line is given by

$$\frac{1}{n_j^+}\frac{\partial p_j}{\partial s} + m_j g_\parallel - Z_j e E_\parallel = 0 \qquad (1\text{-}12a)$$

where n_j^+ is the density of the *j*th ion species, p_j is its momentum, m_j is its mass and Z_j is

the charge number. Similarly, the electron momentum is given by

$$\frac{1}{n_e}\frac{\partial p_e}{\partial s} + e E_\parallel = 0. \qquad (1\text{-}12b)$$

Also, charge neutrality is assumed where

$$n_e = \sum_j Z_j n_j^+. \qquad (1\text{-}13)$$

At mid- and high latitudes, where the topside F region magnetic field is nearly vertical, the parallel electric field ($E_{\parallel}$) arranges the ions in layers with lighter ions settling at higher altitudes than heavier ions. The electric field due to charge separation can be expressed as

$$eE_{\parallel} = \frac{g_{\parallel}\sum(Z_j n_j^+ m_j / n_e) + kT_i[\partial/\partial s(\ln T_i / T_e)]}{(T_i / T_e) + \sum(Z_j^2 n_j^+ / n_e)} \qquad (1\text{-}14)$$

Equation (1-14) can be substituted into the Equations (1-12) and integrated along a portion of the magnetic field from a to s to obtain the coupled equations for the electron and ion densities

$$n_e = n_{ea}\frac{(T_e + T_i)_a}{(T_e + T_i)}\exp\left[-\int_a^s \frac{g_{\parallel}m^+(s')ds'}{k(T_e + T_i)}\right] \qquad (1\text{-}15a)$$

$$n_j^+ = n_{ja}^+\frac{(T_e + T_i)_a}{(T_e + T_i)}\exp\left[-\int_a^s \frac{g_{\parallel}m_j ds'}{kT_i} + \int_a^s \frac{T_e}{T_i}\frac{m^+(s')g_{\parallel}ds'}{k(T_e + T_i)}\right] \qquad (1\text{-}15b)$$

where we have assumed the ions are singly ionized ($Z_j = 1$) so that m^+ denotes the mean ionic mass ($\Sigma n_j^+ m_j / n_e$).

13

Finally, we note that a distinguishing feature of the *D* region is the predominance of negative ions [*Chamberlain and Hunten*, 1987] and heavy hydrated water cluster ions of the type $H_3O^+ \cdot (H_2O)_n$ [*Bauer*, 1973]. The relatively high concentrations of neutral species at these altitudes lead to complicated positive and negative ion chemistry, which will not be discussed further because it is beyond the scope of this work. See *Ferguson* [1971], for example, for additional information on *D* region chemistry.

1.4 Thermospheric Winds

An important aspect of the distribution of plasma in the ionosphere that was ignored in the above discussion is the role of thermospheric winds. Together, the thermosphere and ionosphere form a dynamical system that responds to a variety of forces. Thermospheric, or neutral air motions are key to the understanding of the thermosphere/ionosphere system. Important aspects of ionospheric structure that depend directly on neutral winds and compositional transport include maintenance of the nighttime ionosphere [e.g. *Anderson and Roble*, 1981], equatorial spread-*F* (ESF) [e.g. *Zalesak et al.*, 1982; *Tsunoda*, 1985; *Devasia et al.*, 2002] and geomagnetic storm effects [e.g. *Richmond and Matsushita*, 1975]. These ionospheric phenomena, excluding storm effects, will be described in more detail in the sections below.

Winds in the thermosphere are driven primarily by pressure gradients resulting from temperature differences. Wind motion is also modulated by the Coriolis Effect, momentum transfer due to ion-neutral collisions, and viscous forces. (See *Titheridge*

[1995] for a review of thermospheric winds.) The absorption of solar EUV radiation is the dominant source of heating. Unequal heating between day and night and winter and summer hemispheres sets up pressure gradients that force the atmosphere to respond by moving horizontally from warm to cold [*Rees*, 1989]. Secondary sources of heating arise from collisions between the atmospheric constituents and precipitating energetic auroral particles, and friction resulting from the interaction of the neutral gas with magnetospherically driven ion flows at high latitudes. Deposition of energy from the lower atmosphere in the form of upward propagating planetary waves, tides and gravity waves [*Forbes et al.*, 1993] is also important, especially in the lower thermosphere. Ion-neutral collisions also transfer momentum between the ions and neutrals. At high latitudes, large-scale plasma convection accelerates the neutral wind. At midlatitudes and below, the "ion-drag" force act to retard the winds in the *F* region. Winds at different heights are coupled through frictional drag, μ/ρ, where μ is the coefficient of viscosity and ρ is the mean gas density. Since the density decreases exponentially with height and the viscosity is nearly constant [*Titheridge*, 1995], the frictional drag increases so that at altitudes above 250 km the horizontal wind velocity is independent of height.

To zeroth order, there is an eastward flow from dayside to nightside that is mainly controlled by heating of the atmosphere due to absorption of EUV solar radiation. Daytime meridional, or north/south, winds are poleward; nighttime winds are equatorward. Zonal, or east/west winds are westward before local noon and eastward in the afternoon. Both the zonal and meridional winds are at a minimum during the

equinoxes. This diurnal component of the wind is apparent in Figure 1-5, which shows

winds during March equinox at 126° longitude and 300 km altitude from the Horizontal

Wind Model (HWM-93) [*Hedin et al.*, 1996]. At this altitude (and latitudes) the major

forces, in addition to solar heating, are due to ion drag and the Coriolis force. The

meridional wind (Figure 1-5a) is generally symmetric about the equator and the

amplitude increases from low to high latitudes. The equatorial zonal winds (Figure 1-5b)

reach a maximum at night when the ion drag has a minimal effect [*Titheridge*, 1995]. In

the next section, we shall see that both *E* and *F* region winds are responsible for driving

currents and producing electric fields that strongly affect the nighttime *F* region
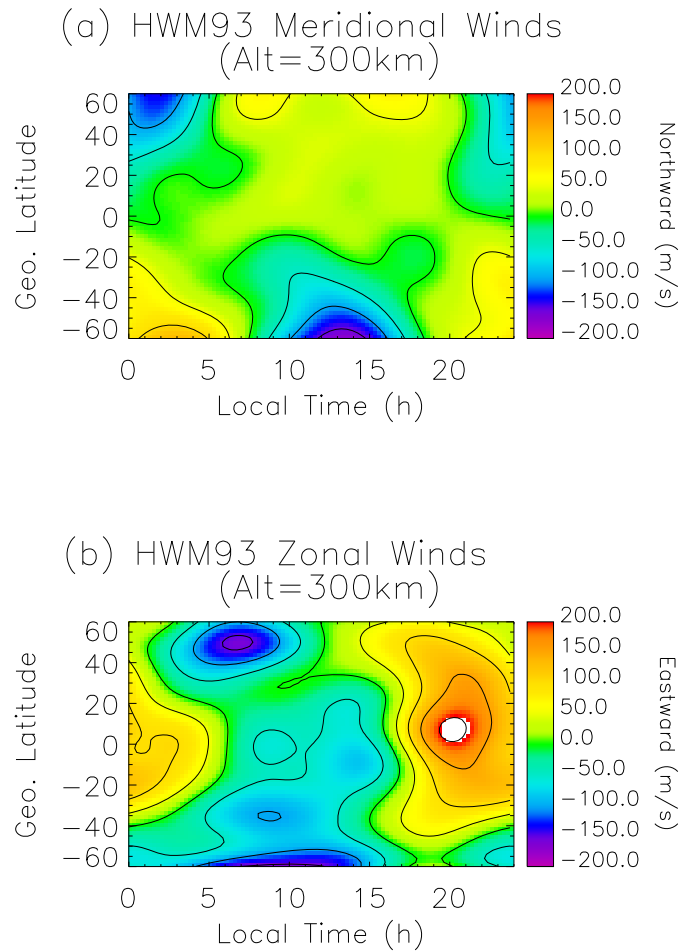
ionosphere.

Figure 1-5 HWM93 (a) meridional and (b) zonal winds at 126˚ longitude at March equinox.

1.5 Low-Latitude Dynamics

The low-latitude *F* region ionosphere (150 – 1000 km) is strongly influenced by the dynamics of the *E* region (100 – 150 km) [e.g. *Kelley*, 1989]. At *E* region altitudes, the ion-neutral collision frequency is so high that ions are dragged across the magnetic field lines along with the neutrals whereas the electrons are constrained to move along the

field lines. Differences in ion and electron velocities, and small differences in their concentrations, are responsible for generating currents and polarization electric fields in this highly conducting region of the ionosphere. The electric fields are generated due to the finite divergence of the currents. The divergence creates a charge density via the current divergence equation,

$$\nabla \cdot J = -\partial \rho_c / \partial t \qquad (1\text{-}16)$$

which in turn creates electric fields through Poisson's equation:

$$\nabla \cdot E = \rho_c / \varepsilon_0 \qquad (1\text{-}17)$$

The electric field modifies the fluid velocities and forces the divergence to zero ($\nabla \cdot J = 0$). Charge densities in the ionosphere, and hence electric fields, build up within ~10^{-6} seconds [*Kelley*, 1989]. Such electric fields that result from winds in the thermosphere are called dynamo electric fields. Figure 1-6 shows east/west electric fields that are generated by thermospheric winds in the *E* region. Due to the high conductivity along the magnetic field, the dynamo fields map along the magnetic field lines to the *F* region.

The global current system that results from thermospheric winds is known as the solar-quiet (Sq) current system. The Sq current is significantly enhanced at the magnetic

18

equator where the magnetic field lines are nearly horizontal. This band of enhanced

current is known as the equatorial electrojet.
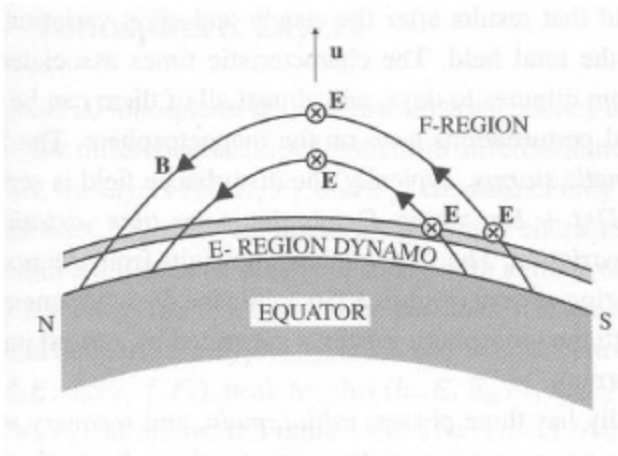
Figure 1-6 Thermospheric winds in the equatorial E region generate dynamo electric fields as the ions are dragged across B. These dynamo fields are responsible for the equatorial electrojet (from *Schunk and Nagy* [2000]).

To understand how the electrojet comes about, the current system can be

described with a few simplified equations. The current is given by the generalized Ohm's

law (e.g. *Gombosi* [1998], *Kelley* [1989]):

$$J = \sigma \cdot (E + u \times B) \tag{1-18}$$

where $\boldsymbol{u}$ is the fluid velocity and the conductivity tensor (σ) is given in the form

$$\sigma = \begin{pmatrix} \sigma_P & 0 & \sigma_H \\ 0 & \sigma_0 & 0 \\ -\sigma_H & 0 & \sigma_P \end{pmatrix} \tag{1-19}$$

where σ_0, σ_P and σ_H are the specific conductivity, Pedersen conductivity and Hall

conductivity, respectively. The coordinate system is defined such that the z axis is

upward, the y axis is horizontal and northward, and the x axis is eastward.
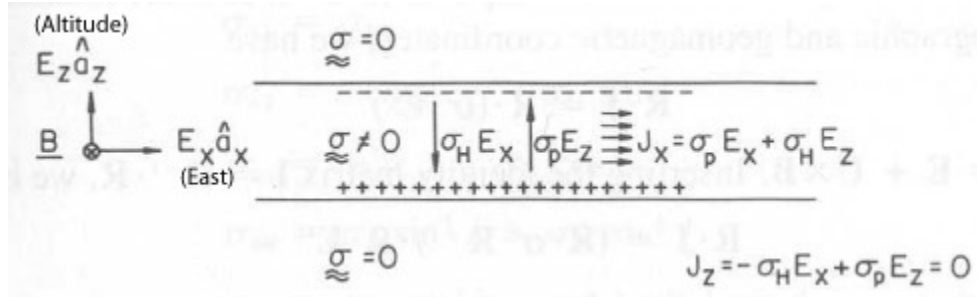
Figure 1-7 The equatorial electrojet in a slab geometry. Altitude increases in the positive z direction and East is in the positive x direction (from *Kelley* [1989]).

An eastward, or zonal, electric field in combination with a northward

geomagnetic field drives a small Pedersen current along the dayside equator. A vertically

downward Hall current also flows. Figure 1-7 illustrates this with a simple slab

approximation of the equatorial electrojet region. The E region conductivity can be

considered bounded in the vertical direction since the Hall conductivity is highly altitude

dependent. The Hall current cannot flow across the boundary and charge layers build up.

The charge layers in turn generate an upward electric field. In steady-state, no vertical

current can flow and the vertical Pedersen current must cancel the Hall current. Thus,

$\sigma_H E_x = \sigma_P E_z$ and $E_z = (\sigma_H / \sigma_P)E_x$. The zonal current is then given by

$$J_x = \sigma_H E_z + \sigma_P E_x \tag{1-20}$$

and

$$J_x = [(\sigma_H{}^2)/(\sigma_P{}^2) + 1]\ \sigma_P E_x = \sigma_c E_x \tag{1-21}$$

20

where σ_c is known as the Cowling conductivity. Note that the zonal neutral wind has been neglected here. The zonal conductivity is enhanced by the Cowling conductivity factor, which leads to the intense current jet at the magnetic equator [*Kelley*, 1989]. At latitudes just off the magnetic equator, the slight tilt of the geomagnetic field lines is sufficient to allow the polarization charges to partially drain, thus reducing the Cowling conductivity [*Rishbeth and Garriott*, 1969].

The dynamo electric fields play a very important role in the dynamics of the low-latitude ionosphere. The electric fields are transmitted along the magnetic field lines to *F* region altitudes because of the high parallel conductivity (Figure 1-6) [*Schunk and Nagy*, 2000]. During the daytime, the electric fields are eastward, which causes an upward plasma drift, while the reverse occurs at night. The *F* region ionosphere is nearly collisionless, thus the ions and electrons drift together across the magnetic field at a steady $\mathbf{E} \times \mathbf{B}/B^2$ velocity. Figure 1-8 shows typical characteristics of vertical drifts with upward drift velocities of about 20 m/s during the day and downward velocities of about 40 m/s at night [*Fejer and Scherleiss*, 2001]. The measurements of the drift velocities were taken with the Jicamarca incoherent scatter radar in Peru, which is situated 1° from the magnetic dip equator. Also evident in Figure 1-8 is an increase in the upward velocity of the drifts before they turn downward. This is due to a postsunset enhancement of the zonal electric field and can be explained by taking into account *F* region winds, which produce *F* region dynamo electric fields, and the sharp east-west gradients at the sunset terminator [*Heelis et al*., 1974].
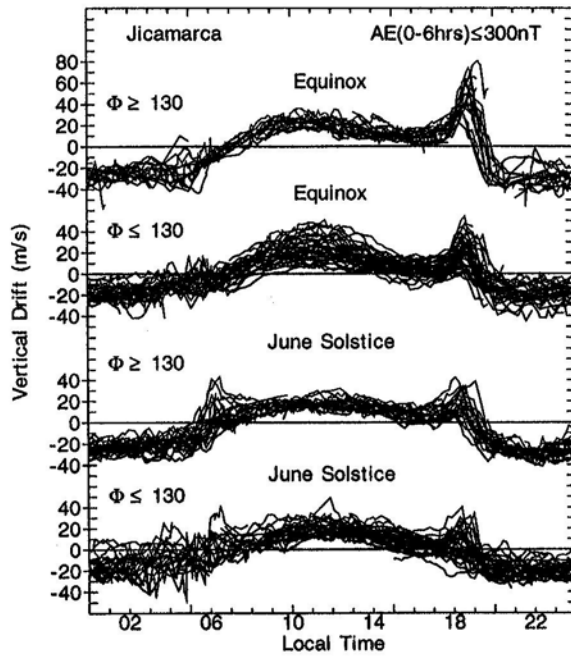
Figure 1-8 Quiet-time Jicamarca F-region vertical plasma drifts during equinox and June solstice for two ranges of the decimetric solar flux index (Φ) (from *Fejer and Scherleiss* [2001]).

The upward drift of plasma acts in combination with ambipolar diffusion along the geomagnetic field lines and results in a transport of ionization away from the magnetic equator toward higher latitudes [*Hanson and Moffett*, 1966; *Anderson*, 1973a and 1973b]. This effect, often called the fountain effect, is illustrated in Figure 1-9. The plasma rises until pressure forces and gravity cause the plasma to descend along the field lines to tropical latitudes. The regions of enhanced plasma density in the *F*2 region of the tropical ionosphere, first recognized by Appleton [*Appleton*, 1946], are known collectively as the equatorial anomaly or Appleton anomaly. The postsunset enhancement of the $\mathbf{E} \times \mathbf{B}$ drift has a significant effect since it causes the *F* layer plasma at the equator to be driven to very high altitudes, typically ~500 km, where recombination is slow and collisions are rare. Thus, the equatorial anomaly often persists into the pre-dawn hours.

22
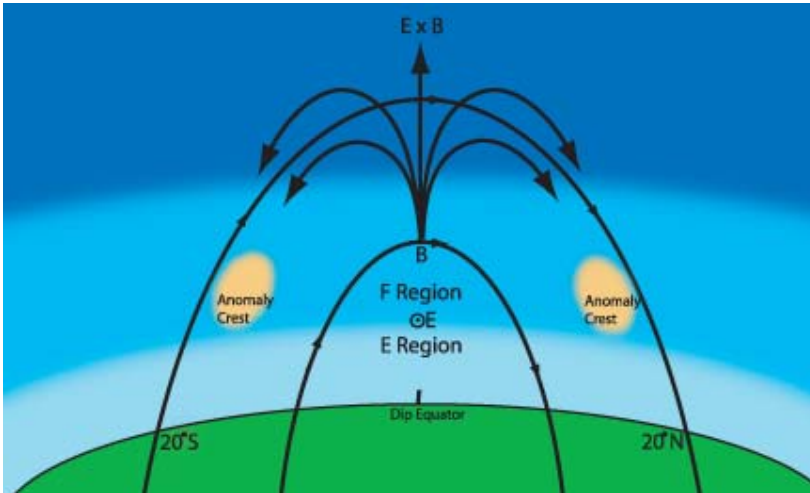
Figure 1-9 Diagram of the fountain effect and resultant equatorial anomaly crests.
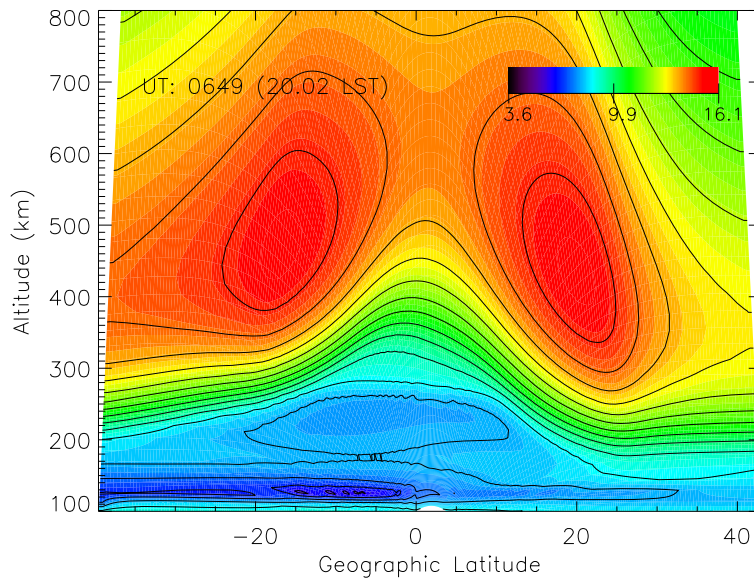
Figure 1-10 Numerical model calculations (SAMI2) of electron density ($\log_{10}(N_e)$ is shown) in the equatorial anomaly region at 2000 LT for equinox conditions at 198° geographic longitude. Here, the southern anomaly crest is slightly higher in altitude than the northern anomaly crest.

The two major factors that influence the morphology of the anomaly crests are the upward $\mathbf{E} \times \mathbf{B}$ drift and the meridional winds. A strong upward $\mathbf{E} \times \mathbf{B}$ drift causes the plasma to drift to higher altitudes and diffuse down at higher latitudes, affecting the separation of the anomaly crests. North/south asymmetries in the anomaly crests are due to thermospheric neutral winds. Figure 1-10 shows electron densities calculated with a numerical model, SAMI2, for equinox conditions at 2000 LT (Please see Section 1.9 for more details on SAMI2). In the early evening hours, the component of the wind along the magnetic field is gently northward. The winds push the southern anomaly to a slightly higher altitude than the northern anomaly. After midnight, the southern hemisphere winds are strongly northward and the northern hemisphere winds are only slightly southward. The change in wind pattern creates an asymmetry in the anomaly densities by 0230 LT, as shown in Figure 1-11. The southern winds maintain the southern anomaly crest at an altitude where recombination is slow, while the lack of northern winds allows the northern anomaly crest to descend to an altitude where it decays more rapidly.
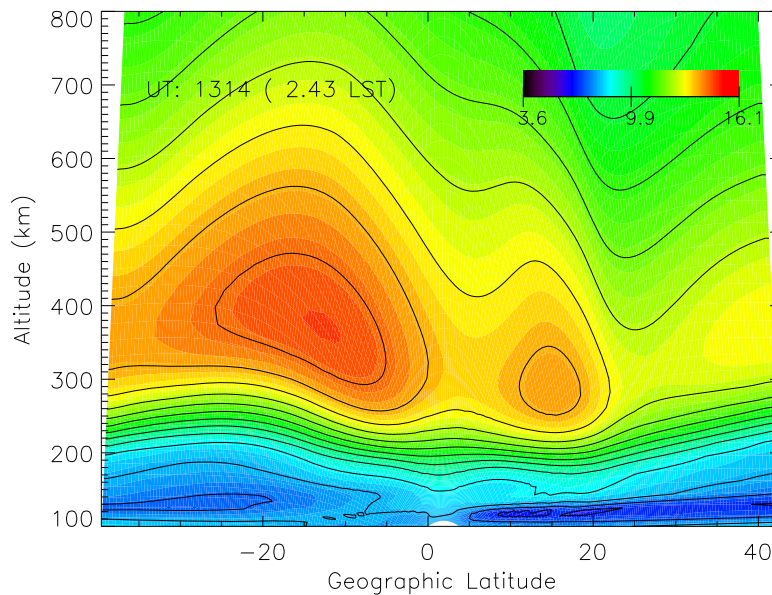
Figure 1-11 Numerical model calculations (SAMI2) of electron density ($\log_{10}(N_e)$ is shown) in the equatorial anomaly region near 0230 LT for equinox conditions at 198° geographic longitude. Stronger equatorward winds in the southern hemisphere maintain the southern anomaly crest, while the northern crest decays at a faster rate.

The morphology of the anomaly crests varies with solar cycle, time of day, season and longitude. At solar minimum, the anomaly is most pronounced at about 1400 LT and declines until it disappears around 2100 LT [*Anderson*, 1973a]. During solar maximum, more energy is deposited into the upper atmosphere, generating a denser ionosphere so that the anomaly can persist until well after 0200 LT. Seasonal and longitudinal effects can be attributed to the difference in alignment of the sunset terminator with the local magnetic meridian (illustrated in Figure 1-12). The season when the solar terminator aligns with the magnetic meridian produces a maximum in the magnetic eastward wind as well as a maximum in the longitudinal gradient in the integrated conductivity [*Abdu et al*. 1981; *Batista et al*., 1986]. This results in a maximum $\mathbf{E} \times \mathbf{B}$ drift. This is also when the meridional wind is at a minimum. Thus, for a longitude that has a small magnetic

25

declination angle, the anomaly crests will be the strongest and most symmetric during the equinoxes. Day to day variations in the anomaly crests are also observed and are caused by daily variations in the electrojet and neutral winds.
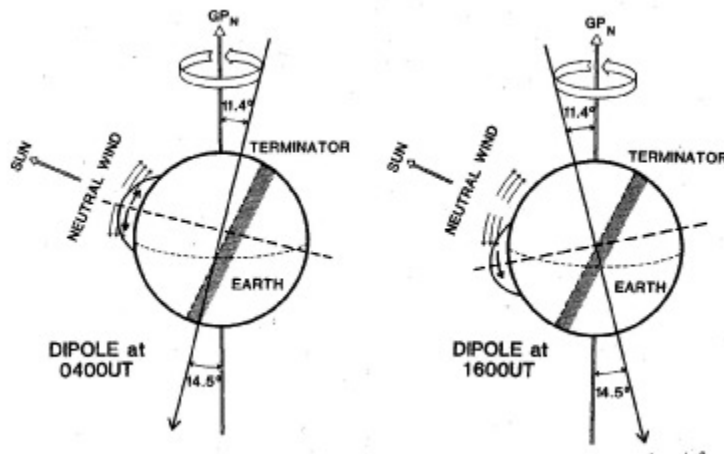
Figure 1-12 Magnetic dipole geometry at two universal times. The offset of the magnetic axis from the geographic axis is 11.4° in the northern hemisphere and 14.5° in the southern hemisphere (from *Sojka and Schunk* [1985]).

1.6 Ionospheric Instabilities

The dynamics within the low-latitude region contribute to the formation of instabilities in the ionosphere which form irregularities in the plasma distribution. The instabilities are generally referred to as equatorial spread-*F* (ESF) events and primarily occur at night. The post sunset enhancement of the upward $\mathbf{E} \times \mathbf{B}$ drift raises the *F* region ionosphere above 300 km. In the absence of sunlight, the lower ionosphere rapidly decays and a steep density gradient develops on the bottomside of the raised *F* region. This produces one of the conditions for a gravitational Rayleigh-Taylor (R-T) instability to form. Another necessary factor is that there must be a density perturbation on the bottomside to serve as a seeding source. Figure 1-13(a) shows a simple two-dimensional

26

model of how a R-T instability is set up. If a small perturbation is present, the divergence between the current in the dense *F*2 region and the depleted region below causes perturbation electric fields to build up. These electric fields cause an upward perturbed $\delta\mathbf{E} \times \mathbf{B}$ drift in the depletions and a downward drift in the enhanced region, which leads to larger perturbations. Figure 1-13(b) shows how the instability can grow with time. Large irregularities are observed as bubbles or depletions in the ion density. If a signal from a satellite passes through such a disturbed region, the receiver picks up fluctuations in the signal strength, which is known as scintillation [*Kelley*, 1989].
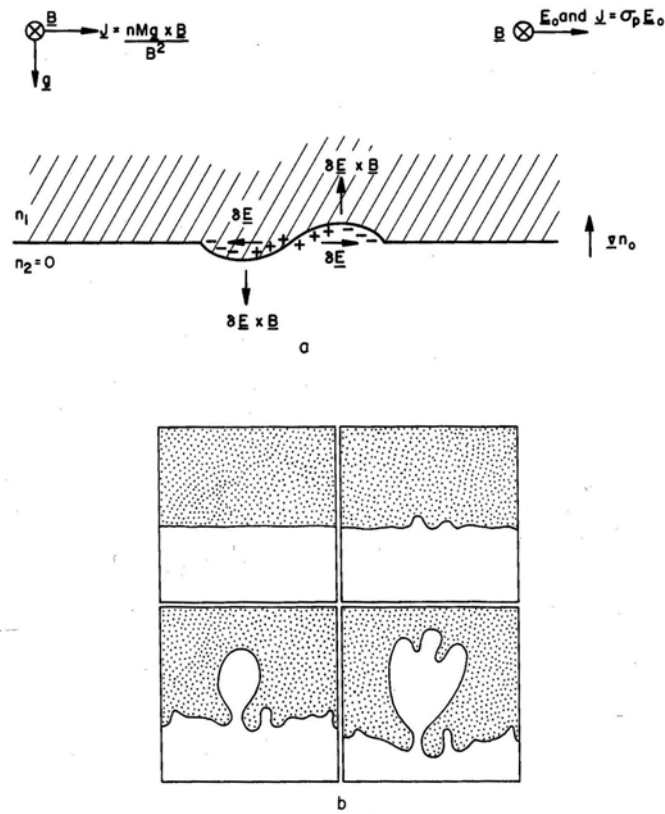
Figure 1-13 (a) Schematic diagram of the plasma analog of the Rayleigh-Taylor instability in the equatorial geometry. (b) Sequential sketches made from photos of the hydrodynamic Rayleigh-Taylor instability. A heavy fluid is initially supported by a transparent lighter fluid (from *Kelley et al.* [1981]).

Initial conditions which lead to an ESF event on a given night depend in a complicated way on the state of the ionosphere and the neutral atmosphere. The strength of the equatorial electrojet at sunset, integrated Pedersen conductivity, and bottomside density gradients all play a role in setting up the conditions for ESF. *Fejer et al.* [1999] showed that the magnitude of the evening upward vertical plasma drift was the main factor in determining the occurrence of ESF. On the other hand, there is evidence that meridional neutral winds can create an asymmetric density distribution in the anomaly

28

region that suppresses the growth of the R-T instability [*Maruyama and Matuura*, 1984; *Devasia et al.*, 2002].

1.7 Ionospheric Measurements

Scientists have been monitoring the ionosphere since its discovery in the early 20th century. Here, we briefly introduce several of the ground and space based instruments and techniques that are currently in use.

The most widely used and one of the simplest, ground-based instruments is the ionosonde. Ionosondes send a spectrum of radio waves vertically into the atmosphere, sweeping from lower to higher frequencies (typically 0.1 to 30 MHz), and record the return signals reflected from the different layers of the ionosphere. The time it takes for the signal to return to the receiver, the strength of the signal, and the highest frequency reflected from the ionosphere are used to obtain the peak density and altitude of the various ionospheric layers. A unique relationship exists between the sounding frequencies and ionization densities. The peak (or critical) plasma frequency of the *F*2 region, *foF2*, is related to the peak electron density, *NmF2*, by:

$$\frac{NmF2}{cm^3} = 1.24 \times 10^4 \left(\frac{foF2}{Mhz} \right)^2 \qquad (1\text{-}22)$$

Hundreds of ionosondes are distributed world-wide, with the highest concentration in North America and Northern Europe. Recently, new digital ionosondes, or digisondes, have come into operation. Digisondes can be used to measure the full electron density profile as well as plasma drift velocity [*Reinisch and Huang*, 1983].

Incoherent Scatter radar (ISR) is the most powerful ground based technique for studying the ionosphere. Electrons in the ionosphere scatter electromagnetic waves beamed from the ground. The returned signal provides information about the temperature, composition and velocity of ions and electrons. ISR instruments provide information about the ionosphere to heights well above the *F* peak [*Kelley*, 1989].

Ground based measurements of the ionosphere are quite accurate; however they only provide local information about ionospheric structure and dynamics. To study the global nature of the ionosphere, numerous satellite borne instruments have been launched into orbit. There are far too many to discuss here. But we briefly mention several instruments and remote sensing techniques that are used in this work.

The longest running satellite program is the U.S. Air Force Defense Meteorological Satellite Program (USAF DMSP), which has launched 44 satellites and has been collecting atmospheric data since 1965. Currently, there are several satellites in operation. The most recent Block 5D-3 satellite was launched in November 2006 and another will be launched in 2008. All of the satellites contain instruments that measure

in-situ (830 km) plasma density, composition and drift velocity. The two most recent satellites also contain instruments that measure FUV airglow emissions from the upper atmosphere. The Special Sensor Ultraviolet Spectrographic Imager (SSUSI) scans the disk and limb up to a tangent altitude of 500 km [*Paxton et al., 1992*]. The Special Sensor Ultraviolet Limb Imager (SSULI) collects EUV and UV (80 nm – 170 nm) airglow emission from tangent altitudes 50 – 750 km [*McCoy et al*., 1992; *McCoy et al*., 1994]. The airglow measurements collected by SSUSI and SSULI can be used to obtain the composition and temperature of the thermosphere and ionosphere.

Space-to-ground measurements that have been originally designed to remove ionospheric effects are also a good source of ionospheric density measurements. Signals collected from the Global Positioning System (GPS) constellation of satellites can be used to obtain line-of-sight total electron content (*TEC*), the integrated electron density along the path. Similarly, the NASA/Centre Nationale d'Etudes Spatiales TOPEX/Poseidon satellite, which was launched in August 1992 and operated until January 2006, carried a dual-frequency radar altimeter operating at 13.6 GHz and 5.6 GHz. Vertical *TEC* estimates are given by the ionospheric range correction computed from the differences in the altimeter measurements [*Imel*, 1994] of the sea surface height.

In this work, we primarily focus on the analysis and interpretation of data collected from the Low Resolution Airglow and Aurora Spectrograph (LORAAS), a SSULI prototype that flew aboard the United States Air Force Space Test Program's

31

Advanced Research and Global Observation Satellite (ARGOS) from 1999 to 2002

[*McCoy et al.*, 1992]. Additionally, we use datasets from ionosondes, TOPEX/Poseidon,

and the Global Ultraviolet Imager (GUVI) [*Christensen et al.*, 2003], which is a

prototype of SSUSI.

1.8 FUV Remote Sensing – O I 135.6 nm

We use FUV measurements from both LORAAS and GUVI instruments

throughout this work. Specifically, we use measurements of the O I 135.6 nm emission

feature. The principal source of the FUV fluorescence in Earth's upper atmosphere at

nighttime (nightglow) is due to the radiative recombination of atomic oxygen ions, the

inverse of photoionization:

$$O^+ + e \rightarrow O^* \tag{1-23}$$

Recombination directly to the ground state produces a narrow continuum shortward of

91.1 nm, whereas recombination into excited states of O produces many emission lines in

the UV (135.6, 130.4, 102.7, 98.9 nm) as well as many visible and infrared wavelengths.

(See *Meier* [1991] for a detailed discussion of the UV airglow.) Ion-ion mutual

neutralization,

$$O^+ + O^- \rightarrow 2O^* \tag{1-24}$$

32
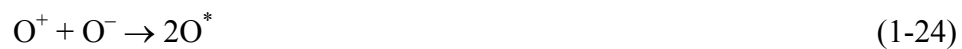
also leads to excited states of atomic oxygen that weakly contribute to the observed line radiation (with the exception of the 91.1 nm continuum.) In this work, we ignore this reaction since its contribution is less than 11% of the total column emission rate at altitudes above 275 km [*Meléndez-Alvira*, 1999].
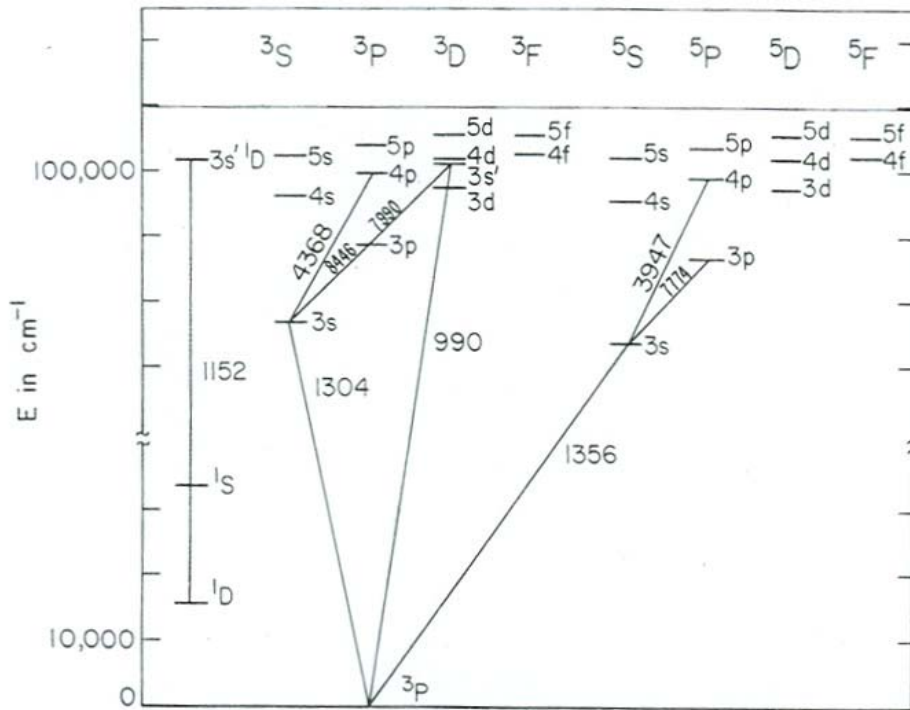
Figure 1-14 Energy level diagram for atomic oxygen showing levels below the O^+ (^4S) ionization limit. Several important emission lines are indicated on the diagram along with the wavelengths in angstroms (from *Julienne and Davis*, 1976).

The 135.6 nm emission line is produced by the relaxation of electronically excited atomic oxygen from the O(^5S) state to the ground O(^3P) state, illustrated in Figure 1-14. The emission actually consists of a doublet ($^3P_2 - {}^5S_2$) (135.56 nm) and ($^3P_1 - {}^5S_2$) (135.85 nm), where the 135.6 nm feature is a sum of the emission in both lines of the

doublet. Ignoring multiple scattering (full equations can be found in *Meier* [1991]), the intensity of the 135.6 nm line is given by

$$4\pi I = \int j(s)ds \qquad (1\text{-}25a)$$

where j(s), the volume excitation rate from radiative recombination is given by

$$j = \alpha n_e n_{O+} \qquad (1\text{-}25b)$$

where n_e is the electron number density, n_{O+} is the oxygen ion number density, and α is the recombination rate. In practice, the recombination rate coefficient we use is an effective rate coefficient that is the sum of the direct recombination coefficient in the ^5S state and a cascade contribution from higher states (Figure 1-14). The 777.4 nm line is the main contributor [*Julienne and Davis*, 1976] from the higher states.

1.9 Ionospheric Models

There are numerous models of the ionosphere, ranging from empirical models to global physics-based models that couple differing atmospheric regions to physics-based data assimilation models. Here, we describe several models that are used in this work.

The International Reference Ionosphere (IRI-90) is an empirical climatology model of the *F* region ionosphere (100 km to 1000 km) that describes monthly averages

of electron density, electron temperature, ion temperature and ion composition [*Bilitza*, 1990]. This model is based on ground, rocket and satellite measurements of the ionosphere and uses analytical expressions and functions to represent temporal and spatial variations of densities and temperatures. Global variations are described by Legendre polynomials. One of the advantages of an empirical model such as IRI is that it requires very little computational time. But because IRI is not based on first principles physics, it cannot be used to study the various drivers of the dynamics of the ionosphere.

SAMI2 (Sami2 is Another Model of the Ionosphere) is a physics-based model of the low-latitude ionosphere [*Huba et al.*, 2000]. SAMI2 treats the dynamic plasma and chemical evolution of several ion species (H^+, He^+, N^+, O^+, N_2^+, NO^+, and O_2^+) in the altitude range from 85 km to 20,000 km. The model solves continuity, momentum and energy equations for the ions and electrons taking into account all chemical and transport processes that are thought to be important. The thermal balance equations are solved for three ion species (H^+, He, O^+) and the electrons. The ion continuity equation for each ion species *i* is:

$$\frac{\partial n_i}{\partial t} + \nabla \cdot (n_i V_i) = P_i - L_i n_i \qquad (1\text{-}26a)$$

where P_i are the ion production terms and L_i are the ion loss terms. These terms involve photoionization, radiative recombination, and chemistry. The ion momentum equation is:

$$\frac{\partial V_i}{\partial t} + V_i \cdot \nabla V_i = -\frac{1}{\rho_i}\nabla P_i + \frac{e}{m_i}E + \frac{e}{m_i c}V_i \times B + g - v_{in}(V_i - V_n) - \sum_j v_{ij}(V_i - V_j)$$

<div align="right">(1-26b)</div>

where v_{in} is the ion-neutral collision frequency, v_{ij} is the ion-ion collision frequency, and the summation is over ion species $j \neq i$. The electron momentum equation is:

$$0 = -\frac{1}{n_e m_e}\nabla P_e - \frac{e}{m_e}E - \frac{e}{m_e c}V_e \times B \qquad (1\text{-}26c)$$

The temperature equation is given by:

$$\frac{\partial T_i}{\partial t} + V_i \cdot \nabla T_i + \frac{2}{3}T_i \nabla \cdot V_i + \frac{2}{3}\frac{1}{n_i k}\nabla \cdot Q_i = Q_{in} + Q_{ii} + Q_{ie} \qquad (1\text{-}26d)$$

where the heating terms are due to ion-neutral collisions (Q_{in}), ion-ion collisions (Q_{ij}), and ion-electron collisions (Q_{ie}). SAMI2 uses a time-splitting scheme to solve the ion and electron equations: the dynamics of the system is first solved for motion along the geomagnetic field and then for motion transverse to the geomagnetic field.

Since SAMI2 is a stand-alone ionosphere model, it requires inputs for the neutral atmosphere and winds. The Mass Spectrometer Incoherent Scatter model (NRLMSISE00) [*Picone et al.*, 2003] is used to specify the neutral atmosphere. The

Horizontal Wind Model (HWM93) [*Hedin et al.,* 1996] specifies the neutral winds. An empirical model of the $\mathbf{E} \times \mathbf{B}$ drifts is also used [*Scherliess and Fejer,* 1999]. Figure 1-10 and Figure 1-11 are examples of SAMI2 electron densities.

Another model that is used in this work is the Global Assimilation of Ionospheric Measurements (GAIM), which uses a data assimilation technique to combine various measurements of the ionosphere with information taken from a time-dependent physics-based model of the ionosphere/plasmasphere [*Schunk et al.*, 2004]. In the absence of measurement data GAIM obtains its ionospheric specification from the Ionospheric Forecast Model (IFM), which is similar to SAMI2. With the addition of data, GAIM employs a Kalman filter, which performs a recursive least-squares inversion of all the observations for the model variable (e.g. electron density) using the model as a constraint. The result is an improved estimate of the model variable. Currently, GAIM is capable of assimilating GPS receiver data, DMSP in situ measurements of electron density as well as UV line-of-sight radiances. Electron densities are output on a three dimensional grid.

1.10 Ionospheric Research

By the middle of the twentieth century, the basic processes responsible for the formation of the ionospheric layers were well established. Over the next fifty years, major advances have been made in understanding the dynamics of the ionosphere and how it interacts with other regions of the atmosphere. Today, the climatology of the geomagnetically quiet ionosphere is fairly well understood and can be modeled with

37

some degree of success; however, predicting ionospheric weather is not yet possible [*Rodger and Jarvis*, 2000]. Weather refers to the conditions that deviate from monthly mean values.

Recent advances in ground and space based technology have lead to systems that are increasingly affected by space weather. Large geomagnetic storms are capable of having an adverse effect on power grids, satellite communications and GPS systems, to name a few. But problems are not limited to ionospheric conditions associated with storms. Any signals that must traverse the ionosphere can be affected by quiet time disturbances, such as spread *F* events, plasma bubbles and equatorial scintillation. Our increasing dependence on technology that is affected by ionospheric weather has led to a desire to be able to predict its behavior. This is the underlying motivation for much of the current ionospheric research. To better understand ionospheric weather, improved knowledge of the coupling between the neutral atmosphere and plasma transport processes is required [*Fejer*, 1997], and latitudinal, longitudinal and day to day variability must be addressed.

It is well known that under geomagnetically active and quiet conditions the ionosphere demonstrates considerable day to day variability, but the sources of this variability are not well understood. This was a topic that was actively pursued in the 1970s and was motivated by the desire for short term predictions of radio propagation conditions. For example, *Rush and Gibbs* [1973] used ionosonde data to determine the

variability of the ionospheric regions. It was found that the monthly median value of critical frequency of the *E* and *F*1 regions (*foE* and *foF1*, respectively) could be used to represent the daily variation of these regions; but the *F*2 region was found to be highly variable. Recently, *Forbes et al.* [2000] analyzed data from over 100 ionosondes over a 20 year period to quantify the *F* region ionospheric variability. Recent studies have shown that day to day variability of *NmF2* can be attributed to upward propagating tides. Planetary waves, with periods of about 2 to 30 days, are predominantly of tropospheric origin and can penetrate directly to ~100 km. Indirectly, their effects can be observed in the *F* region ionosphere (e.g., *Forbes and Zhang*, 1997; *Altadill and Apostolov*, 2001, 2003; *Lastovicka et al.*, 2003a, b). *Immel et al.* [2005], using the Far Ultraviolet Imager on board the IMAGE satellite, have shown that the equatorial anomaly exhibits longitudinal structure that is possibly due to tides originating in the troposphere.

Ionosonde data have proven useful for studies on ionospheric variability because they provide years of hourly data at various locations around the globe. But ionosondes only provide limited global coverage of the ionospheric conditions, with equatorial latitudes typically being underrepresented. Also, the ionosonde studies are limited to measurements of critical frequencies or peak ionospheric densities. With the advent of space based observations of the ionosphere we can now get a better global view of the structure of the ionosphere.

In this work, we use the LORAAS observations of the nighttime ionosphere to reconstruct electron densities in the low-latitude region. The LORAAS dataset provides us with global electron density profiles that will be used to quantify the variability of not only the peak electron density but the corresponding height of the F region. To date, there have been very few global studies of the variations in the height of the F region ionosphere in the low-latitude region (e.g. *Chandra et al*., 1975). The LORAAS datasets are also used to investigate the longitudinal variability of the ionosphere, specifically variability that is not attributed to the offset of the geomagnetic field from the geographic coordinates.

1.11 Scope of this Work

We first perform a case study of the longitudinal variability of the occurrence of scintillation in the low latitude ionosphere within a 24 hour period (Chapter 2) during geomagnetically quiet times. By studying the evolution of the TEC in the equatorial anomaly region in both a scintillating and non-scintillating longitude sector, we find evidence of longitudinal differences in the daytime and evening vertical plasma drifts that may affect the conditions for the occurrence of scintillation. Such longitudinal differences in the so-called "background" ionosphere, the large scale structure upon which irregularities occur, are also characteristic of the observed day to day variability of the ionosphere. Thus we were motivated to study the day to day variability of the equatorial anomaly region in more detail using UV remote sensing data that could also provide global coverage (Chapter 3). Two months (March 2001 and March 2002) of LORAAS

data are used to determine the day to day and longitudinal variability of the peak

densities, peak heights and separation of the equatorial anomaly crests on

geomagnetically quiet days in the post-midnight local time sector (0230 LT). We show

that the latitudes and separation of the anomaly crests are the most variable aspects of the

anomaly region (46-67% variation about the monthly mean), which indicates that the

$\mathbf{E} \times \mathbf{B}$ drifts vary significantly from one day to the next. We find that the height of the $F2$

peak density ($hmF2$) is the least variable feature, with less than 10% variation about the

monthly mean. We further demonstrate that the monthly mean values of the equatorial

anomaly features are in agreement with a climatology model (IRI-90).

Our results also show that the equatorial anomaly features vary with longitude. In

Chapter 4 we explore this variation in more detail and relate our results to recent

publications [e.g. *Immel et al.*, 2006] that suggest that a four-peaked wavelike variation

of the equatorial anomaly with longitude is due to the effects of atmospheric tides

originating in the troposphere on the daytime E region dynamo and hence the $\mathbf{E} \times \mathbf{B}$

drifts. We used the two months of LORAAS data analyzed in Chapter 3 along with

SAMI2 to investigate a wavelike pattern in the longitudinal variation of the peak

densities and latitudes of the anomaly crests. We show that there is a pronounced

hemispheric asymmetry in the wavelike pattern at ~0230 LT that is due to longitudinally

varying thermospheric winds in combination with well-known effects associated with the

offset of the geographic and geomagnetic equators. Our work implies that the F region

winds may be modulated by the same tides that affect the *E* region dynamo. We

summarize our findings in Chapter 5 and discuss areas of future study.

2 Longitudinal Variability of Equatorial Scintillation[1]

We investigate the longitudinal variability of equatorial scintillation under quiet magnetic conditions during March 22-23, 2002. SCINDA observations show intense activity in the South American-Atlantic sector during local evening hours, whereas an absence of scintillation is seen in the Far-East Asian sector. Ground and space-based measurements from SCINDA, GUVI, TOPEX and a chain of GPS receivers are used in combination with the USU-GAIM data assimilation model to explore the relationship between the large-scale ionization distribution and small-scale irregularities at low latitudes in both the scintillating and non-scintillating longitude sectors. Our analysis shows that there are significant differences in the evolution of the ionization distributions during the evening hours, which are likely the result of differences in the daytime and post-sunset vertical plasma drift in the two sectors. This study demonstrates the importance of USU-GAIM as a new tool for investigating longitudinal as well as day to day variability that is observed in the large-scale distribution of the ionosphere and how this relates to the occurrence of scintillation.

2.1 Introduction

Plasma density irregularities in the ionosphere can lead to rapid fluctuation or scintillation of satellite radio communication signals at or near the Earth's surface. Scintillation affects radio signals up to a few GHz in frequency and can seriously degrade or disrupt satellite based navigation and communication systems (some examples are shown in Figure 2-1). This can be particularly severe at night at low latitudes. To understand the occurrence of scintillation it is important to understand the large scale background ionospheric conditions on which plasma instabilities develop [*Basu and Basu*, 1985].
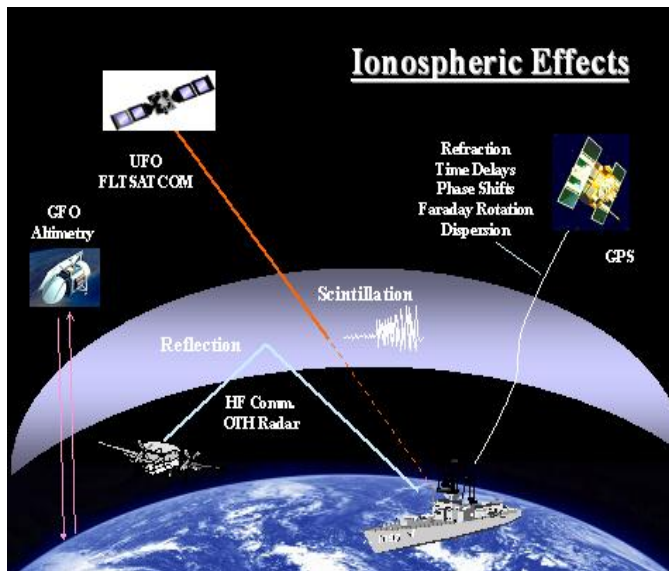
Figure 2-1 Examples of ionospheric effects on communication systems.

Atmospheric motions within the low-latitude thermosphere contribute to the formation of instabilities in the ionosphere that lead to irregularities in the plasma distribution [e.g. *Fejer and Kelley*, 1980; *Basu and Basu*, 1981; *Kelley*, 1989]. One of the most important processes that control the large-scale distribution of plasma is the vertical plasma drift that is driven by the complex interaction of *E* and *F* region electrodynamic processes [e.g. *Rishbeth*, 1971; *Heelis et al.*, 1974; *Richmond et al.*, 1976; *Stening*, 1981]. During the day an eastward electric field generated by dynamo action in the *E* region (90-120 km) causes a vertical $\mathbf{E} \times \mathbf{B}$ drift of *F* region plasma at the equator. In the late afternoon, when the *E* region density decreases, the *F* region dynamo becomes more significant. The *F* region dynamo, in conjunction with the conductivity gradient across the terminator, causes a post-sunset enhancement of the electric field and thus of the vertical plasma drift. The plasma rises until the pressure gradients are large enough that it diffuses down the magnetic field lines, assisted by gravity, toward tropical latitudes. The post sunset enhancement of the $\mathbf{E} \times \mathbf{B}$ drift has a significant effect since it causes the *F* layer plasma at the equator to be driven to very high altitudes, typically 500 km, where recombination is slow [*Hanson and Moffett*, 1966; *Anderson*, 1973a]. Regions of enhanced density, known collectively as the equatorial anomaly [*Appleton*, 1946], form at roughly ± 15° of the magnetic equator and often persist into the post-midnight hours. In the absence of sunlight, the lower ionosphere rapidly decays and a steep density gradient develops on the bottomside of the raised *F* region. This sets up the conditions for a gravitational Rayleigh-Taylor (R-T) instability to form. A small perturbation in the bottomside

density can lead to growth of the instability, resulting in plasma irregularities and the formation of "bubbles" (structures with depleted density) [e.g. *Kelly*, 1989]. The growth rate of the R-T instability is given by

$$\gamma = \frac{g}{L \nu_{in}}$$
(2-1)

where g is the acceleration due to gravity, ν_{in} is the ion-neutral collision frequency and L is the inverse gradient plasma scale length ($L = [(1/n)\, dn/dz]^{-1}$). Because the ion-neutral collision frequency decreases as a function of height, the higher the F layer the larger the instability growth rate. Thus, it is plausible that there is a direct connection between the strength of the post sunset enhancement of the $\mathbf{E} \times \mathbf{B}$ drift, which raises the F region, and the occurrence of scintillation.

There have been numerous studies that investigate the dependence of plasma irregularities on season, solar cycle, longitude, latitude and geomagnetic conditions and how they relate to ionospheric observables such as the post sunset enhancement of the $\mathbf{E} \times \mathbf{B}$ drifts and the location, height, and electron content in the equatorial anomaly region [e.g. *Walker and Chan*, 1970; *Aarons et al.*, 1980; *Maruyama and Matuura*, 1984; *Fejer et al.*, 1999; *Valladares et al.*, 2001; *Whalen*, 2001; *Hysell and Burcham*, 2002; *Anderson et al.*, 2004]. There is significant evidence for a close relationship between the vertical plasma drifts, the location of the anomaly crests, and

the occurrence of equatorial Spread-*F* (ESF) [*Fejer et al.*, 1999; *Whalen*, 2001; *Valladares et al.*, 2001; *Hysell and Burcham*, 2002]. *Basu et al.* [1996] conducted an equatorial campaign during September 25 – October 7, 1994 to investigate the day to day variability of the occurrence of ESF and found that during solar minimum a post sunset enhancement of the upward plasma drift on the order of ~ 20 m/s is necessary for the generation of irregularities. Recent results by *Anderson et al.* [2004] indicate that there indeed appears to be a threshold vertical velocity of ~ 20 m/s for strong scintillation, based on observations carried out in 1998 and 1999 in the Peruvian/Chilean longitude sector. The climatology of scintillation indicates that it is generally expected to occur at all longitudes on geomagnetically quiet equinoctial days during solar maximum [e.g. *Tsunoda*, 1985; *Basu and Basu*, 1985]. Despite significant advances in understanding the climatology of plasma irregularities, there remains considerable day to day variability that tends to contradict the climatology [*Tsunoda*, 2005].

The objective of this study is to make use of a diverse combination of space and ground-based data, along with a data assimilation model, to conduct a detailed investigation of the longitudinal variability in the occurrence of scintillation within a selected 24 hour period. With the combination of data and models, we are able to reconstruct the time evolution of the low-latitude plasma distributions in multiple longitude sectors in more detail than is possible with a single satellite or ground campaign. Though we are studying longitudinal variability of scintillation, we assume

47

that it is more closely related to the day to day variability than to other longitudinal effects such as the displacement of the geographic and geomagnetic equators.

We used UHF-band scintillation measurements from AFRL's Scintillation Network Decision Aid (SCINDA) [*Groves et al.*, 1997] to determine locations where UHF scintillation occurred on the night of March 22-23, 2002. We then collected and analyzed far-ultraviolet radiances from the Global Ultraviolet Imager (GUVI) [*Christensen et al*, 2003] aboard the NASA Thermosphere Ionosphere Mesosphere Energy and Dynamics (TIMED) satellite. Vertically integrated total electron content (*TEC*) measurements were obtained from several sources including: the dual-frequency radar altimeter aboard the NASA/Centre Nationale d'Etudes Spatiales TOPEX/Poseidon satellite [*Imel*, 1994], a chain of GPS receivers in South America [*Valladares et al.*, 2001], and individual GPS stations. The Utah State University (USU) GAIM (Global Assimilation of Ionospheric Measurements) model [*Schunk et al.*, 2004] was used to assimilate *TEC* data derived from globally distributed GPS measurements.

2.2 Data and Models

To find suitable days for the study, we used scintillation measurements obtained from the SCINDA system, which provides UHF-band (~250 MHz) and L-band frequency scintillation measurements from geostationary and GPS satellites at equatorial sites around the world [*Groves et al.*, 1997; *Caton et al.*, 2004]. We analyzed UHF-band data from 6 stations; three in the Far-East Asian sector

(Singapore, Manila and Guam) and three in the South American-Atlantic sector (Ascension Island, Ancon and Antofagasta). The SCINDA sites are shown in Figure 2-2. We chose March 22-23, 2002 because it was geomagnetically quiet and yet exhibited extreme differences in the occurrence of scintillation between the sectors. We were careful to select a period for the study with geomagnetically quiet conditions for at least 6 hours prior to dusk for each of the longitudes under investigation. The study spans from 0 UT on March 22 to 4 UT on March 23, 2002. During this time period the average 3-hour Kp is 1.2 and reaches a maximum of 3 early on March 22, 2002. The 10.7 cm solar radio flux value ($F_{10.7}$) is 170 and the 81-day average $F_{10.7}$ is 186.7.
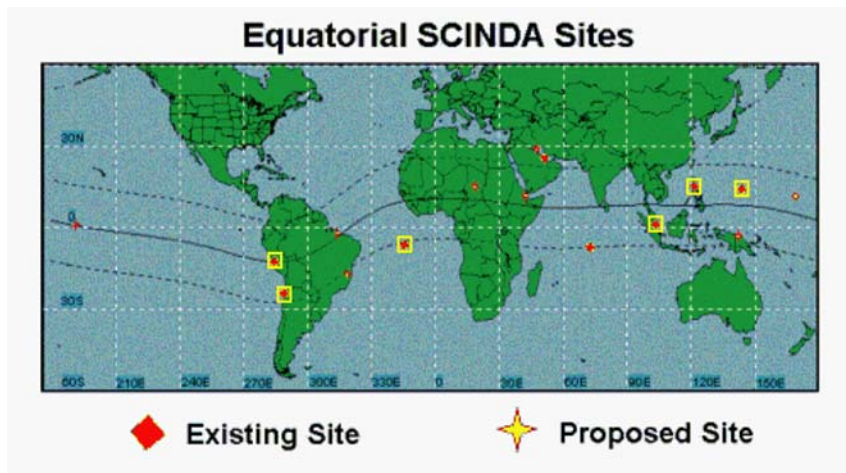
Figure 2-2 Equatorial SCINDA sites are located near the magnetic equator and anomaly regions. For this study, SCINDA data were obtained from the sites highlighted in yellow: Ancon, Antofagasta, Ascension Island, Manila, Singapore and Guam.

Figure 2-3 shows the S_4 index of scintillation as a function of time derived from UHF links at the six SCINDA stations. S_4 is defined as the normalized standard deviation of the signal intensity,

49

$$S_4{}^2 = \frac{\left\langle I^2 \right\rangle - \left\langle I \right\rangle^2}{\left\langle I \right\rangle^2} , \text{ where } I = \text{signal power.} \qquad\qquad (2\text{-}2)$$

The S_4 index is a metric for indicating the amount of variation in the amplitude of a signal, which in this case is due to electron density fluctuations. Noise in the data, manifested as sharp spikes extending beyond the plotting region, has not been removed. Each of the figures is labeled with the 350 km intersection longitude, which is the longitude at which the station to satellite line-of-sight intersects an altitude of 350 km, approximately the altitude of the peak of the F region. Time of sunset is marked with a red dashed line. Strong scintillation, starting after E region sunset and lasting well into the night, was detected at all three locations in the South American-Atlantic sector. No scintillation, however, was detected in Singapore or Manila, and only brief activity was detected in Guam. Though the Ancon and Antofagasta stations are at the same longitude, scintillation begins about 30 minutes earlier at Antofagasta because the observations are 6° east of the Ancon observations. Note that on average, scintillation is stronger in the equatorial anomaly region (Ascension Island, Antofagasta), where densities are enhanced, than at the magnetic equator (Ancon).
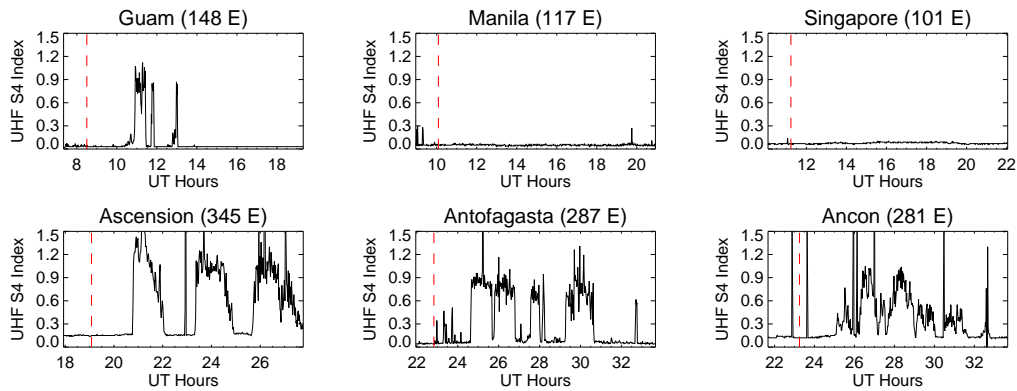
Figure 2-3 Plots of the S_4 index measured at several SCINDA stations on the evening of March 22-23, 2002. Each plot is labeled with the 350 km intersection longitude. The vertical dashed line indicates local sunset.

We used space and ground-based measurements of the ionosphere to obtain the *TEC* for extended latitude regions at specific longitudes and local times. The TOPEX/Poseidon satellite, launched in August 1992 and operational until January 2006, flew at an altitude of 1336 km with a 66° inclination and carried a dual-frequency radar altimeter operating at 13.6 GHz and 5.6 GHz. Vertical *TEC* estimates are given by the ionospheric range correction computed from the differences in the altimeter measurements [*Imel*, 1994] of the sea surface height. For purposes of comparison with GAIM, the TOPEX *TEC* measurements are averaged over 2° in latitude.

Additional space-based measurements were obtained from the GUVI instrument aboard the NASA TIMED satellite, which is in a 630 km circular polar orbit with a 74.1° inclination. GUVI collects spectral radiances of the Earth's far-ultraviolet airglow in the spectral region from 120 to 180 nm using a cross-track

scanning spectrometer [*Christensen et al*, 2003]; the scan begins on the antisunward

limb and scans onto the disk, covering 140° every 15 seconds. The radiance is

measured in five bandpass channels. In this study, we used the O I (135.6 nm)

channel radiances from the disk observations.

We estimate the nighttime *TEC* by first obtaining an average of the GUVI

intensities along the satellite track. The 14 pixels of O I (135.6 nm) channel of the

GUVI slit are averaged. Then we average the steps within 30° of the nadir position

(40 steps on either side of the nadir step). Next, we assume that the 135.6 nm radiance

is produced exclusively from the radiative recombination of O^+ ions (cf. Section 1.8)

and that the ion and electron densities are equal:

$$I(R) \cong 10^{-6} \alpha_{135.6} \int_0^\infty n_e^2 dz \qquad\qquad (2\text{-}3)$$

The intensity, *I,* is measured in Rayleighs and the electron density is given by n_e. The

effective 135.6 nm recombination rate coefficient ($\alpha_{135.6}$) is 7.3 x 10^{-13} cm^3 s^{-1} at

1160 K and varies with electron temperature as $(1160/T_e)^{\frac{1}{2}}$ [*Meléndez-Alvira et al.,*

1999]. We assume a Chapman layer representation of the electron density profiles

[*Chamberlain and Hunten,* 1987]. The Chapman model uses three parameters to

characterize the ionosphere: the peak density, *NmF2*; the height of the peak density,

hmF2; and the O scale height, H_o, which is one-half the plasma scale height. The

Chapman function (cf. Section1.3) for describing the electron density, $n_e(z)$ is given

by Equation 1-7. We express it again here in terms of the three Chapman parameters:

$$n_e(z) = NmF2 \exp\left\{ \frac{1}{2}\left[1 - \frac{z - hmF2}{H_O} - \exp\left(-\frac{z - hmF2}{H_O} \right) \right] \right\} \qquad (2\text{-}4)$$

where z is the altitude. Substituting equation (2-4) into equation (2-3), performing the

integration of equation (2-3) and solving for the peak density, we obtain

$$NmF2 = \sqrt{\frac{I(R) \times 10^6}{\alpha_{135.6} H_O e}} . \qquad (2\text{-}5)$$

Next, we solve for *TEC* by integrating n_e over *z*:

$$TEC = \int_0^\infty n_e \, dz \qquad (2\text{-}6)$$

to obtain

$$TEC = H_O NmF2 \sqrt{2\pi e} \qquad (2\text{-}7)$$

53

We substitute equation (2-5) into (2-7) to arrive at the expression for *TEC* in terms of the

radiance, *I*, and the scale height, H_O:

$$TEC = 10^{-12} \sqrt{\frac{2\pi H_O I(R) \times 10^6}{\alpha_{135.6}}} \qquad (2\text{-}8)$$

We have divided by a factor of 10^{12} to express the *TEC* in units of *TEC* (TECU),

where 1 TECU = 10^{12} electrons/cm^2. Also, since we do not know the scale height,

H_O, we assume it is 70 km.

Ground-based *TEC* measurements were gathered from a chain of 11 dual-

frequency GPS receivers located near the west coast of South America, which span

latitudes from 9° N to 40° S (Figure 2-4). (Data were provided courtesy of Cesar

Valladares of Boston College.) The *TEC* measurements provided for this study have

been corrected for transmitter and receiver biases, multipath, and cycle slips.

Additionally, data were eliminated when cycle slips had not been corrected, or when

unreasonably large values of *TEC* were obtained [*Valladares et al.*, 2001].
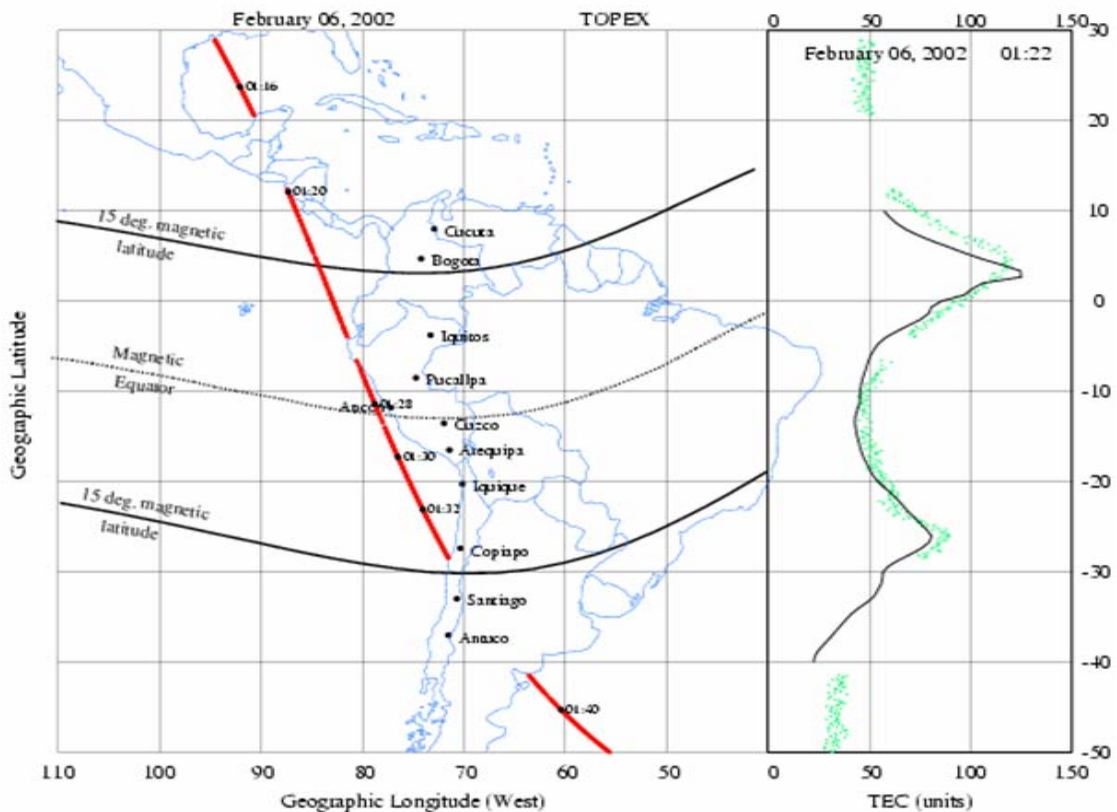
Figure 2-4 The South American GPS-chain consists of 11 receivers distributed across the equatorial anomaly region. The red line shows an overpass of TOPEX. To the right is a comparison of the GPS-chain *TEC* (in black) to that of TOPEX (in green).

The data alone do not provide sufficient longitudinal or temporal coverage of the large scale background ionospheric conditions that existed on March 22-23, 2002. To investigate the differences between the scintillating and non-scintillating longitude sectors, we use the USU-GAIM data assimilation model. The model uses a time-dependent physics-based model of the global ionosphere and a Gauss-Markov Kalman Filter as a basis for assimilating diverse sets of observations [*Schunk et al.*, 2004]. The physics-based model is the Ionospheric Forecast Model (IFM), which accounts for five ion species and covers the *E* region, *F* region and the topside

ionosphere over an altitude range from 90 to 1400 km. Within the Kalman Filter, the IFM derived ionospheric densities constitute a background density field on which perturbations are superimposed. The USU-GAIM model was run for the March 22-23, 2002 time period; it assimilated slant GPS/TEC data from ~300 world-wide GPS receivers (Figure 2-5), bottomside electron density profiles from two ionosondes, and nighttime line-of-sight UV radiances from the Low Resolution Airglow and Aurora Spectrograph (LORAAS) aboard the Advanced Research and Global Observing Satellite (ARGOS) [*McCoy et al*., 1992]. (USU-GAIM model results were provided courtesy of Ludger Scherliess of Utah State University.)
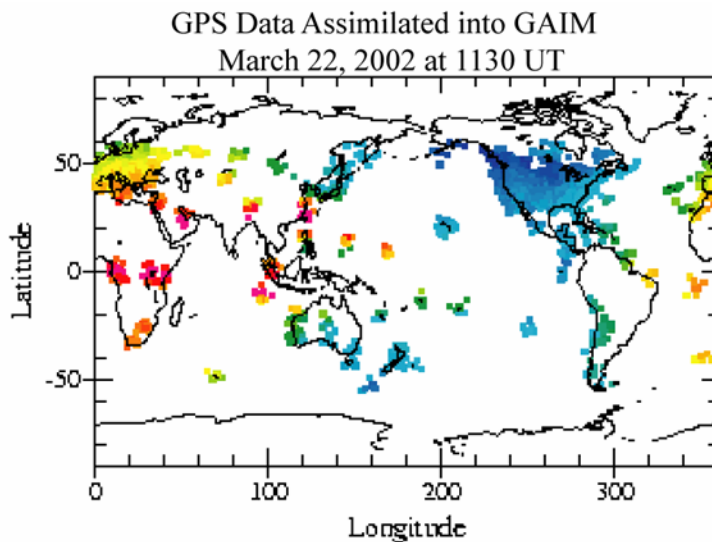
Figure 2-5 Map of the GPS data coverage for March 22 at 1130 UT. Vertical *TEC* data are shown at their 300 km pierce points. This map shows the density of data that is assimilated into GAIM.

2.3 Results and Discussion

Figure 2-6 shows the composite GUVI disk-scan images in the O I 135.6-nm band on the evening of March 22-23, 2002; the local time of the observations was 2330 LT. Time progresses from right to left, with the UT of the magnetic equator crossing of GUVI listed along the top of the image. Also indicated are the magnetic equator and SCINDA sites that are used in this study. The bright features on either side of the magnetic equator are the equatorial anomaly crests. The dark bands through these enhanced intensity regions are ionospheric depletions, or "bubbles", caused by plasma instabilities. Satellite signals crossing through these depleted regions will be significantly degraded. This composite image shows very clearly the longitudinal variability implied by the SCINDA data. The anomaly crests show no evidence of depletions in the Far-East Asian sectors (170°E to 80°E), but large-scale irregularities are present from the west coast of India to the American sector (50°E to 250°E).
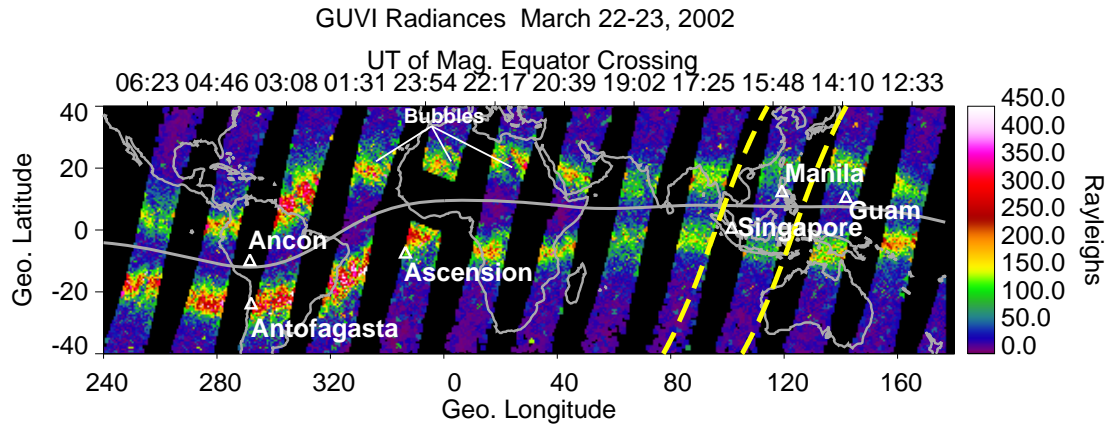
Figure 2-6 TIMED GUVI OI (135.6 nm) channel night-side disk images for March 22-23, 2002, where the GUVI slit is projected to an altitude of 300 km. Time (UT) progresses from right to left. The TOPEX paths in the Far-East Asian sector are also shown (yellow dashed lines). SCINDA stations are also indicated (triangles).

Next, we look more closely at the large scale plasma distributions in the Far-East Asian and the South American-Atlantic sector. As mentioned in the previous section, the GUVI and TOPEX data alone cannot provide sufficient insight into the evolving post-sunset ionosphere. The TOPEX and GUVI data (at 2240 LT and 2330 LT respectively) provide only a snapshot of the ionosphere well after the conditions for scintillation are set. Ideally, we would use the GAIM model to provide the ionospheric specification at earlier times.

In Figure 2-7 we show that GAIM reproduces the TOPEX and estimated GUVI disk-scan *TEC*s quite well in the Far-East Asian sector on March 22, 2002. Also shown in Figure 2-7 are the results for IFM, which are the model results obtained in the absence of data assimilation. Note that the "weather" results provided by GAIM are a significant improvement over the climatology predicted by IFM. In

the South American-Atlantic sector the situation is different. Here, the GPS data are affected by the strong occurrence of bubbles during the evening hours of March 22, 2002. GAIM, in its current mode, uses a built-in GPS-TEC preprocessor that discards any GPS data that are affected by either ionospheric bubbles or large phase slips. This limitation of GAIM, which will be overcome in future versions of the model, prevents us from using the GAIM results in the South American-Atlantic sector during the evening hours of March 22, 2002. As an alternative, the GAIM results are used to provide *TEC*s in the Far-East Asian sector, and the South American chain of GPS receivers are used to provide *TEC*s at the times the GAIM results are unavailable. Due to the close proximity of the GPS-chain receivers, additional processing is performed on this dataset in order to remove the effects of the bubbles.
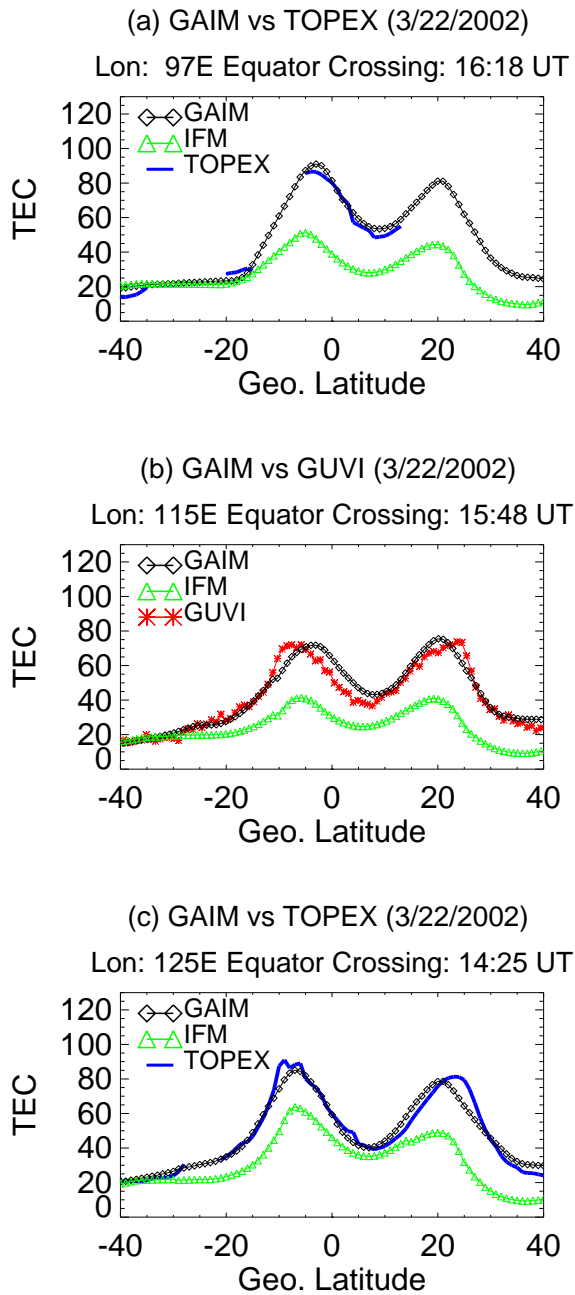
Figure 2-7 Comparisons of GAIM to GUVI and TOPEX TECs on March 22-23, 2002. IFM model results are also shown.

Figure 2-8 shows a comparison of the *TEC* at two longitudes: one in the non-scintillating Far-East Asian sector (127°E) and the other in the scintillating South

American sector (288°E). Figure 2-8a shows the evolution of the equatorial anomaly

region from 1800 LT to midnight at 127°E longitude. From 1800 LT to 2000 LT, the

crests move slightly poleward. Since the anomalies are already quite prominent

before sunset the post-sunset vertical plasma drift has little effect in the crest regions.

The evolution of the *TEC* distributions at 288°E longitude, on the other hand, show

the typical characteristics of a post-sunset enhancement of the equatorial anomaly.

The large ratio of *TEC* at the crests and trough probably arises from the action of the

enhanced zonal electric field at the time of sunset that uplifts the plasma at the

magnetic equator which then diffuses down the magnetic field lines. Between 1800

and 2000 LT, the anomaly crests increase in strength and move farther apart (Figure

2-8b). In fact, the anomaly crests do not begin to decay until nearly midnight.
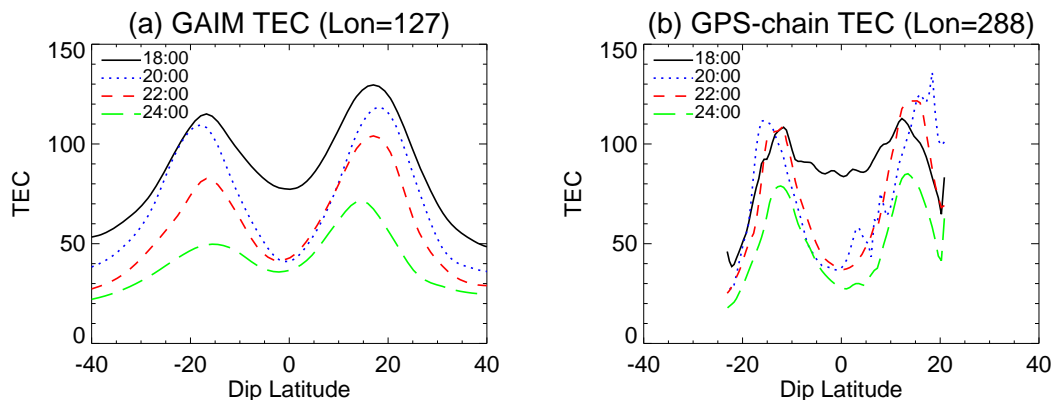
Figure 2-8 a) Computed TECs from the GAIM model near the Manila longitude on March 22, 2002. b) TECs at the same local time in the S. American-Atlantic sector on the same night (March 22-23, 2002).

The differences in the evolution of the TECs in the two longitude sectors are

the result of differences in the strengths of the daytime and the post-sunset vertical

plasma drifts, as well as the duration of the upward drifts, at the two locations. In general, longitudinal variations in vertical drift velocities can be attributed to the differences in the alignment of the sunset terminator with the local magnetic meridian as a result of longitudinal changes in magnetic declination [*Batista et al.*, 1986; *Abdu et al.*, 1992]. But various measurements have shown that the vertical drift velocities are largely independent of longitude near the equinoxes [e.g. *Coley et al.*, 1990; *Fejer et al.*, 1995; *Fejer et al.*, 1996]. On the other hand, ground and space-based measurements of vertical drifts indicate considerable day to day variability [e.g. *Fejer et al.*, 1995; *Fejer and Scherliess*, 2001] that is likely due to meteorological influences from the lower atmosphere, such as upward propagating tides [*Richmond*, 1995]. More extensive studies are needed to better understand the coupling of the lower atmosphere to the variability observed at *F* region heights.

Certainly, the vertical plasma drifts in the South American sector had a greater effect on the early evening structure of the anomaly region than the drifts in the Far-East Asian sector. The fact that the anomaly crests decayed much more quickly in the Far-East Asian sector indicates that the drifts turned downward at an earlier time than in the South American sector. It is possible that a larger peak vertical drift velocity in the South American sector, along with a later reversal, led to the favorable conditions for scintillation, whereas a threshold velocity may not have been attained in the Far-East Asian sector. *Fejer et al.* [1999], for example, found that in the South American sector during solar maximum and low magnetic activity, strong equatorial Spread-*F*

occurs when the peak vertical drift velocities exceed 55 m/s. Other results, however, indicate that a peak velocity of only ~20 m/s is necessary [*Basu et al*., 1996; *Anderson et al*., 2004]. The need for seed perturbations at such times cannot be overlooked and clustered measurements may be necessary to resolve this issue [*Tsunoda*, 2005].

2.4 Conclusion

In this study we have shown that there exists significant longitudinal variability in the occurrence of scintillation over a 24 hour period under geomagnetically quiet conditions. Two sectors were analyzed in detail; one of the sectors exhibited strong equatorial scintillation (South American-Atlantic) and the other (Far-East Asian) exhibited no scintillation. Together, the SCINDA and GUVI data show that the occurrence of ionospheric depletions or "bubbles" is correlated with strong scintillation activity.

We have also shown that USU-GAIM data assimilation model is capable of reproducing the large-scale variability observed in the low-latitude plasma distribution provided that there is sufficient data coverage and that the data are not contaminated by ionospheric bubbles. The USU-GAIM model reproduced quite well the *TEC*s observed by GUVI and TOPEX in the Far-East Asian sector. However, the model can not be used to specify the background ionosphere in the South American-Atlantic sector after the onset of scintillation and occurrence of bubbles in this region.

By comparing the *TEC*s derived from the South American chain of GPS receivers to the USU-GAIM results in the Far-East Asian sector, we have shown that the combination of data and assimilation models can serve as a powerful tool for investigating the global time evolution of large-scale plasma distributions. Our analysis of the two sectors has shown that there were significant differences in the evolution of the *TEC* distributions from 1800 LT to 2400 LT, which were likely the result of differences in the daytime and post-sunset vertical plasma drifts in the two sectors. Previous studies have shown that such differences in plasma distributions are observed on a day to day basis in a single longitude sector [e.g. *Valladares et al.*, 2001]. We have shown that similar differences are observed in different longitude sectors on the same day. The results of our study did not clearly indicate why scintillation was not observed in the Far-East Asian sector on March 22, 2002. Other processes not directly observable in the large-scale background ionosphere, such as perturbations on the bottomside *F* region, may play a significant role in the occurrence of scintillation [*Tsunoda*, 2005]. Additional measurement will need to be performed in order for this issue to be resolved. Our work raises additional questions concerning the scale lengths of ionospheric disturbances. In order for data assimilation forecasting models to be accurate, additional studies must be conducted to understand the scale lengths of the various physical processes that contribute to scintillation.

Our limited study shows that USU-GAIM, with the additional assimilation of suitable datasets, will be an important tool for providing insight into the causes of the observed day to day and longitudinal variability of ionospheric weather. The ability of USU-GAIM to provide a specification of the background ionosphere that is far more accurate than that provided by current climatology models will prove useful to the Communications/Navigation Outage Forecasting System (C/NOFS) mission [*de la Beaujardière et al.*, 2004], whose science objectives includes obtaining a better understanding of the equatorial ionosphere at all local times and, in particular, how plasma bubbles form.

3 Day to Day Variability of the Equatorial Anomaly

The Low Resolution Airglow and Aurora Spectrograph (LORAAS) has collected

numerous spectra of Earth's airglow in the 80.0 – 175.0 nm wavelength region during its

mission, which began in May 1999 and ended in April 2002. The intensity of nighttime

O I 135.6 nm emission associated with the equatorial anomaly is measured and

interpreted using a quasi-tomographic technique to invert the intensity scans to derive

electron density profiles of the ionosphere. In this study, reconstructed electron density

profiles from two months of LORAAS data are used to determine the separation, peak

heights, and peak densities of the northern and southern anomaly crests at approximately

0230 LT. We observe that even under relatively quiet conditions there are significant day

to day and longitudinal variations in the equatorial ionosphere. We quantify the day to

day variability of the equatorial anomaly crests in 15 longitude sectors and compare our

results with an empirical model of the ionosphere.

3.1 Introduction

Since the early days of ionospheric exploration, it has been well known that the

ionosphere is a highly variable component of the Earth's atmosphere. Because the

ionosphere plays an important role in radio communication, the causes of variability and

its prediction have been areas of research for several decades. Today, in addition to high frequency (HF) communications (both commercial and military), there are an increasing number of satellites whose transmissions through the atmosphere can be severely impacted by the ionosphere. For example, ionospheric disturbances can cause errors in the Global Positioning System. In response to the growing communication needs, space weather specification and forecasting have emerged as active areas of research, making it even more important to understand ionospheric variability.

The ionosphere lies at the boundary between the dense neutral atmosphere below and the magnetosphere above, which couples to the solar wind and interplanetary magnetic field (IMF). The strong coupling of the ionosphere to these regions is manifested as structural variation that occurs on global scales down to the mesoscale and timescales ranging from years to days, hours or even minutes. Sources of the non-polar ionospheric variability can be broadly categorized as originating from solar ionizing radiation, solar wind conditions (or geomagnetic activity), and meteorological influences. A fourth category, electrodynamics, also accounts for observed variability, though these processes can be derived from the other three. Table 3-1 lists the possible causes of ionospheric variability.

Table 3-1 Possible causes of ionospheric F-region variability.

1. Solar Ionizing Radiation	3. Meteorological influences
Solar flares	Solar and lunar tides; generated within thermosphere or coupled through mesosphere
Solar rotation (27 day) variations	Acoustic and gravity waves
Formation and decay of active regions	Planetary waves and 2-day oscillations
Seasonal variation of Sun's declination	Quasi-biennial oscillations
Annual variation of Sun-Earth distance	Lower atmosphere weather coupled through mesopause
Solar cycle variations (11 years)	Surface phenomena: earthquakes, volcanoes
Longer period solar epochs	
Solar zenith angle	
Solar flux-induced variations in neutral composition, temperatures, winds and conductivities	
2. Solar wind, Geomagnetic activity	**4. Electrodynamics**
Day-to-day 'low level' variability	Dynamo 'fountain effect' at low latitudes
Substorms	Penetration of magnetospheric electric fields
Magnetic storms	Plasma convection at high latitudes
IMF/solar wind sector structure	Field-aligned plasma flows to and from plasmasphere and protonosphere
Energetic particle precipitation, Joule heating	Electric fields from lightning and sprites

Under both geomagnetically active and quiet conditions, the ionosphere demonstrates considerable day to day variability. This was a topic that was actively pursued in the 1970s and was motivated by the desire for short term predictions of radio propagation conditions. For example, *Rush and Gibbs* [1973] used ionosonde data to determine the day to day variability of the ionospheric regions. It was found that the monthly median value of critical frequency of the *E* and *F*1 regions (*foE* and *foF1*, respectively) could be used to represent the daily variation of these regions. But the *F*2 region was found to be highly variable; the standard deviation from the mean *foF2* was three times higher than for the lower regions.

There have been numerous studies of the day to day variability of total

ionospheric electron content (*TEC*) obtained from measurements of the Faraday rotation

of radio beacons on geostationary satellites. Specifically, the beacons aboard the

Applications Technology Satellite series of six geostationary satellites launched from

December 1966 to May 1974 were used to obtain *TEC* measurements. *Rastogi and Alex*

[1987], *Aravindan and Iyer* [1990], *Aravindakshan and Iyer* [1993] all used signals from

ATS-6 to study day to day variability in the equatorial and low-latitudes in India.

Aravindan and Iyer [1990] found that variability is low (10 – 25%) by day and higher (30

– 40%) at night. Variability is lowest (< 15%) at the magnetic equator and highest (26%)

near the anomaly crest. They also showed that the strength of the electrojet has a

dominant effect on the day to day variability of the *TEC* near the anomaly crests and

established a linear relationship between the two. It was also found that *foE* is less

variable than *TEC* or *foF2*, indicating the greater influence of ionospheric dynamics on

the upper region of the ionosphere. *Rastogi and Alex* [1987] found that *TEC* varied from

10 – 25% during the day and from 40 – 60% during the night, with the largest variability

occurring near the anomaly crests.

A number of other studies have been conducted that use critical frequencies from

globally distributed ionosondes. For example, *Forbes et al.* [2000] analyzed data from

over 100 ionosondes over a 20 year period to quantify the *F* region ionospheric

variability and to determine to what degree the variability is attributed to various sources.

Under quiet conditions (Kp < 1), the one sigma (1σ) variability of *NmF2* about the mean

is 25 – 35% over a period of a few hours to 1 to 2 days and 15 – 20% over 2 to 30 days at all latitudes. This represents variability due to meteorological influences. For high frequencies, *NmF2* was found to be the most variable at the anomaly crest latitudes; the authors suggest that these results may reflect the sensitivity of anomaly crest densities to day to day variations in *F* region winds and electric fields driven by the *E* region wind dynamo.

Rishbeth and Mendillo [2001] studied the day to day *F*2 layer variability by analyzing 34 years of ionosonde data from thirteen stations. They defined quantitative descriptions of variability versus local time, season and solar cycle. On average, it was found that for years of medium solar activity, where the 10.7 cm solar radio flux index ($F_{10.7}$) is 140 W m^2 Hz^{-1}, the daily fluctuations of *NmF2* have a standard deviation of 20% by day and 33% by night. A large part of the variability is linked to geomagnetic activity and the rest is attributed to meteorological sources at lower levels in the atmosphere. They suggest that the variability at night, in the upper-midlatitudes, is due to enhanced auroral energy input and lack of strong photochemical control of the *F*2 layer that exists during the day. They found that the equinoxes exhibit the greatest variability. *Kouris* [2002] also found that deviations of *foF2* are within 20% about 85 – 90% of the time, with higher variability (up to 30 – 40%) on the day/night boundaries, at night and during equinox months. Similar results were obtained by *Araujo-Pradere et al.* [2004] and *Bilitza et al.* [2004], who also found that low latitudes show higher variability.

The advantage of using ionosonde or beacon data to perform studies on ionospheric variability is that they provide years of hourly data at various locations around the globe. But ionosondes only provide limited global coverage of the ionospheric conditions, with equatorial latitudes typically being underrepresented. Also, the ionosonde studies are limited to measurements of critical frequencies or peak ionospheric densities. With the advent of space-based observations of the ionosphere we can now get a better global view of the structure of the ionosphere. Additionally, two-dimensional images of the ionosphere can be reconstructed tomographically to obtain improved spatial resolution of the ionosphere.

In this study we use the LORAAS limb scans of O I 135.6 nm emission features to tomographically reconstruct the low-latitude ionosphere. The resultant images are used to investigate the nighttime day to day variability of the low latitude ionosphere at all longitudes. Our analysis uses two equinox months (March 2001 and March 2002) of LORAAS data taken at ~0230 LT. We investigate the variability of the main features of the equatorial anomaly, which include the peak electron densities in the anomaly crests, the heights of the peak densities, and the separation of the anomaly crests. In Section 3.2, we describe the ARGOS satellite UV observations and the technique used to obtain electron density profiles. In Sections 3.3 and 3.4, we compare the LORAAS densities with other observations. In Section 3.5, we analyze the day to day and longitudinal variability of the equatorial anomaly region for March 2002. Our results are compared

71

with an empirical model of the ionosphere in Section 3.6. We summarize the work and present our conclusions in Section 3.7.

3.2 LORAAS Observations and Data Analysis Technique

The High Resolution Airglow and Aurora Spectroscopy (HIRAAS) experiment was launched aboard the United States Air Force (USAF) Space Test Program's Advanced Research and Global Observation Satellite (ARGOS) on February 23, 1999 and continually observed the ionosphere and neutral thermosphere until early April 2002. The satellite was placed into a sun-synchronous orbit at 98° inclination at an altitude of approximately 830 – 850 km and a local time of 0230/1430. The HIRAAS consisted of three limb scanning spectrographs, shown in Table 3-2. The High Resolution Ionospheric and Thermospheric Spectrograph (HITS) covered the far and extreme ultraviolet regime (50 – 150 nm) in 12 nm segments with a 0.06-0.11 nm spectral resolution. The Ionospheric Spectroscopy and Atmospheric Chemistry (ISAAC) spectrograph covered the mid-ultraviolet regime (180 – 320 nm) in 40 nm segments with a 0.38 nm spectral resolution. The Low Resolution Airglow and Aurora Spectrograph (LORAAS), an extreme and far ultraviolet spectrograph, operated in the 80 – 175 nm passband with a 1.8 nm spectral resolution. The HIRAAS instruments are described in more detail by *Dymond and McCoy* [1993], *McCoy et al.,* [1992, 1994].

Table 3-2 HIRAAS instruments

Instrument	Passband	Spectral Resolution	Field of View
HITS	50-180 nm	0.06 - 0.11 nm	4.6° x 0.06°
LORAAS	80-175 nm	1.8 nm	2.4° x 0.15°
ISAAC	180-320 nm	0.38 nm	1.1° x 0.034°

The LORAAS sensor was a prototype of the Special Sensor Ultraviolet Limb Imagers (SSULIs) that are scheduled to fly on the USAF Defense Meteorological Satellite Program (DMSP) Block 5D-3 satellites in the $2003 - 2012$ timeframe. The LORAAS viewed aft in the orbital plane and observed ultraviolet emissions on the Earth's limb by scanning in the instrument's field-of-view from the satellite's local horizon to the edge of the Earth's surface, as illustrated in Figure 3-1. The instrument had a horizontal by vertical field-of-view of $2.4° \times 0.15°$ and swept out a $2.4° \times 17°$ field-of-regard during each 90 second scan, covering tangent altitudes of 750 km to 75 km (Figure 3-2). Approximately 90 spectra, with one-second integration, were gathered per limb scan, covering 5° to 6° latitude.
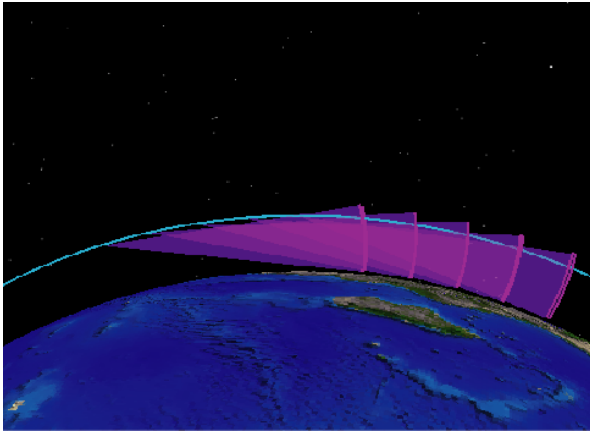
Figure 3-1 Illustration of consecutive LORAAS limb scans. Here, the satellite is moving from right to left and scans zenith angles from 96˚ to 117˚.
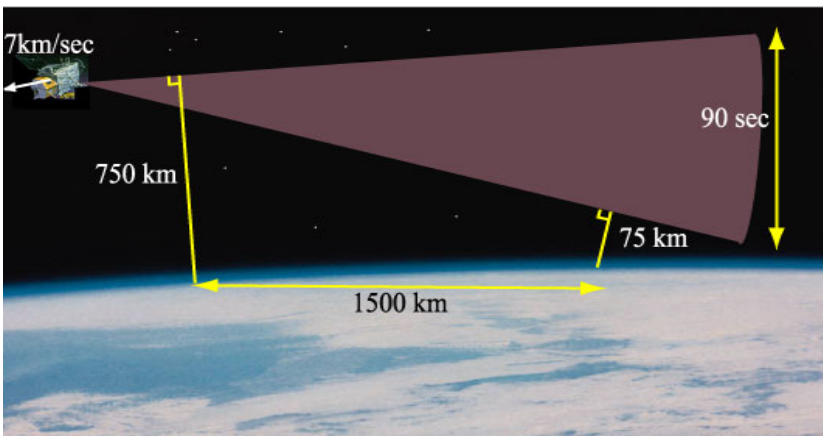
Figure 3-2 An illustration of the LORAAS 2.4˚ x 17˚ field-of-regard. The instrument scans tangent altitudes from 750 to 75 km during a 90 second period.

Figure 3-3 shows an image from a typical nighttime limb scan. The emission features visible in the image are O I 91.1 nm, H I 121.6 nm (Lyman-α), and O I 135.6 nm. Other emission features in the bandpass that are too faint to see include O I 102.6 nm, H I 102.7 nm (Lyman-β), and O I 130.4 nm. The LORAAS detector

74

included a low sensitivity region from 120 to 133 nm in order to suppress the signal from the brightest airglow features.
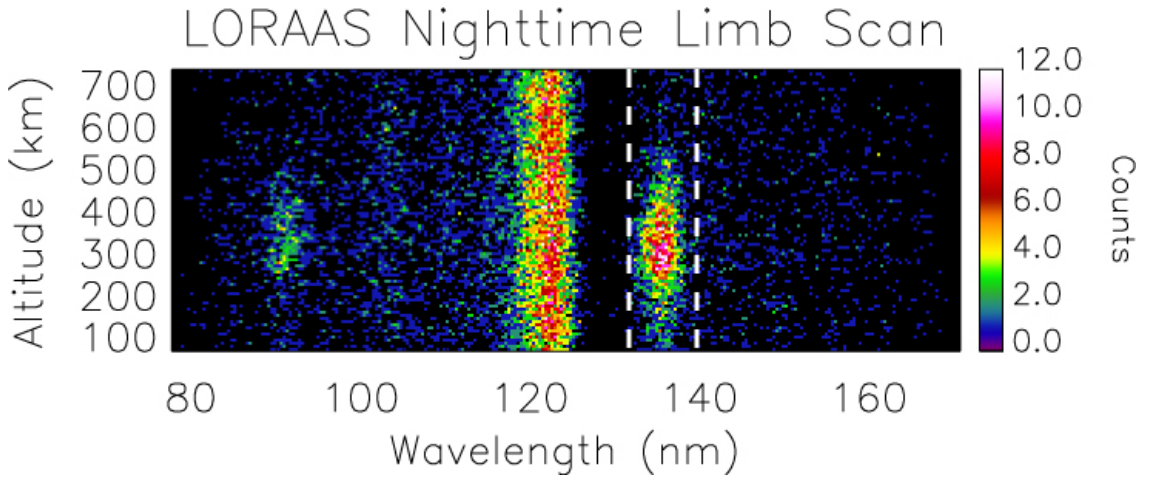
Figure 3-3 A typical nighttime limbscan (0230 LT). The brightest feature is the Lyman-α (121.6 nm), followed by O I (135.6 nm) and O I (91.1 nm). The region within the dashed lines is summed to determine the total counts for the 135.6 nm feature.

We use the LORAAS instrument to measure the intensity of the nighttime O I 135.6 nm emission feature, which is produced primarily by radiative recombination (cf. Section 1.8). We use many of the same assumption and equations that we applied to the GUVI observations (discussed in Section 2.2) and will restate them here. We assume the 135.6 nm feature at night is optically thin and that contamination due to $O^+ - O^-$ neutralization is negligible. *Meléndez-Alvira* [1999] showed that mutual neutralization contributes up to 11% of the total intensity at tangent altitudes near 275 km in the early evening, but that it is lower at higher altitudes. The 91.1 nm feature is not used in this study because it often had a poor signal-to-noise ratio. Limb profiles of the 135.6 nm emissions are produced by summing the counts in the region surrounding the emission

feature, as indicated by the dashed lines in Figure 3-3. An adjacent region is then

subtracted from the profile in order to remove the background noise. The limb profiles

are then converted to radiance units by dividing by the instrument's sensitivity at

135.6 nm. The LORAAS sensitivity for March 2001 and March 2002 were determined to

be 0.18 and 0.20 counts s^{-1} Rayleigh^{-1} respectively. A stellar detection technique was

used to determine the sensitivity and is described in *Budzien et al.* [2002]. A typical limb

profile is shown in Figure 3-4.

OI 135.6nm Intensity
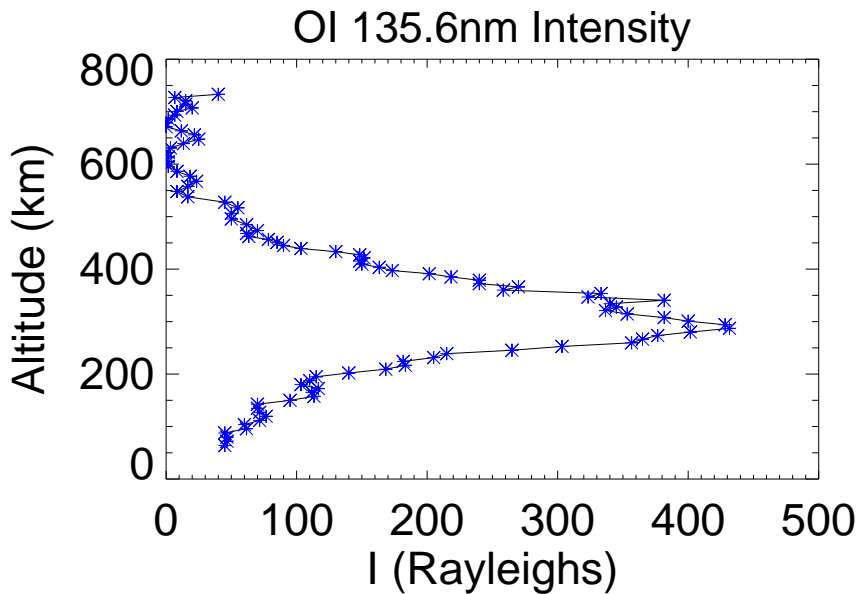
Figure 3-4 Typical O I (135.6 nm) LORAAS limb profile in the equatorial anomaly region. (9 March 2002 at Lat=25°, Lon=127°, 0247 LT)

The set of intensity profiles for a nighttime pass across the low-latitude and

equatorial region can be represented as an image as shown in Figure 3-5. The image is a

76

composite of consecutive 135.6 nm intensity profiles, where the y-axis represents the altitude in kilometers and the x-axis represents the dip latitude in degrees. The brightest features in the image are the aurora in the southern hemisphere and the equatorial anomaly, which appears as two features at -15° and +20° latitude and an altitude of ~300 km. The geometry of the raw limb scans causes the anomalies to appear distorted, with emission features appearing higher or lower in altitude than expected.
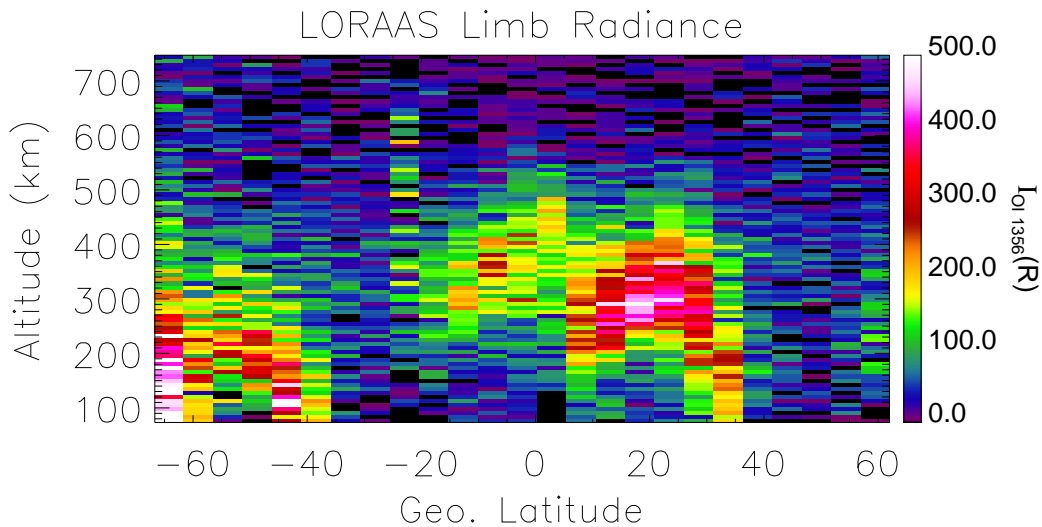
Figure 3-5 Consecutive LORAAS nighttime limb profiles of O I (135.6 nm) on 9 March 2002 (Lon=121° at 0230 LT). The northern and southern equatorial anomaly crests are clearly visible at 20° and -15° latitude respectively. The enhancement observed south of -40° latitude is due to aurora.

A two-dimensional tomographic technique is used to invert the intensity scans to derive the electron density profiles of the F layer ionosphere in the equatorial anomaly region. It is assumed that the electron density equals the O^+ density:

$$I(R) \cong 10^{-6} \alpha_{135.6} \int_{0}^{\infty} n_e^2 dz \qquad\qquad (3\text{-}1)$$

which is approximately correct below the H^+/O^+ transition height in the nighttime F region. We have used SAMI2 to determine that the H^+/O^+ transition height is ~1200 km in the low latitude ionosphere for the average conditions of our observations. The effective recombination rate coefficient ($\alpha_{135.6}$) is 7.3×10^{-13} cm^3 s^{-1} at 1160° K and varies with electron temperature as $(1160/T_e)^{1/2}$ [*Meléndez-Alvira et al.*, 1999]. Since the density is proportional to the square root of the intensity, the density scales as $T_e{}^{1/4}$. To determine the approximate electron temperature at 0230 LT in the low-latitude ionosphere, we use an empirical model of the ionosphere, the International Reference Ionosphere (IRI-90). Based on this model, we assume the electron temperature is isothermal at 1050° K during the data accumulation, which results in less than 3% error in the electron density per 100° K change in temperature.

We assume a three parameter Chapman layer representation of the O^+ and electron density profiles [*Chamberlain and Hunten,* 1987]. Recall from Section 2.2 that the Chapman model (Equation 2-3) uses three parameters to characterize the ionosphere: the peak density, *NmF2*; the height of the peak density, *hmF2*; and the O scale height, H_o, which is one-half the plasma scale height. The Chapman function for describing the O^+ density, $n_{O+}(z)$ as a function of altitude z is given by:

$$n_{O^+}(z) = NmF2 \exp\left\{ \frac{1}{2}\left[1 - \frac{z - HmF2}{H_O} - \exp\left(-\frac{z - HmF2}{H_O} \right) \right] \right\}. \qquad (3\text{-}2)$$

The inversion algorithm is based on discrete inverse theory and uses the iterative Levenberg-Marquardt scheme to seek a maximum likelihood estimate (minimum of the Chi-Squared statistic) of the ionospheric parameters based on the fit of the model to the data [*Dymond and Thomas*, 2001]. A model covariance matrix is also calculated, which is based on the counting statistics and the model used to fit the data. The two-dimensional inversion algorithm requires the addition of a regularization parameter to control the amplification of noise in the retrieval process [*Dymond and Thomas*, 2001]. Details related to our implementation of regularization along with the method used to determine the "optimal" regularization weight are provided in the Appendix. We found that a single regularization weight could be used for all of the March 2001 and March 2002 retrievals, which vastly reduced the computational time to process the LORAAS data. However, this "optimal" regularization weight occasionally overly smoothed the retrieved densities.

Figure 3-6 shows the electron density profiles that have been reconstructed from the 2-D inversion of the intensity profiles illustrated in Figure 3-5; the three Chapman parameters are also plotted as a function of latitude. Fewer limb scans are represented in the density image than in the intensity image because limb scans with auroral contamination or excess noise were not included in the inversion. Figure 3-6 clearly shows the northern and southern anomaly crests. The 2-D inversion algorithm removes the distortion caused by the geometry of the limb scans. The northern anomaly is stronger

and slightly lower in altitude than the southern crest. The variances in the parameters are determined from the diagonal terms of the covariance matrix. The uncertainties in *NmF2* were adjusted to take into account systematic errors arising from inaccuracies in the 135.6 nm radiative recombination rate (5% [*Meléndez-Alvira et al.*, 1999]) and in the intensity calibration scalar (10% [*Dymond et al.*, 2001]). The uncertainties in *hmF2* were adjusted to include the altitude uncertainty due to the ARGOS pointing uncertainty of ~5 km at the limb [*Dymond et al.*, 2001]. In the anomaly region, 1σ uncertainties in *NmF2* are on the order of 1.0×10^5 electrons/cm^3, 1σ uncertainties in *hmF2* are ~10 km, and 1σ uncertainties in the O scale height are ~13 km. In the northern mid-latitudes, however, the signal to noise ratio is much lower, leading to significantly larger uncertainties in the retrieved model parameters. *Dymond and Thomas* [2001] also found that a low signal to noise ratio resulted in poor estimates of the *hmF2* and O scale height.
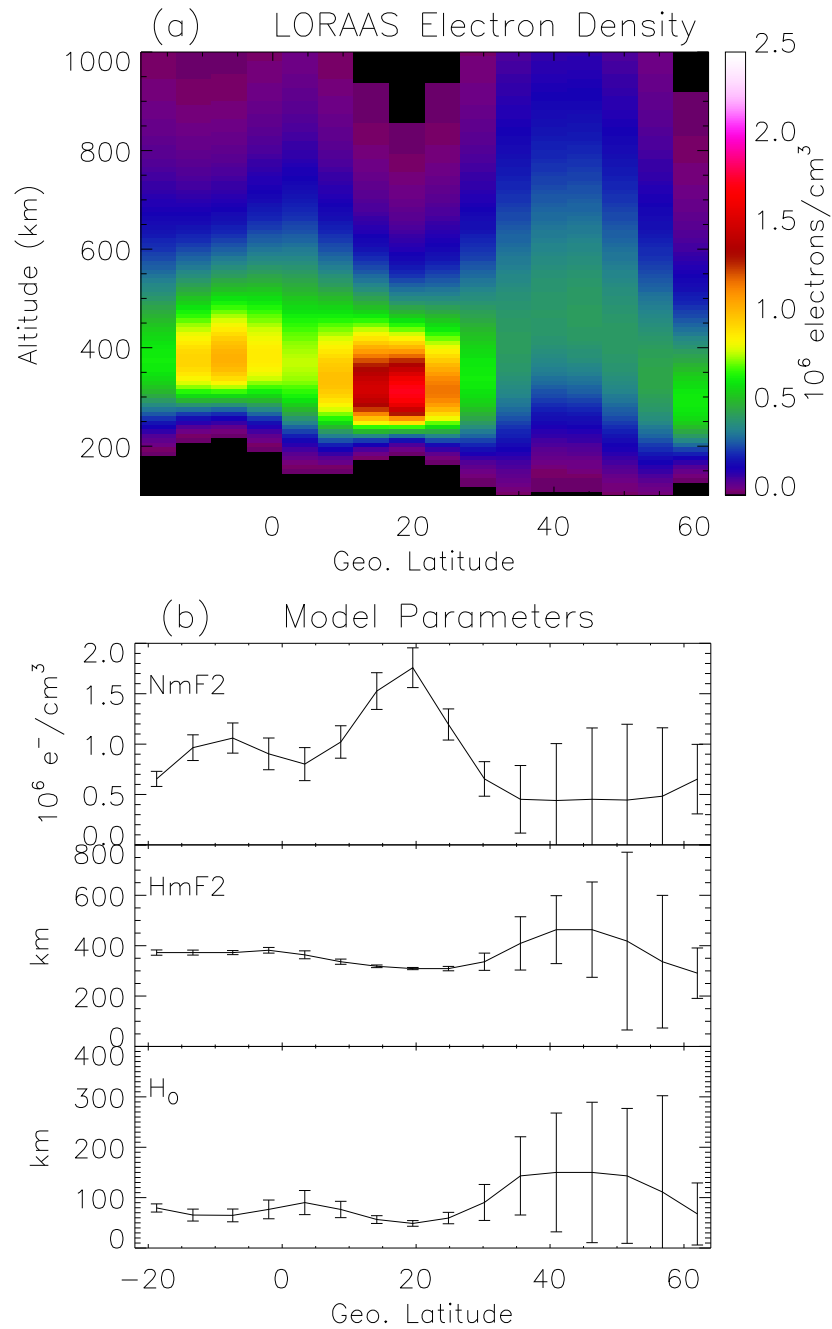
Figure 3-6 Model parameters and associated 1σ error bars obtained from the inversion of the limb scan 135.6 nm intensities for 9 March 2002 at 121° geographic longitude (0230 LT). The small signal to noise ratio in the northern midlatitudes leads to larger uncertainties in the model parameters in this region; uncertainties in the equatorial anomaly region are relatively smaller.

81

We used simulated data generated with SAMI2 to show how well the 2-D inversion technique can reproduce an ionosphere. Details of the methodology can be found in *Dymond and Thomas* [2001], where the 2-D algorithm was tested with simulated data using IRI-90. Figure 3-7(a) shows the model ionosphere generated by SAMI2. The SAMI2 ionosphere was integrated using the LORAAS viewing geometry to obtain line of sight intensities. These intensities were then used as input to the 2-D inversion algorithm to reconstruct the densities shown in Figure 3-7(b). The comparisons of the modeled and reconstructed *NmF2* and *hmF2* are shown in Figure 3-8. The regularization weight was varied to produce the best match to the model. The 2-D inversion algorithm accurately captures the latitudes of the anomaly crests. The peak heights agree with the model to within 20 km, with the largest discrepancies in the anomaly crests. The *NmF2*s are in fairly good agreement with the model, but cannot reproduce the peak densities of the anomaly crests. We suspect further improvements could be made to the 2-D inversion algorithm by varying the model grid size within the algorithm so that narrow features, such as the anomaly crests, can be captured more accurately.
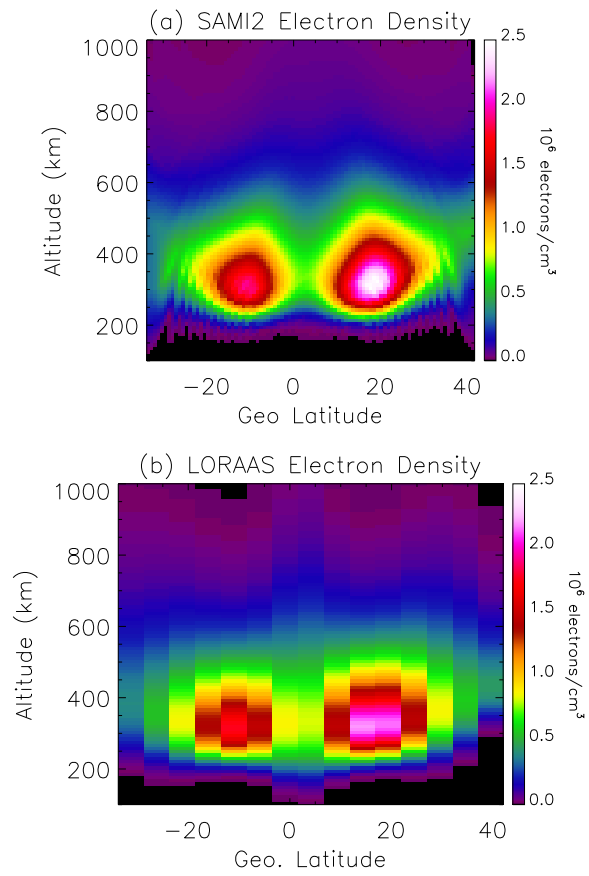
Figure 3-7 Example of a 2-D inversion with simulated data. (a) shows SAMI2 electron densities at 0230 LT and (b) shows electron densities that have been reconstructed from intensities obtained by integrating the SAMI2 ionosphere.
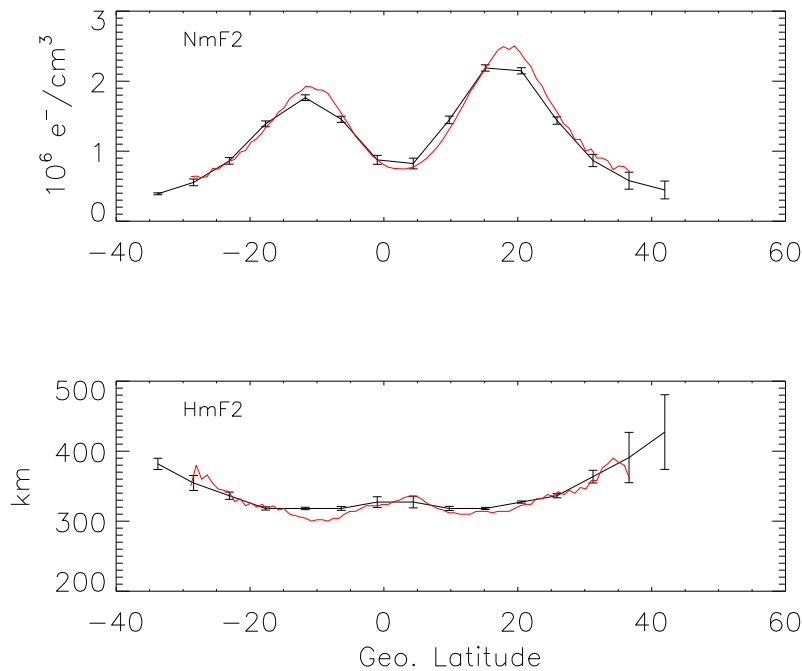
Figure 3-8 A comparison of *hmF2* and *NmF2* extracted from the SAMI2 model ionosphere with those determined from the 2-D reconstruction of the model ionosphere.

3.3 Comparison of LORAAS Electron Densities to Ionosonde Measurements

LORAAS electron densities retrieved by inversion of single limb scans of the 91.1 nm emission feature have been successfully compared to ionosonde observations of peak density, *NmF2*, and peak height, *hmF2*, [*Dymond et al.*, 2001]. In this study fifteen dayside limb scan retrievals were compared with data from seven ionosondes located in the northern midlatitude region. It was found that the fractional average difference in *NmF2* was 0.05% and that the average difference in *hmF2* was 5.4 km. In a more extensive study that used the densities retrieved from 135.6 nm emission feature using the two-dimensional inversion algorithm, *Coker et al.* [2004] compared total electron content

(*TEC*) obtained by vertically integrating the LORAAS derived densities to *TEC*

measurements provided by TOPEX/Poseidon for several days in December 1999 and

November 2000. The study determined that there is good agreement between the

LORAAS and TOPEX *TEC*s, especially when the measurements were spatially and

temporally coincident. It was found that the LORAAS vertical *TEC* is accurate to within

5 TECU (5×10^{12} electrons/cm^2). *Coker et al*. [2004] also found that the location and

latitudinal extent of the anomaly crests are properly identified in the LORAAS

inversions, though the retrieval algorithm was limited in its ability to capture narrow

latitudinal structures. It was suggested that this limitation may be due to overly

smoothing of the retrieved densities by regularization.

We use data available from the Space Physics Interactive Data Resource (SPIDR)

World Wide Web site (http://spidr.ngdc.noaa.gov/) to compare the peak densities of the

*F*2 region of the ionosphere derived from ionosondes to that of LORAAS. Ionosondes are

in operation across the globe, but very few operate in the equatorial regions; and even

fewer provide measurement data on SPIDR. For this reason, our study is limited to the

ionosonde operating in Darwin, Australia located at -12.5° latitude and 131.0° E

longitude, which is near the southern anomaly crest. Initially, another ionosonde

operating in China was also chosen for this study, but the data quality was questionable.

Only results for March 2002 are presented since no coincident measurements over

Darwin are available for March 2001.

Ionosondes sweep from lower to higher frequencies and record the return signals reflected from the different layers of the ionosphere. A unique relationship exists between the sounding frequencies and ionization densities that can reflect the high frequency radio pulses generated by the ionosonde. The *foF*2 is the *F*2 peak plasma frequency and is related to the *NmF2* by Equation (1-27).

Figure 3-9 shows the comparison of the Darwin *NmF2*s to LORAAS for March 2002. In both plots, the Darwin measurements between 0200 – 0300 LT are shown for each day of the month. LORAAS measurements that are within a specified latitude and longitude region of the Darwin site are over plotted. The figure to the left shows the LORAAS measurements that are within 3° latitude and 3° longitude of the Darwin site. The figure to the right shows LORAAS measurements in a larger longitude region (within 15° longitude). The LORAAS measurements match the Darwin results fairly well within a very narrow region. Once that region is expanded, longitudinal variability in the peak densities becomes evident, and the LORAAS data no longer match the Darwin results as closely.
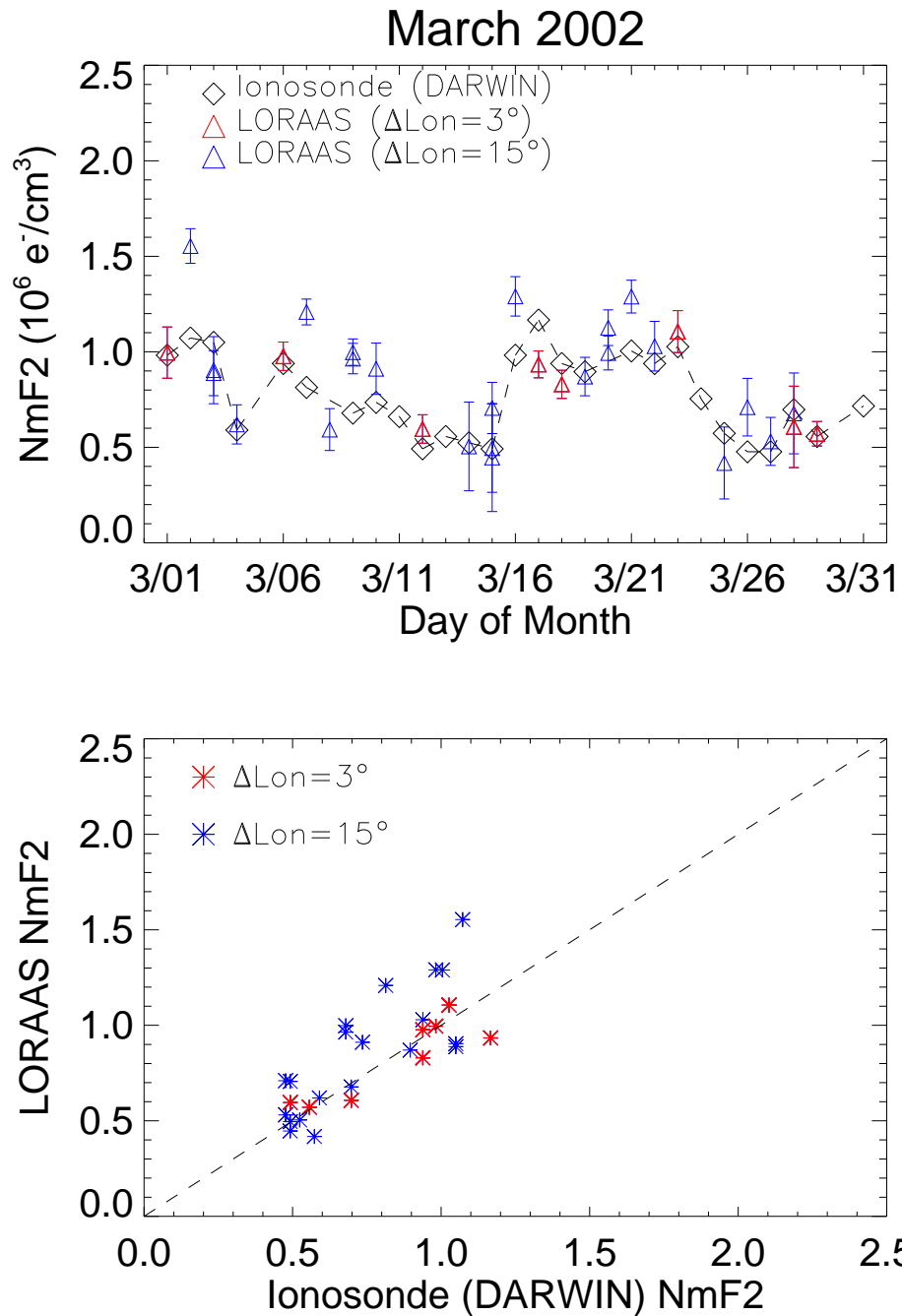
Figure 3-9 Comparison of LORAAS *NmF2*s to the Darwin ionosonde *NmF2*s for March 2002. Red triangles (stars) represent coincident measurements that are within 3° longitude of the ionosonde location. Blue triangles (stars) represent coincident measurements within 15° longitude of the ionosonde.

3.4 Comparison of LORAAS and GUVI Data

The Global Ultraviolet Imager (GUVI) was launched aboard the NASA TIMED (Thermosphere Ionosphere Mesosphere Energy and Dynamics) satellite in 2001. TIMED was launched into a 630 km 97.8 min period, circular polar orbit with a 74.1° inclination. The satellite progresses through all local times in about 60 days. GUVI measures the spectral radiance of the Earth's far ultraviolet airglow in the spectral region from 120 to 180 nm using a cross-track scanning spectrometer design [*Christensen et al*., 2003]. The radiance is measured in five bandpass channels. Major emission features within those channels include H (121.6), O I (130.4) O I (135.6), and the N_2 LBH bands (141.0 – 152.8 nm and 167.2 – 181.2 nm passbands respectively).

Figure 3-10 shows the scan geometry of GUVI observations. The scan begins on the antisunward limb at a tangent altitude of ~525 km and moves downward toward the Earth's surface, or disk, and across the disk to the sunward side, covering a total of 140 degrees.
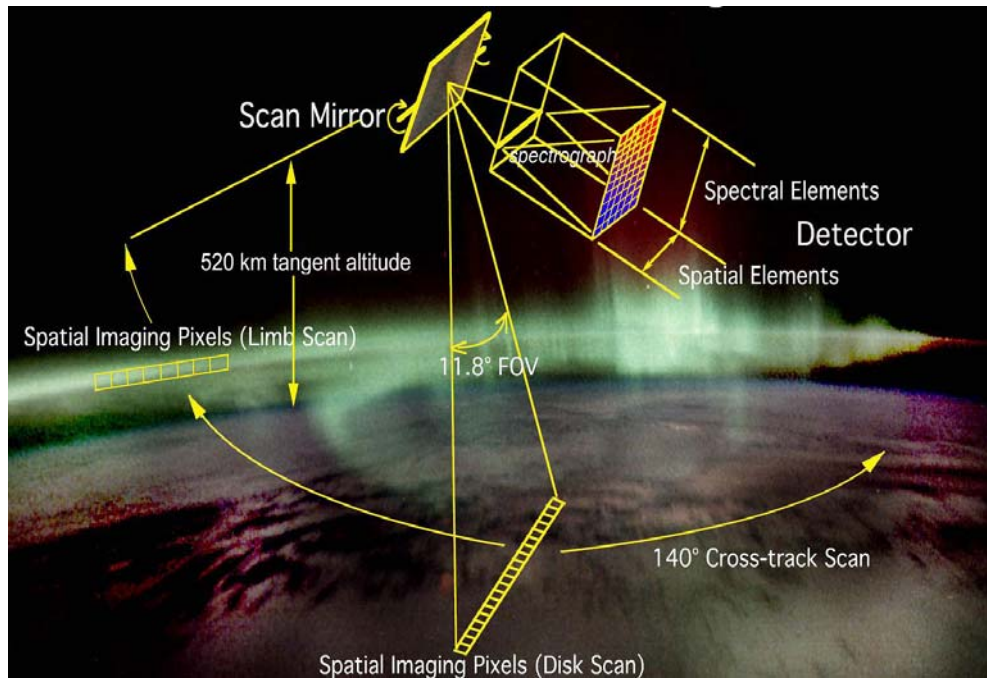
Figure 3-10 Illustration of the scan operation of the GUVI instrument. The slit dimension is projected along the ground track of the satellite. The cross track scan is initiated every 15 seconds [from *Christensen et al.*, 2003].

In this study, we are interested in obtaining electron densities from the GUVI limb scans in the O I (135.6 nm) channel by performing a 1-D inversion similar to the technique described in Section 3.2. The primary difference between the 1-D and 2-D techniques is that the 1-D algorithm inverts each limb scan separately. The algorithm is described in detail by *Dymond et al*. [2001].

The first 32 steps of a GUVI scan are on the limb, covering tangent point altitudes from 525 km down to 110 km. Though there are 14 pixels in the O I channel, we use only four of the central pixels. The outer pixels are ignored because a distortion has been identified in the slit which leads to unresolved uncertainties in the tangent point altitudes

of these pixels [*private communication with R. R. Meier*, 2007]. To avoid errors introduced by this distortion, we average pixels 6 through 9 and assign the tangent point position of pixel 8 to this average. Because the signal levels are very low in the nighttime observations, we also average together 5 consecutive limb scans. This greatly reduces the spatial resolution of the retrieval to about 4° in latitude but it is similar to the LORAAS resolution of ~5°.

As we did for the LORAAS data, we assume the 135.6 nm feature at night is optically thin and we neglect emissions from $O^+ - O^-$ neutralization. The three parameter Chapman function for describing the O^+ density is given by equation (3-2) above and the radiance is given by equation (3-1). Again, we assume the temperature is isothermal at 1050° K.

On February 28, 2002, ARGOS and TIMED were in orbits where the limb scans were nearly coincident in space and time. Figure 3-11 shows the GUVI (blue) and LORAAS (red) tangent point positions of the limb scans. The times of the geographic equator crossing of GUVI and LORAAS are also shown. The TIMED satellite moves from south to north, while the ARGOS satellite is moving in the opposite direction. In the rightmost scan, the satellites cross the equator within 21 minutes of each other. By the leftmost scan, the satellites are 42 minutes apart.
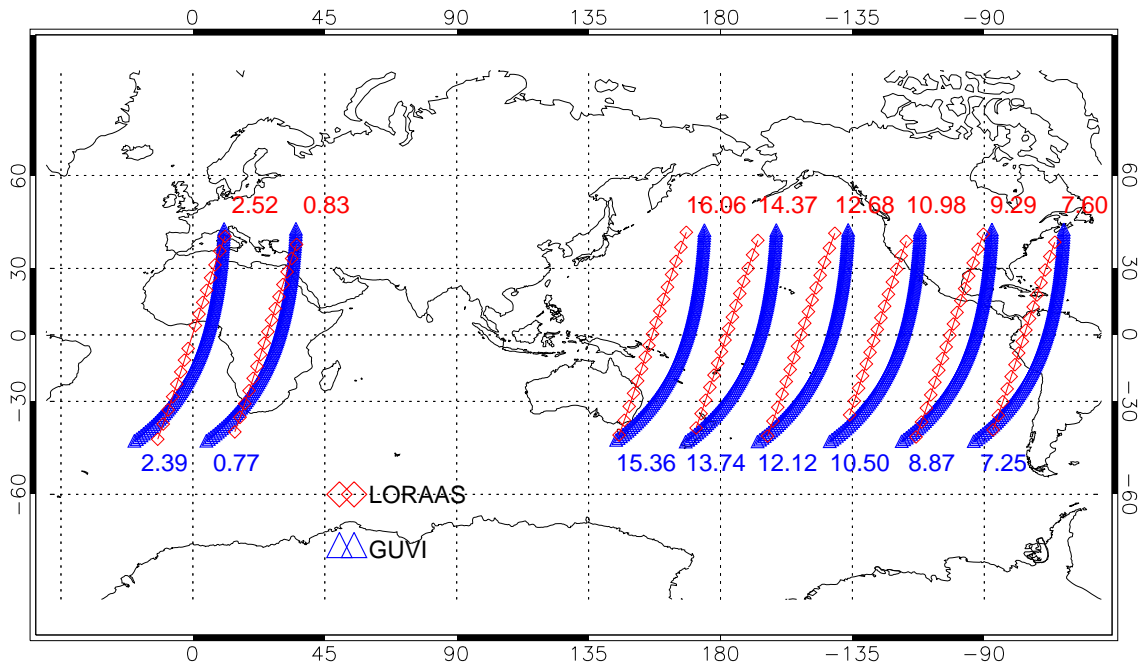
Figure 3-11 GUVI (blue) and LORAAS (red) tangent point latitude and longitudes of limb scans obtained on February 28, 2002. On this day, the TIMED satellite travels from south to north and ARGOS travels from north to south. The UTs of the equator crossing are labeled. Only the passes used in the comparison study are shown.

Figure 3-12 shows an example of the LORAAS and GUVI limb radiances at 12.68 UT and 12.12 UT, respectively. Here, in order to highlight the differences between the two instruments, the GUVI limb scans have not been averaged. LORAAS covers a greater altitude range, but has much lower latitude resolution than GUVI. In both images, the northern and southern anomaly features are clearly evident, located at roughly ±15° latitude with the southern crest at a higher altitude than the northern crest. Due to the differing geometries of the limb scans (LORAAS limb scans are in-track and GUVI limb scans are cross-track), a more detailed comparison cannot be performed without first performing the inversions.

91
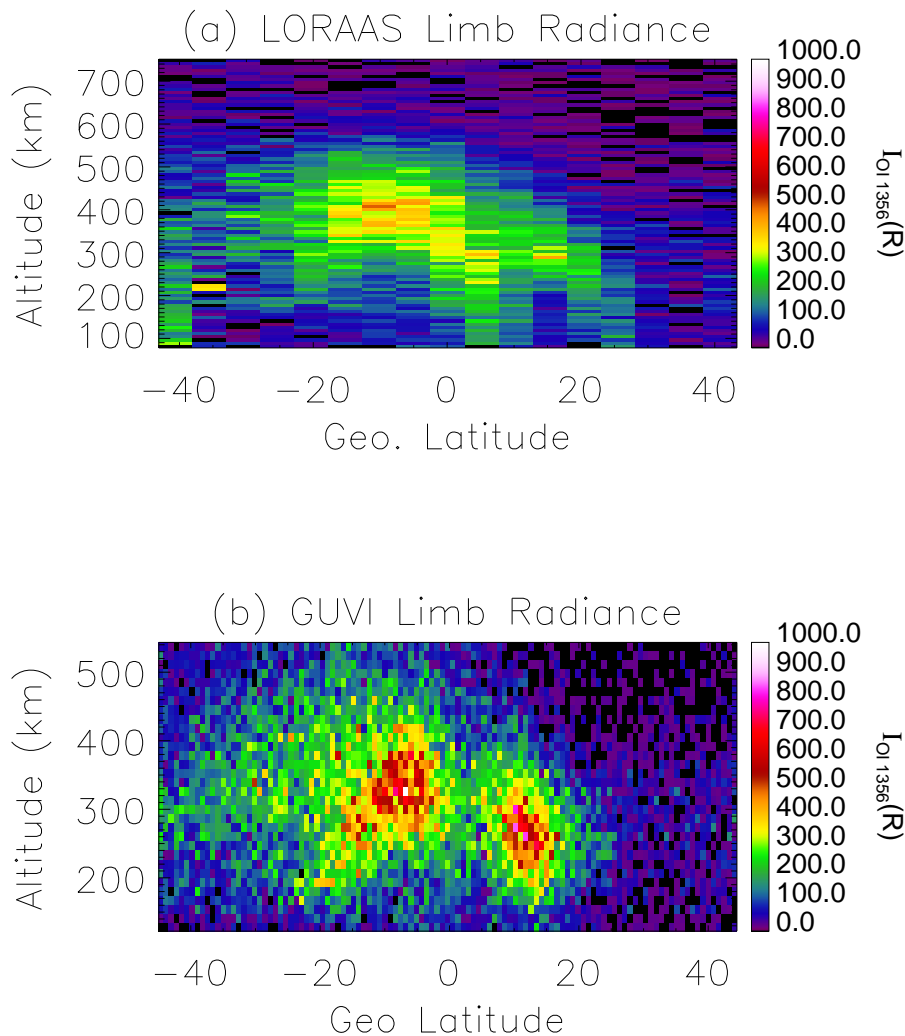
Figure 3-12 (a) LORAAS limb radiances (Lon = 208°, UT=12.68) and (b) GUVI limb radiances (Lon = 218° and UT=12.12).

Figure 3-13 through Figure 3-18 show the comparisons of the electron density profiles, peak electron densities (*NmF2*) and peak heights (*hmF2*) retrieved from the inversions of the GUVI and LORAAS limb scans. We also compare our results to the electron density profiles available on the GUVI website. The "online" densities are

derived using a two-step inversion technique where the volume emission rate as a function of altitude is determined from the 135.6 nm radiance measurements and then the inferred volume emission rates are used to determine the electron density profiles. The technique is discussed in detail by *DeMajistre et al*. [2004].

Figure 3-13 shows the southern anomaly crest at -30° geographic latitude, which corresponds to -17° dip latitude. Both the online GUVI electron densities and that derived from the 1-D inversion technique show a very high *NmF2* (2.6×10^6 cm^{-3}) in the anomaly crest, while the LORAAS density (1.1×10^6 cm^{-3}) is much lower in this region. As we will show in subsequent comparisons, this is not a typical difference and there may be several possible explanations. There is a temporal offset of nearly 40 minutes and a spatial offset of 5° longitude between the GUVI and LORAAS observations; however, model runs performed with IRI-90 show that the electron density is 1.5×10^6 cm^{-3} at the time and location of the GUVI observation and drops off to 1.3×10^6 cm^{-3} at the LORAAS observation. The model results suggest that the LORAAS densities are more typical, but without additional measurements we cannot rule out the possibility of a localized enhancement. As discussed in the previous section, the 2-D inversion typically smoothes out the peak densities in the anomaly crests, resulting in a lower than expected *NmF2*, but this is unlikely to account for a nearly 60% difference between the GUVI and LORAAS densities. *DeMajistre et al*. [2004] compared GUVI electron density profiles with incoherent scatter radar (ISR) measurements at Millstone Hill and in general found good agreement between the two, except after midnight when the GUVI densities were significantly higher than the ISR densities. It was concluded that conjugate

photoelectrons produced in the sunlit southern hemisphere excite the atomic oxygen through photoelectron impact, thus providing a significant source of contamination in the GUVI field-of-view. Since our GUVI observations occur at a time when the southern magnetic pole is in sunlight, conjugate photoelectron contamination is a possible explanation of the observed enhancement, though a detailed investigation of the geometry should be conducted to verify this. LORAAS performs limb scans in the plane of the satellite orbit, looking across considerably fewer magnetic field lines than GUVI; therefore, contamination due to conjugate photoelectrons is not a significant issue for the LORAAS data. The peak heights of the *F* region ionosphere compare fairly well between the GUVI and LORAAS measurements.

The remaining coincident passes show that the position, both in latitude and altitude, agree fairly well between LORAAS and GUVI. Again, the LORAAS densities are typically lower than GUVI in the anomaly crests. In Figure 3-14 the difference in electron density may be attributed to the LORAAS observation taking place 40 minutes later than the GUVI observation as well as to overly smoothing of the LORAAS densities. Modeling studies using SAMI2 indicate that the anomaly crest density can decrease by $\sim 3.0 \times 10^5$ cm^{-3} within this timeframe. In Figure 3-17, the online electron density profiles suggest a very narrow peak in density near 400 km altitude, but the LORAAS intensities do not show such a region. Also, the GUVI results show a well defined trough region between the anomaly crests that is not captured in the LORAAS data; this may be due to the different geometries of the observations.

94

The comparison of the GUVI and LORAAS $NmF2$s and $hmF2$s are summarized in Figure 3-19. These plots show the LORAAS densities are larger than the GUVI densities for $NmF2$s less than 1.0×10^6 cm^{-3}, but the GUVI densities are larger for higher $NmF2$s. The mean absolute difference in $NmF2$, excluding the outlier observed in Figure 3-13, is 2.1×10^5 cm^{-3}, which is 18% of the average LORAAS $NmF2$. The peak heights are in closer agreement, with a mean difference of 16.3 km, which is less than 5% of the average LORAAS $hmF2$. We did not find a strong correlation of the mean difference in either parameter with increasing longitude or local time. This is not an indication that temporal or spatial differences in the measurements do not play a role, but that they are not the main cause of all the observed differences. We did, however, find some correlation with dip latitude. For dip latitudes less than 10° from the equator, the mean LORAAS $NmF2$ was higher; for dip latitudes greater than 10° from the equator (the anomaly crest region) the mean GUVI $NmF2$s were higher. For $hmF2$, the greatest differences were found in the anomaly crest regions, but neither the GUVI nor LORAAS measurements were systematically higher or lower than the other.
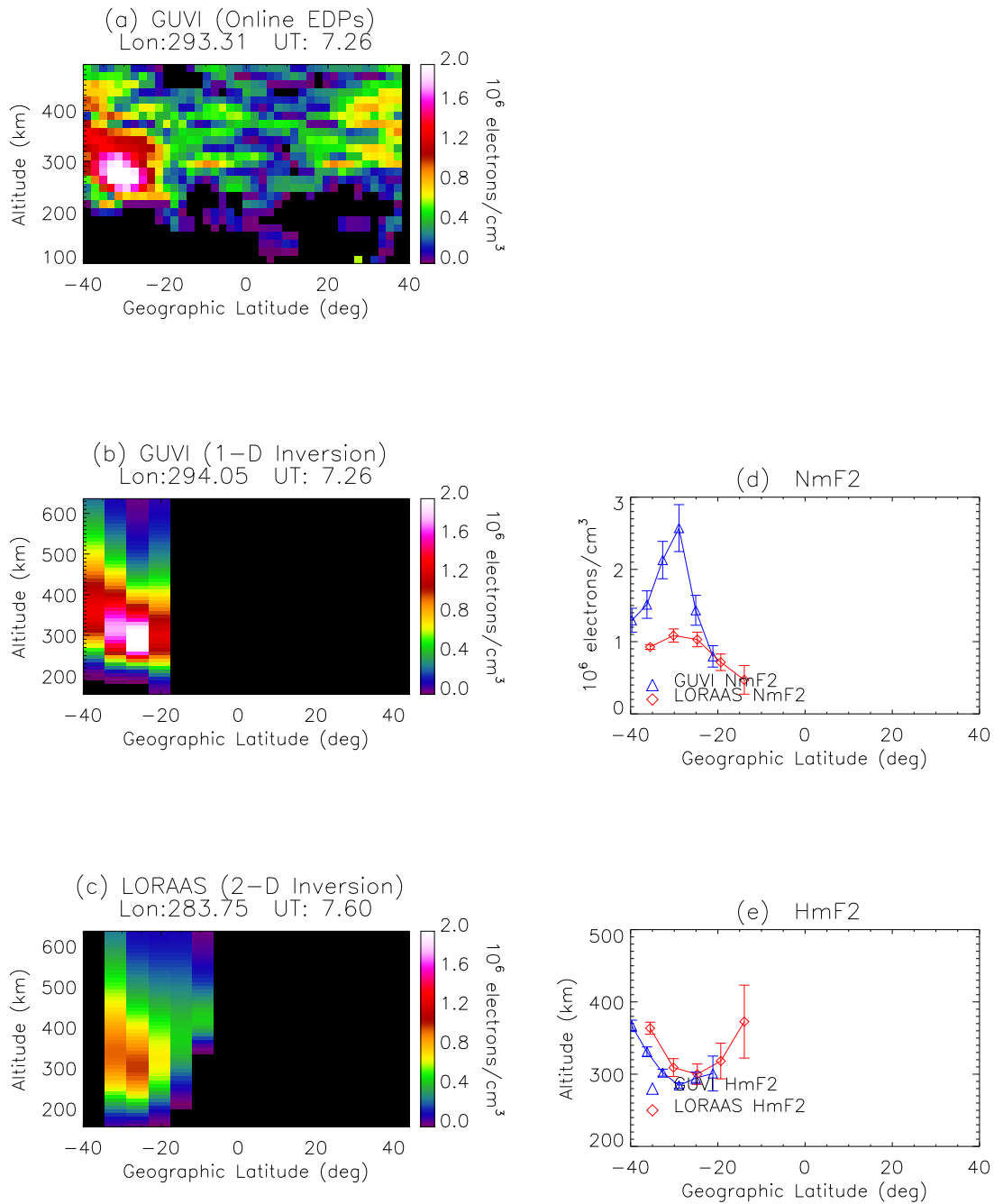
Figure 3-13 (a) GUVI densities (level 3 products available on the GUVI website), (b) derived GUVI densities using the 1-D inversion algorithm, (c) derived LORAAS densities using the 2-D inversion algorithm, (d) a comparison of the GUVI and LORAAS peak densities (*NmF2*), (e) a comparison of the GUVI and LORAAS peak electron density heights (*hmF2*).
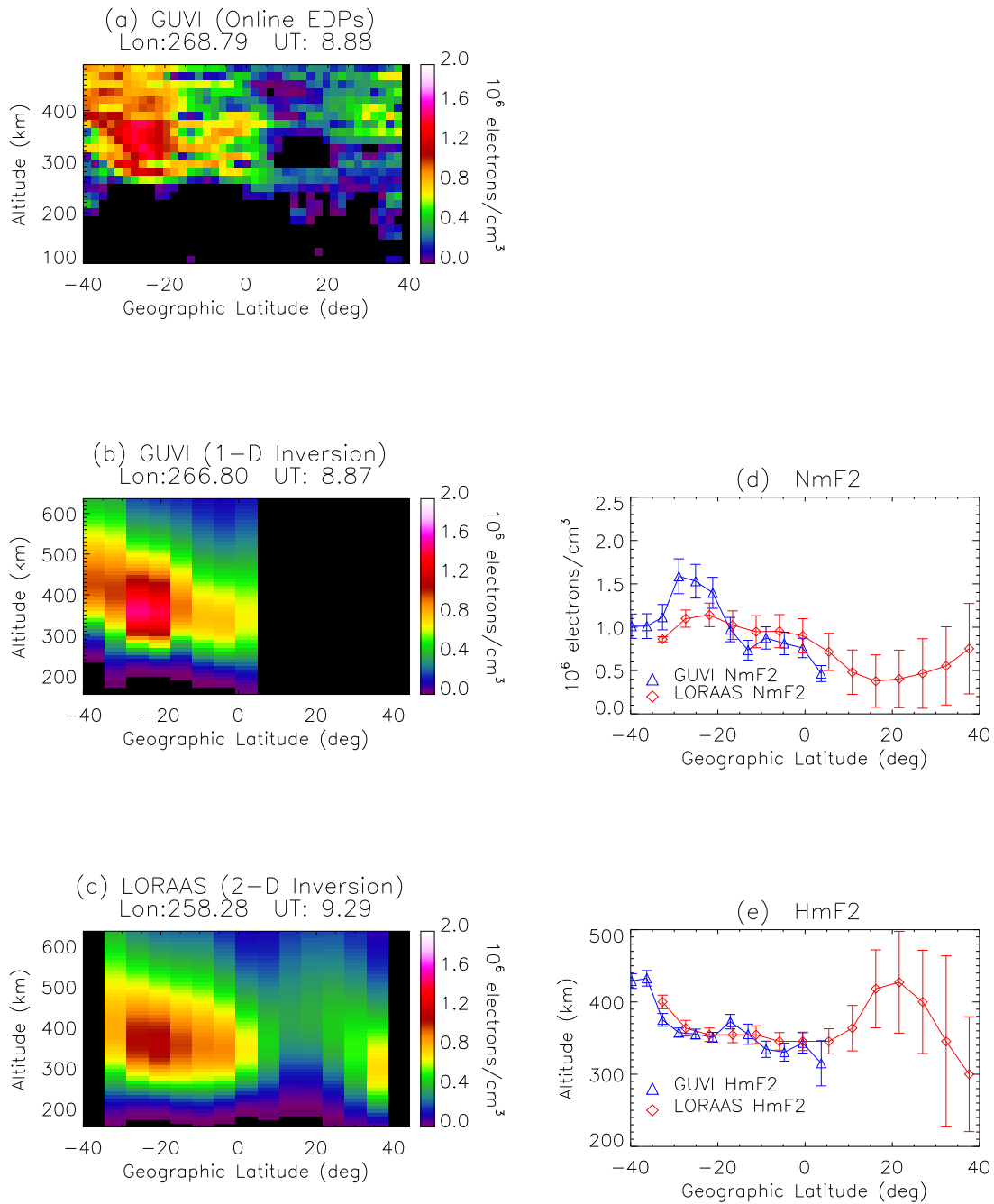
Figure 3-14 (a) GUVI densities (level 3 products available on the GUVI website), (b) derived GUVI densities using the 1-D inversion algorithm, (c) derived LORAAS densities using the 2-D inversion algorithm, (d) a comparison of the GUVI and LORAAS peak densities (*NmF2*), (e) a comparison of the GUVI and LORAAS peak electron density heights (*hmF2*).
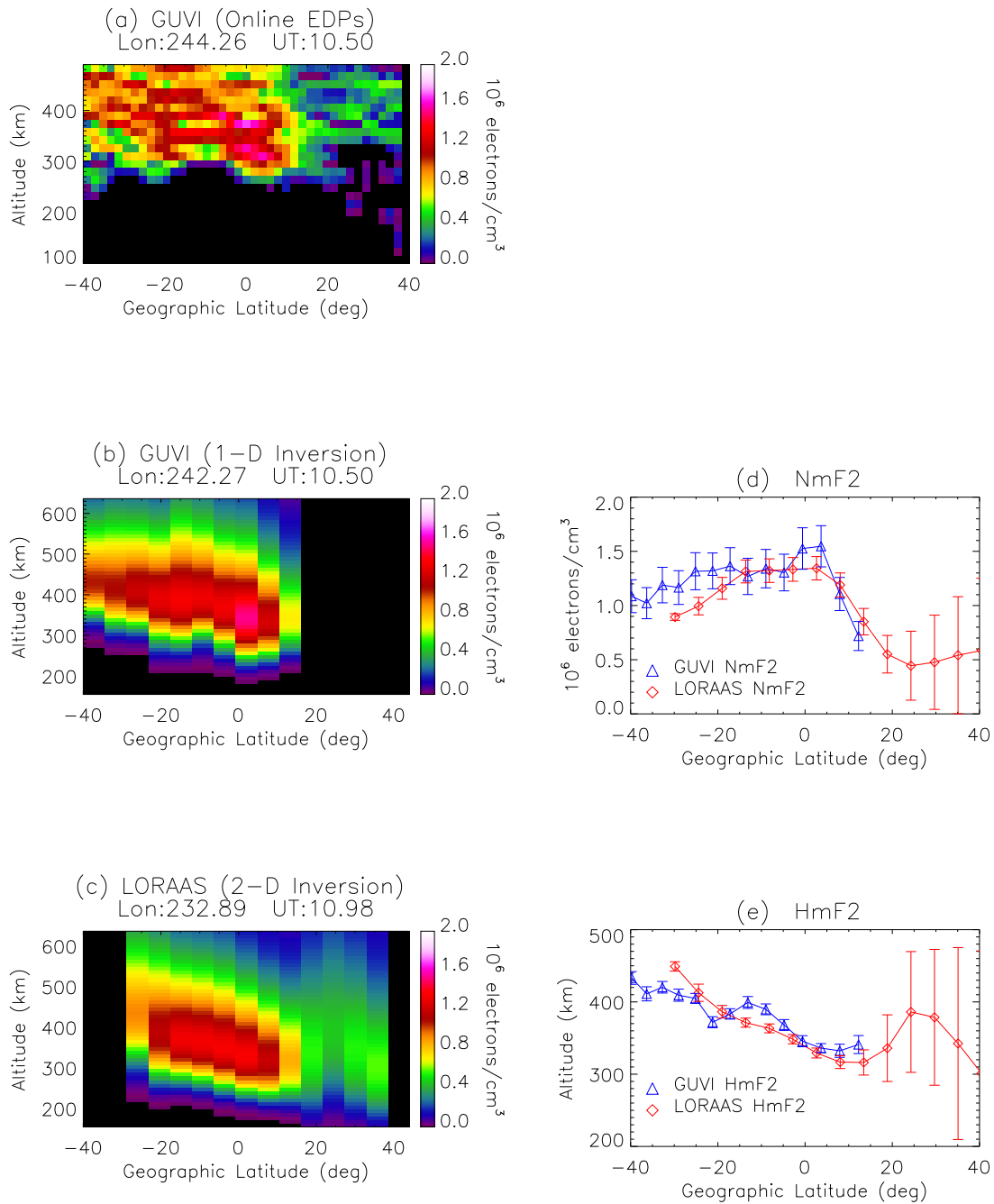
Figure 3-15 (a) GUVI densities (level 3 products available on the GUVI website), (b) derived GUVI densities using the 1-D inversion algorithm, (c) derived LORAAS densities using the 2-D inversion algorithm, (d) a comparison of the GUVI and LORAAS peak densities (*NmF2*), (e) a comparison of the GUVI and LORAAS peak electron density heights (*hmF2*).
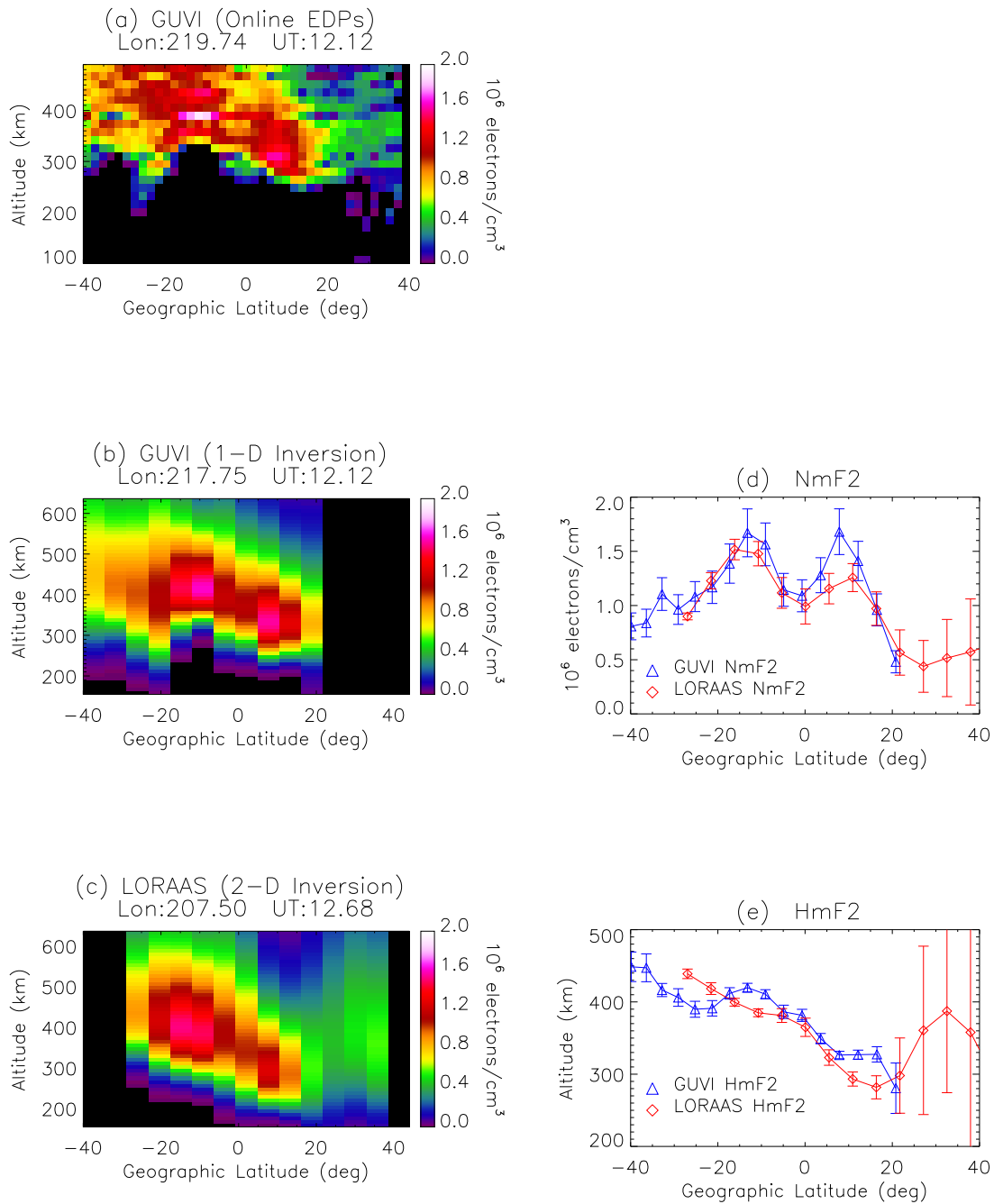
Figure 3-16 (a) GUVI densities (level 3 products available on the GUVI website), (b) derived GUVI densities using the 1-D inversion algorithm, (c) derived LORAAS densities using the 2-D inversion algorithm, (d) a comparison of the GUVI and LORAAS peak densities (*NmF2*), (e) a comparison of the GUVI and LORAAS peak electron density heights (*hmF2*).
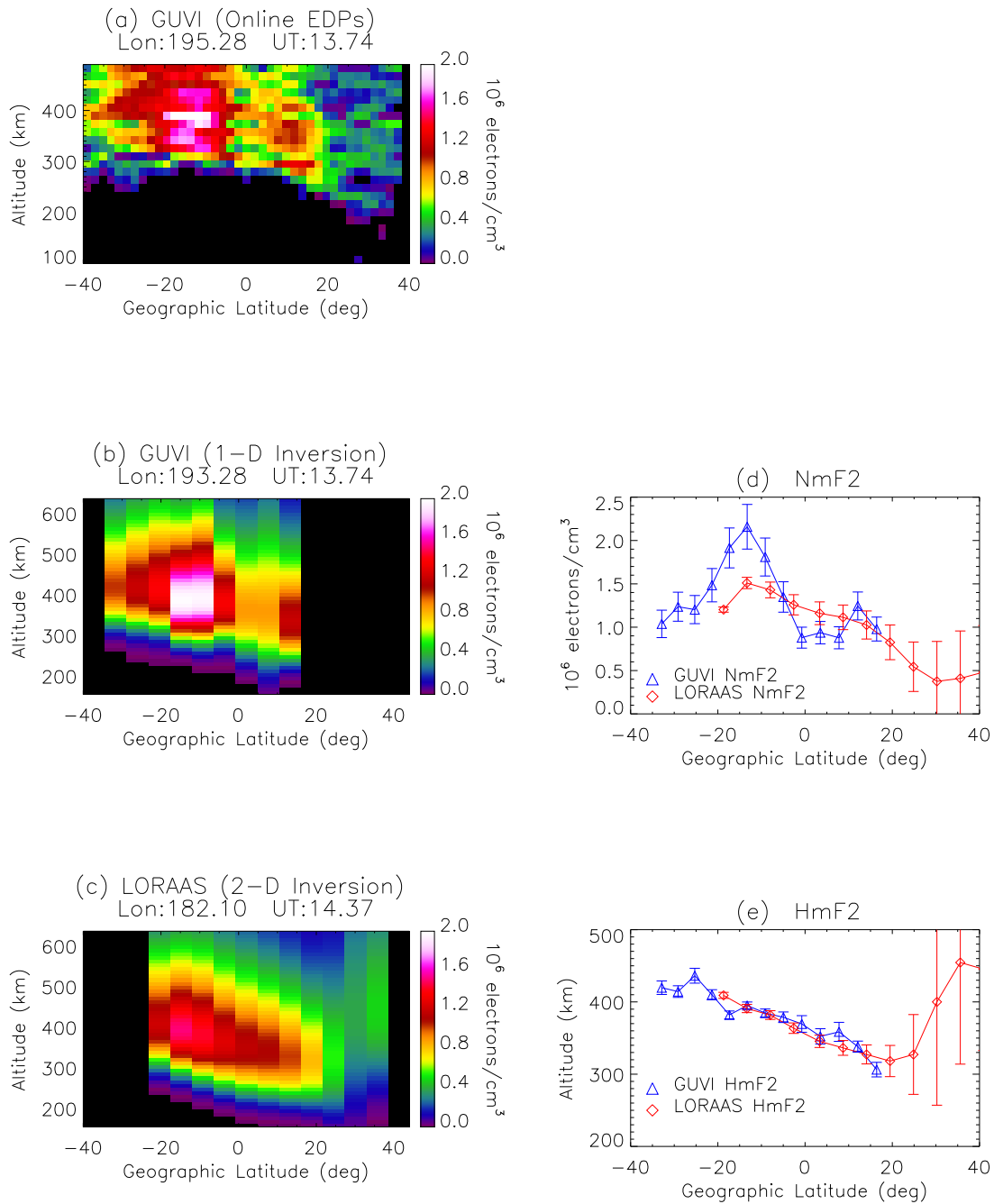
Figure 3-17 (a) GUVI densities (level 3 products available on the GUVI website), (b) derived GUVI densities using the 1-D inversion algorithm, (c) derived LORAAS densities using the 2-D inversion algorithm, (d) a comparison of the GUVI and LORAAS peak densities (*NmF2*), (e) a comparison of the GUVI and LORAAS peak electron density heights (*hmF2*).
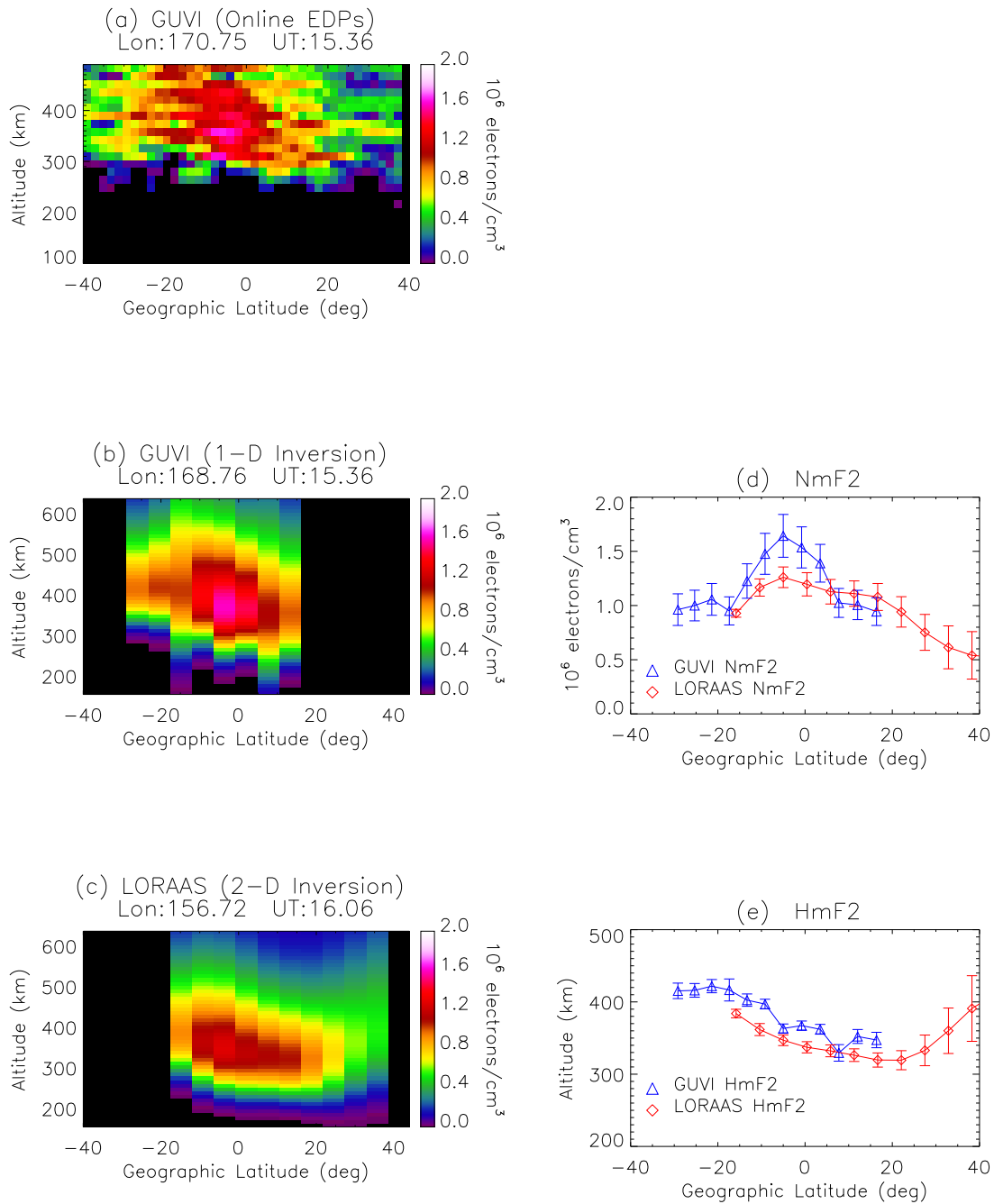
Figure 3-18 (a) GUVI densities (level 3 products available on the GUVI website), (b) derived GUVI densities using the 1-D inversion algorithm, (c) derived LORAAS densities using the 2-D inversion algorithm, (d) a comparison of the GUVI and LORAAS peak densities (*NmF2*), (e) a comparison of the GUVI and LORAAS peak electron density heights (*hmF2*).
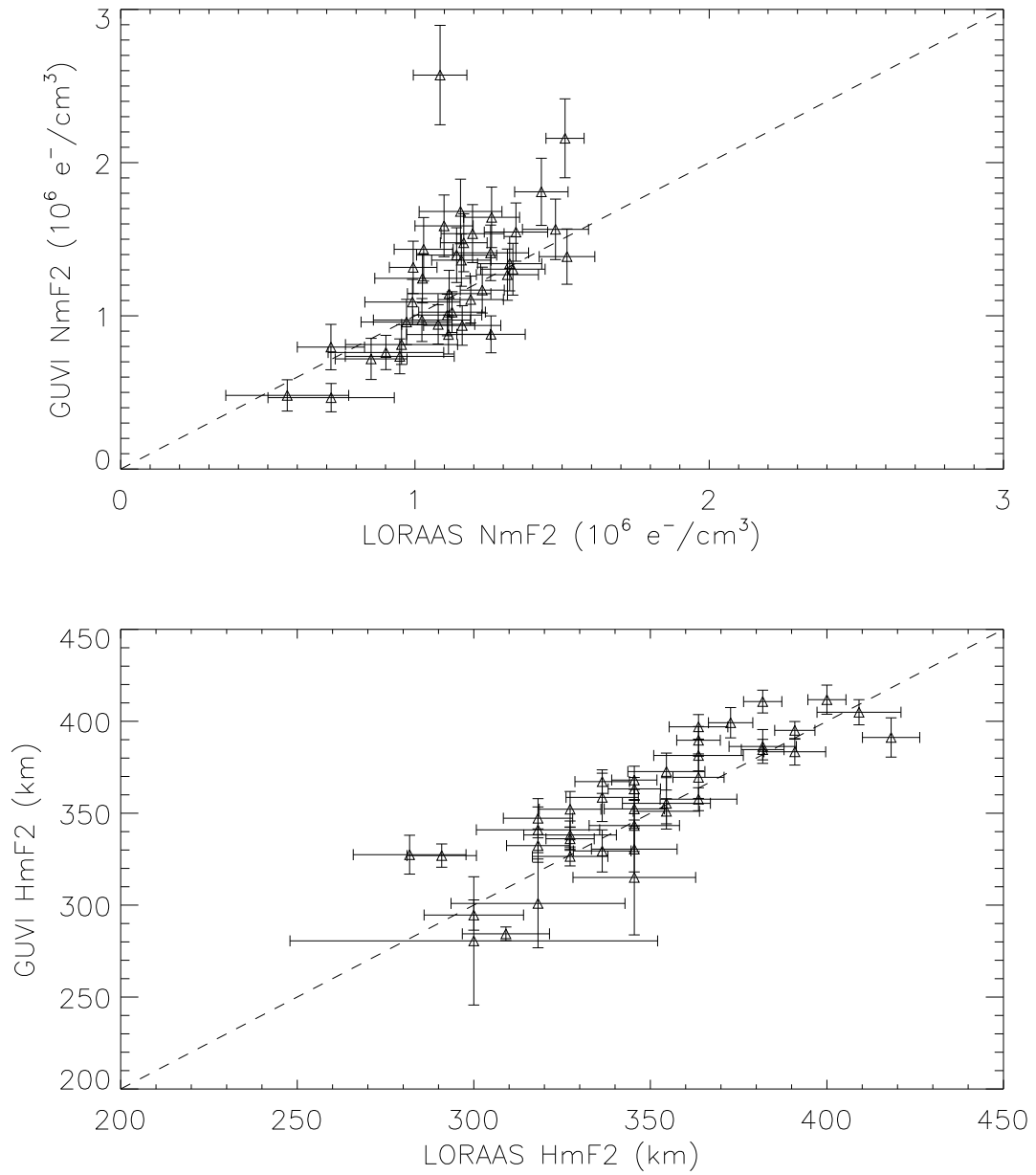
Figure 3-19 A comparison of the LORAAS and GUVI peak densities (*NmF2*) and peak heights (*hmF2*) for coincident measurements on February 28, 2002.

3.5 Day to Day Variability of the Equatorial Anomaly

We analyze the variability of the equatorial anomaly region for March 2001 and March 2002. March 2002 was chosen because it was a particularly quiet month, with only two days where the average daily Ap index > 30. The Ap is a 3 hourly index that measures geomagnetic activity and ranges from 0, indicating no activity, to 400, indicating a significant geomagnetic storm. The mean $F_{10.7}$ for this month is 178.4×10^{-22} W m^{-2} Hz^{-1}. March 2001 is much more active, especially toward the end of the month, but also has a number of quiet days. The mean $F_{10.7}$ is 176.1, though the mean $F_{10.7}$ for March 1-21 2001 is 147.4. The average Ap index is 20.2. Geomagnetic conditions for March 2001 and March 2002 are shown in Figure 3-20 and Figure 3-21.
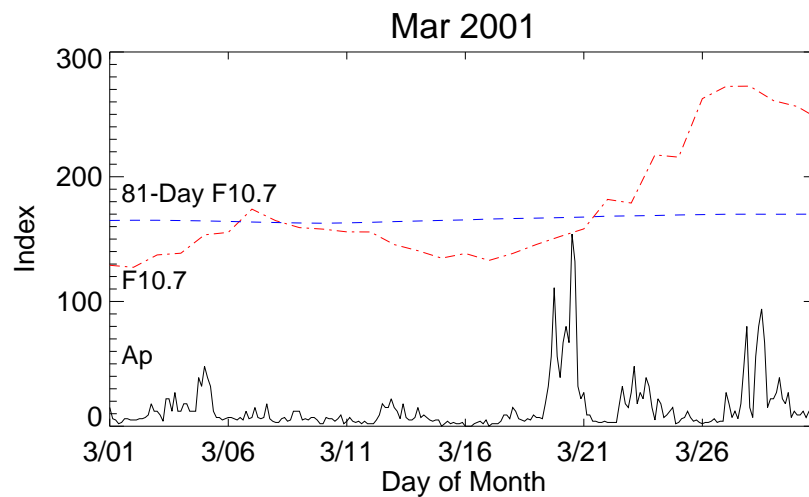
Figure 3-20 Geomagnetic indices, including 3-hour Ap, $F_{10.7}$ and the 81-Day average $F_{10.7}$ are shown for the month of March 2001.
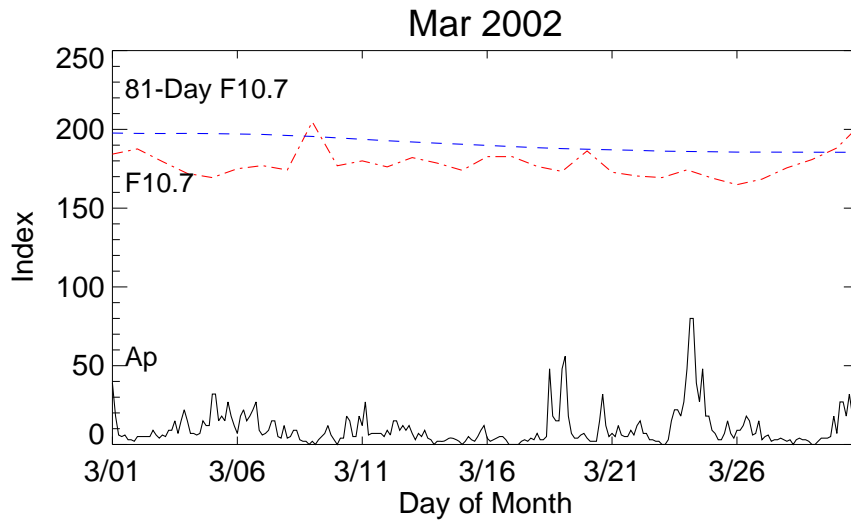
Figure 3-21 Geomagnetic indices, including 3-hour Ap, $F_{10.7}$ and the 81-Day average $F_{10.7}$ are shown for the month of March 2002.

We note that the LORAAS instrument was seriously affected by the South Atlantic Anomaly (SAA), shown in red in Figure 3-22. Limb scans collected while the satellite was in this region were degraded by noise and could not be processed. As a result, there is little information about the equatorial anomalies in the American and African sectors.
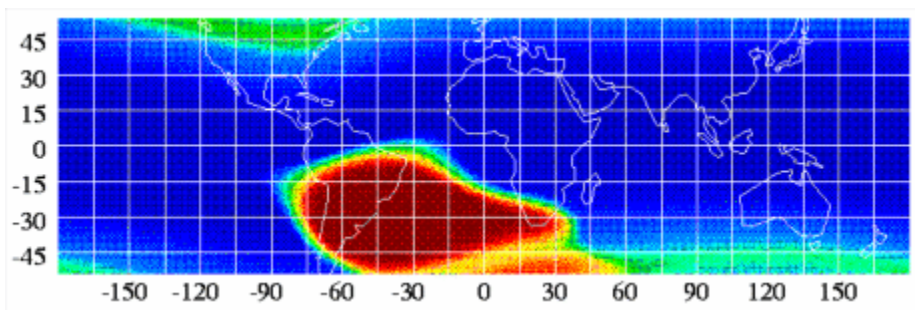
Figure 3-22 An image of the relative location of the SAA. The data were collected by the South Atlantic Anomaly Detector (SAAD) aboard the ROSAT spacecraft (**http://heasarc.gsfc.nasa.gov/docs/rosat/gallery/display/saa.html** image credited to Steve Snowden).

For our study of the day to day variability of the ionosphere, we processed the

LORAAS data for the months of March 2001 and March 2002. We use the inversion

techniques described in Section 3 to obtain altitude-latitude electron density maps (Figure

3-6c) for each nightside pass through the equatorial anomaly region. We then use a

simple algorithm, described below, to identify specific features of the anomaly crests:

peak density, peak height, latitude, and width. This information is used to obtain mean

values for the anomaly crests and the deviation from the mean.

The anomaly identification algorithm is based on the assumption that the

equatorial anomaly region is typically characterized by two crests, or density

enhancements, that form on either side of the magnetic dip equator. The dip equator is

defined as the location where the inclination, I, of Earth's magnetic field, **B**, is zero. The

location of the anomaly crests is determined by first finding the $NmF2$ of each electron

density profile in the density maps. To minimize misidentification of the anomaly crests,

the first and last electron density profiles of a pass are excluded on the basis that these

profiles are at the boundaries of the solution space and therefore heavily influenced by

the boundary conditions. Profiles at latitudes greater than or less than $\pm 40°$ dip latitude

are also excluded based on the assumption that under geomagnetically quiet conditions,

the anomaly crests do not extend to midlatitudes. This latitudinal limit prevents

midlatitude density enhancements from accidentally being identified as anomaly features.

The algorithm then searches for the maximum density on either side of the magnetic dip

equator, where the dip equator is determined using IGRF (the 9th generation model of the

International Geomagnetic Reference Field,

http://www.ngdc.noaa.gov/IAGA/vmod/igrf.html). The full width half-maximum

(FWHM) is calculated for each anomaly crest. Figure 3-23 shows an example *NmF2*

profile with the various anomaly features identified. Occasionally, only one anomaly

crest is detected within ± 3° of the dip equator. In this case, it is assumed that the northern

and southern anomalies are combined, or collapsed, into one feature with a separation of

0°. Such features can arise when the upward $\mathbf{E} \times \mathbf{B}$ drift is not strong enough to displace

the plasma away from the dip equator.
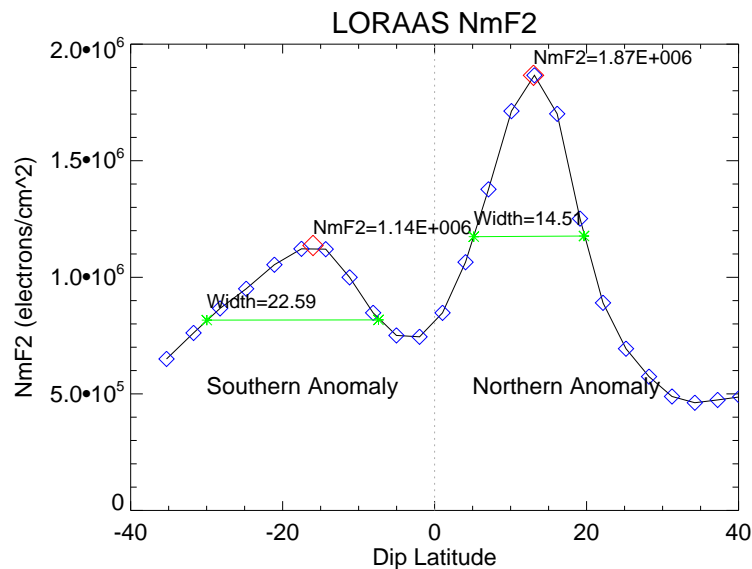
Figure 3-23 Example LORAAS *NmF2* latitudinal profile (March 9, 2002 at 121˚ latitude) showing the peak *NmF2*s and widths of the northern and southern anomaly crests.

To study the longitudinal variability, the Earth is divided into 15 longitude bins of

24°, listed in Table 3-3. These bins are chosen to roughly correspond to the 14 orbits

ARGOS accomplishes in a 24 hour period. The longitude of a LORAAS pass is determined by the longitude at which ARGOS crosses the geographic equator.

Table 3-3 LORAAS longitude bins and associated mean UT.

Longitude Sector (deg)	Geographic Longitudes (deg)	Mean UT (hr)	Longitude Sector (deg)	Geographic Longitudes (deg)	Mean UT (hr)
12	0-24	1.7	204	192-216	12.9
36	24-48	0.1	228	216-240	11.3
60	48-72	22.5	252	240-264	9.7
84	72-96	20.9	276	264-288	8.1
108	96-120	19.3	300	288-312	6.5
132	120-144	17.7	324	312-336	4.9
156	144-168	16.1	348	336-360	3.3
180	168-192	14.5	-	-	-

We plot observed variability in each longitude sector on each day in March 2001 and March 2002 (shown in Figure 3-24 through Figure 3-35). Only geomagnetically quiet days are plotted, where we define quiet days as those in which the 3 hour *Ap* index was less than 30 from 1600 LT the previous afternoon to the time of the observation. By using this definition we limit the possibility that geomagnetic activity influenced the strength of the evening upward plasma drifts and hence the density and location of the anomaly crests. There are a number of days with missing data, which indicates one of the following: 1) there are insufficient data to determine if an anomaly is present, 2) the anomaly is not present or is below the detection threshold of 6.0×10^5 cm^{-3}, or 3) it is a geomagnetically active day.

Figure 3-24 and Figure 3-25 show the mean crest latitude for each longitude

sector. The latitude of the anomaly crests provides some indication of the strength of the

daytime and prereversal enhancement of the upward $\mathbf{E} \times \mathbf{B}$ drifts. Large upward plasma

drifts push the anomaly to higher latitudes. Generally, the crests are symmetric about the

dip equator, but asymmetries do arise from the effects of neutral winds. We find that the

anomaly crest location in each longitude bin is nearly symmetric about the dip equator to

within ~5°, the latitudinal resolution of the LORAAS inversions. But in both years the

southern anomaly crests are occasionally shifted southward of their expected locations.

For example, in the 156° longitude sector on March 17, 2002 (Figure 3-25), the northern

crest is located at 15° dip latitude while the southern crest is at -35°. We have performed

modeling studies with SAMI2 that indicate this may be due to a strong equatorward wind

in the southern hemisphere that acts to maintain the midlatitude F region iononization

well past midnight. Certainly, this is an area that warrants further investigation.

Figure 3-26 and Figure 3-27 show the separation of the northern and southern

anomaly crests for those days in which both crests are identified. These figures clearly

show several instances where the anomaly crests have collapsed, or come together, at the

dip equator. For example, Figure 3-27 shows this occurred in 2002 on March 5, 7, 8, 25

and 26 in the 84° longitude sector, more than in any other longitude sector. This result is

consistent with recent studies using GUVI disk data at dusk that show a collapse of the

anomaly occurs frequently in the Indian-African longitude sector [*Basu et al.*, 2006]. Our

results also show that there is a relatively high occurrence of collapse in the eastern

Pacific region. It would be interesting to determine if the collapses observed in the post-

midnight sector by LORAAS are correlated with the dusk collapses. Modeling studies should be conducted to determine the relative roles of the $\mathbf{E} \times \mathbf{B}$ drifts and the neutral winds.

Figure 3-28 and Figure 3-29 show the daily variation of the *NmF2* of the northern crest, while Figure 3-30 and Figure 3-31 show the variation of the southern crest *NmF2*s. The peak densities in the anomaly crests are primarily determined by a combination of $\mathbf{E} \times \mathbf{B}$ drifts, both upward and downward, and neutral winds, as discussed in Section 1.5. In the postmidnight sector, large densities typically indicate strong equatorward winds that maintain the ionosphere at altitudes where recombination is slow. In the LORAAS data, large density variations on the order of 1.0×10^6 cm^{-3} from one day to the next are not uncommon in all longitude sectors. But particularly noteworthy are the variations observed on March 14, 15 and 16 2002 in the 276° longitude sector (S. America). On March 14 and March 16, the peak *NmF2* of the southern anomaly crest is roughly 1.3×10^6 cm^{-3}, but the *NmF2* doubles to 2.6×10^6 cm^{-3} on March 15. A similar jump is observed from March 7 to March 8, 2002 in the same longitude sector. Very large *NmF2*s were observed in this longitude sector by GUVI (Figure 3-13) and were conjectured to be attributed to contamination by photoelectrons, largely because the same densities were not observed by LORAAS on that day. It is unfortunate that LORAAS did not have more consecutive days of observations in this longitude sector; however comparisons with the South American chain of ionosondes [*Valladares et al.*, 2001] could be carried out to verify our results.

We also show the variation of the *hmF2* of the northern crest (Figure 3-32 and Figure 3-33) and southern crest (Figure 3-34 and Figure 3-35). Immediately obvious is the fact that the southern anomaly crests are at a higher altitude than the northern crests. Also, the *hmF2*s of the both anomaly crests are generally higher in 2002 than in 2001. In March 2001, all of the daily variations in crest height are less than 50 km. However, in March 2002, there are several instances of ~80 km differences in height from one day to the next. For example, in Figure 3-33 the northern anomaly *hmF2* in the 12° longitude sector jumps from 270 km on March 4, 2002 to 360 km the following day. A similar increase is also observed in the southern hemisphere in the 180° longitude sector on March 9 and March 10, 2002. Likely mechanisms for the differences include thermospheric wind, neutral composition and neutral temperature differences in the two hemispheres.
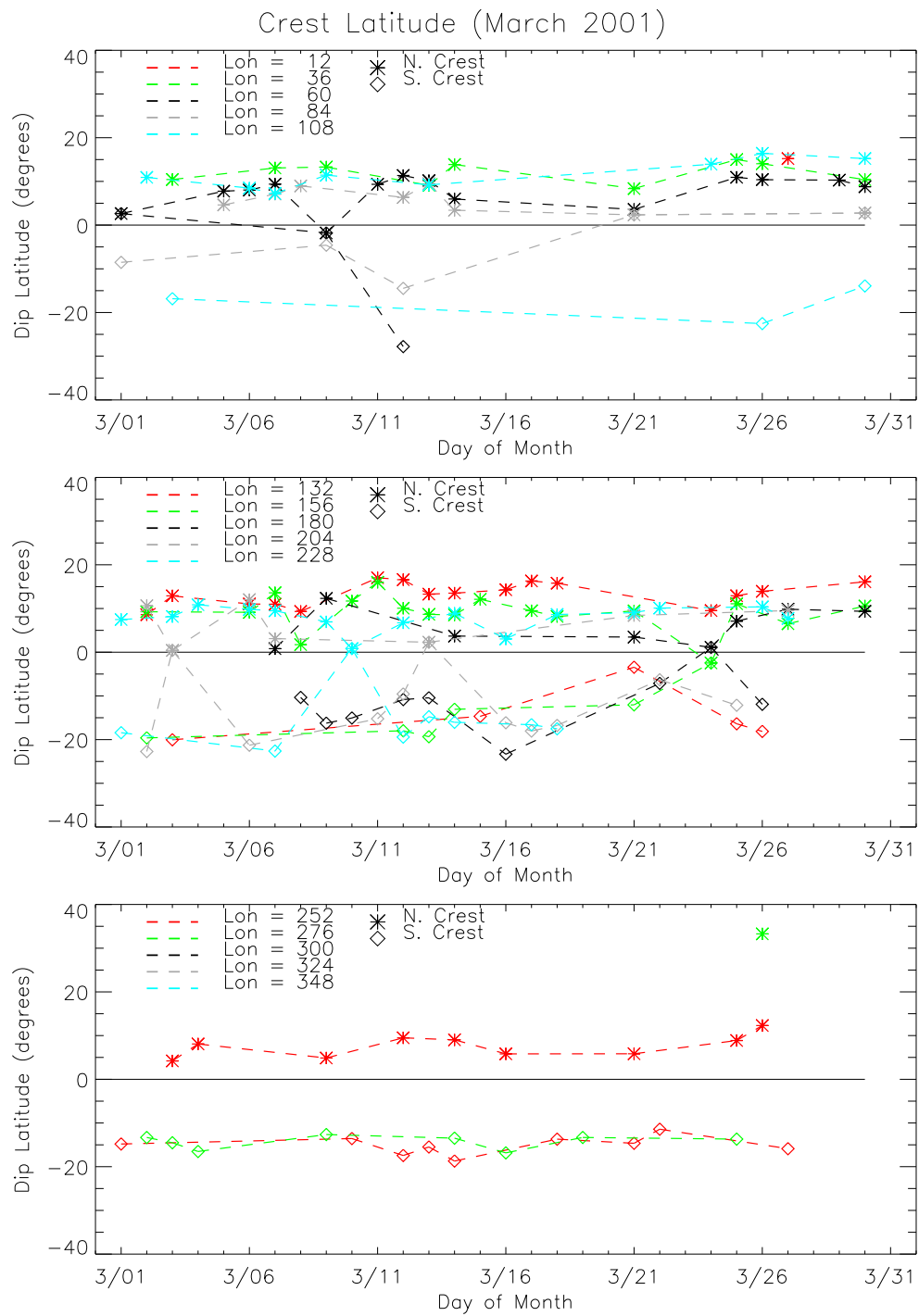
Figure 3-24 Anomaly crest location (dip latitude) for March 2001.

111
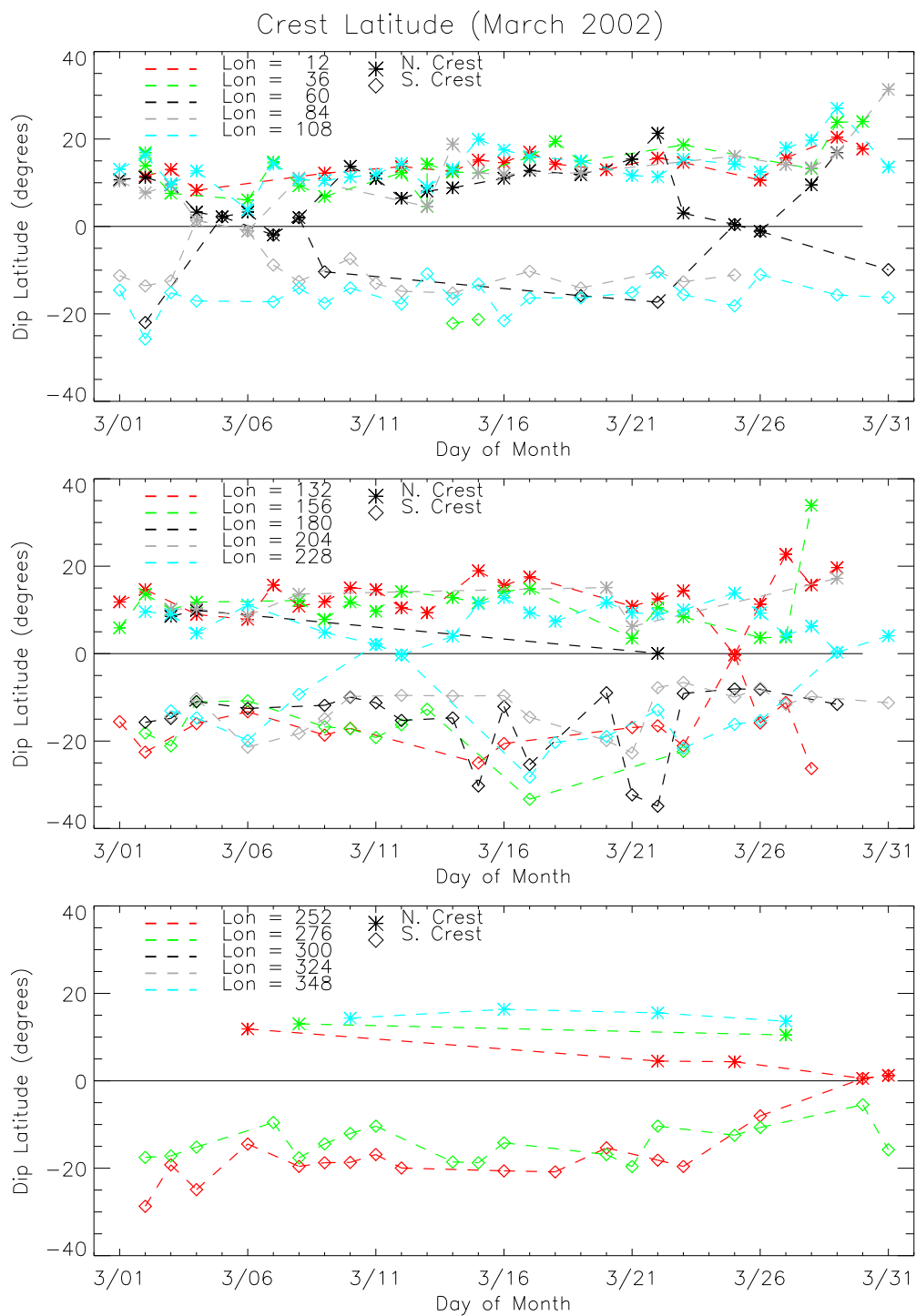
Figure 3-25 Anomaly crest location (dip latitude) for March 2002.

112
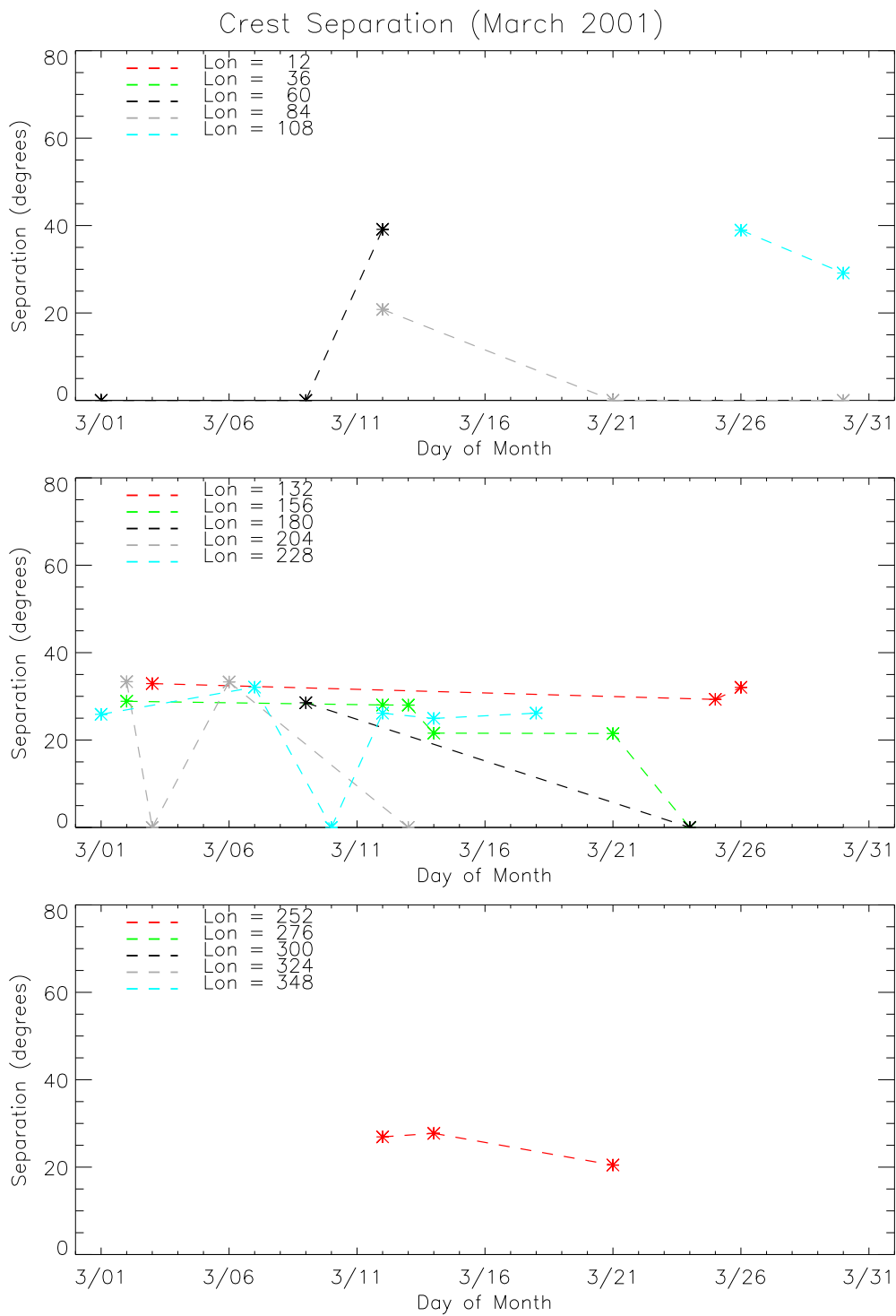
Figure 3-26 Anomaly crest separation (degrees dip) for March 2001.

113
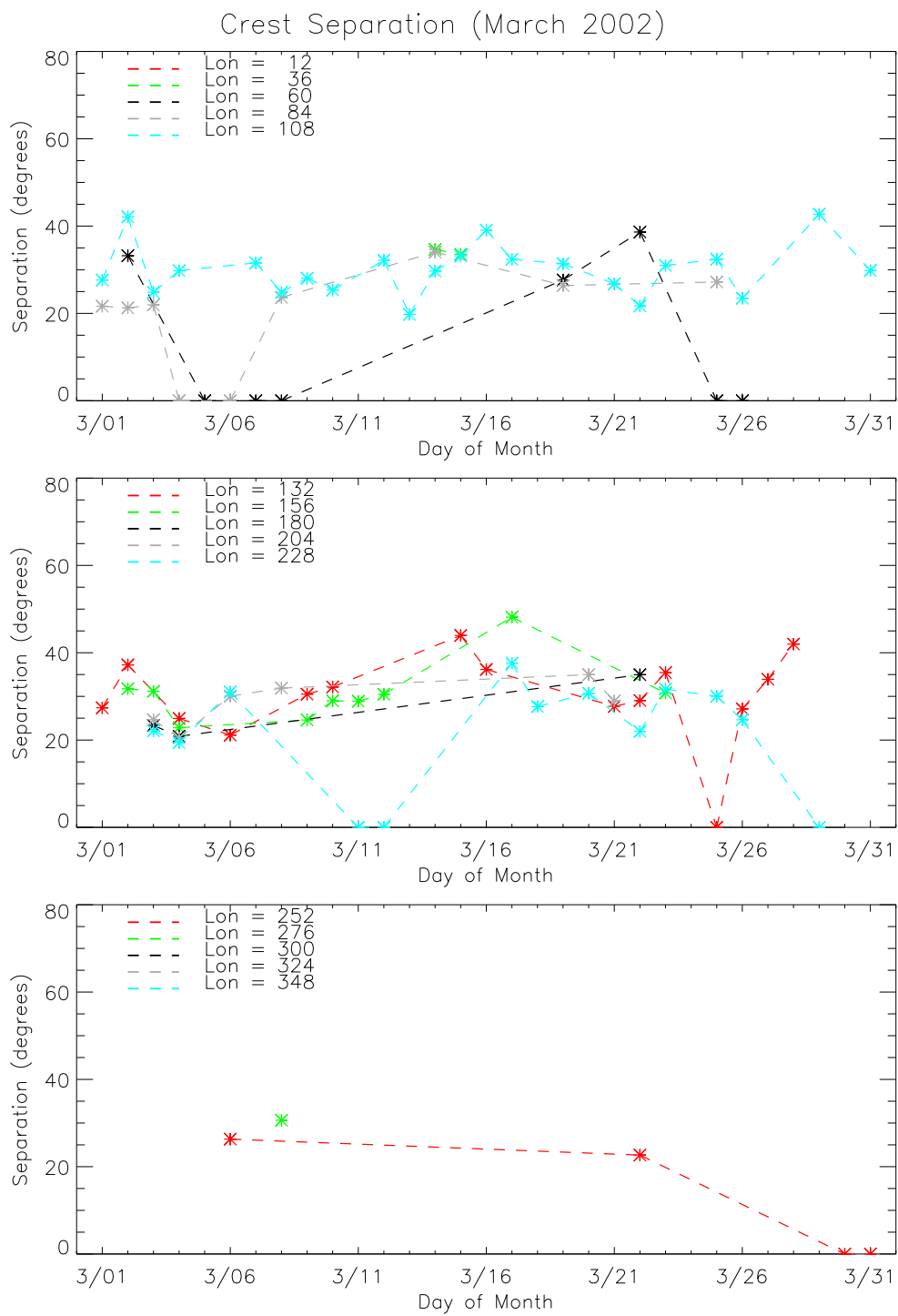
Figure 3-27 Anomaly crest separation (degrees dip) for March 2002.

114
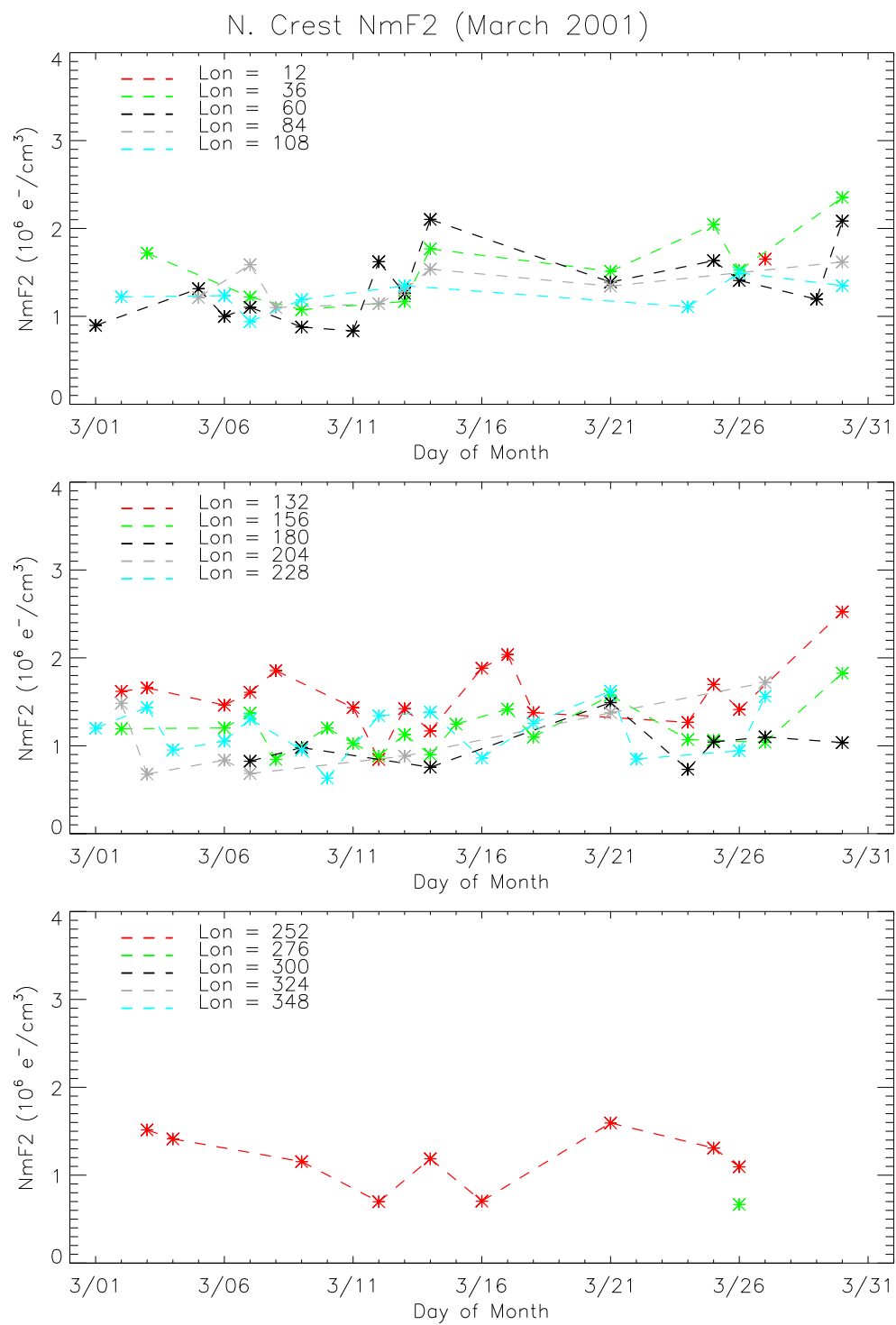
Figure 3-28 Northern anomaly crest peak density (*NmF2*) for March 2001.

115
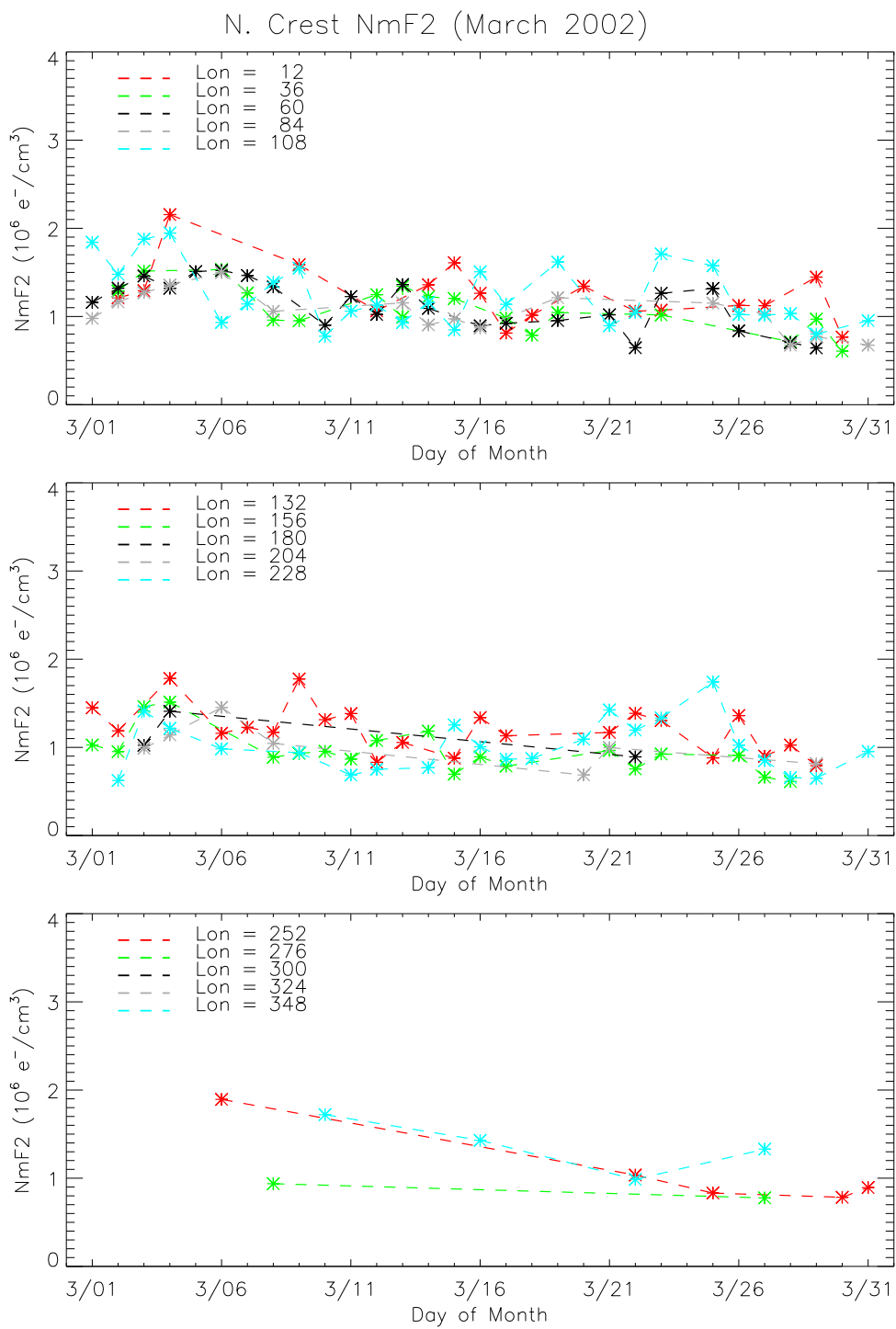
Figure 3-29 Northern anomaly crest peak density (*NmF2*) for March 2002.

116
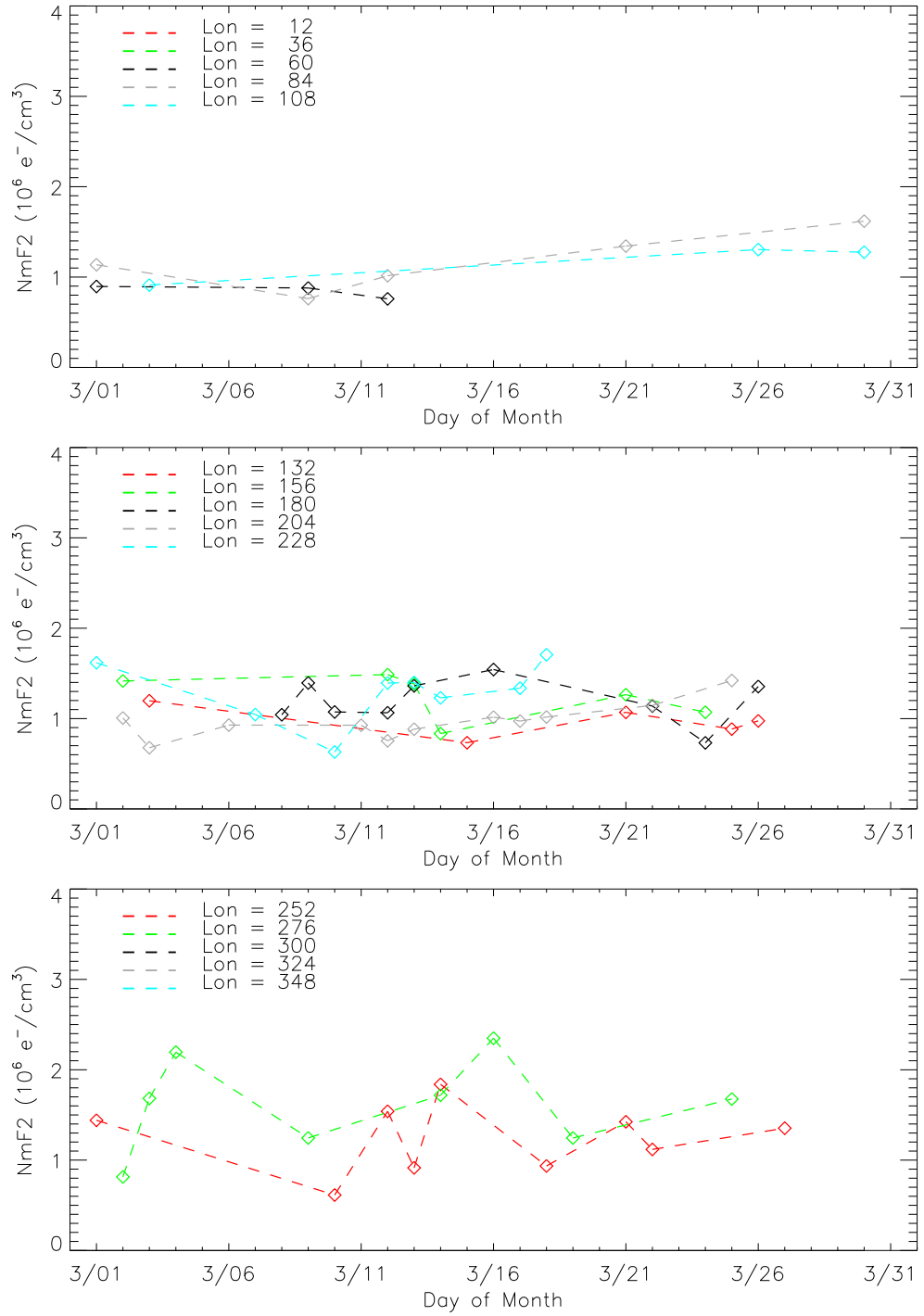
Figure 3-30 Southern anomaly crest peak density (*NmF2*) for March 2001.

117
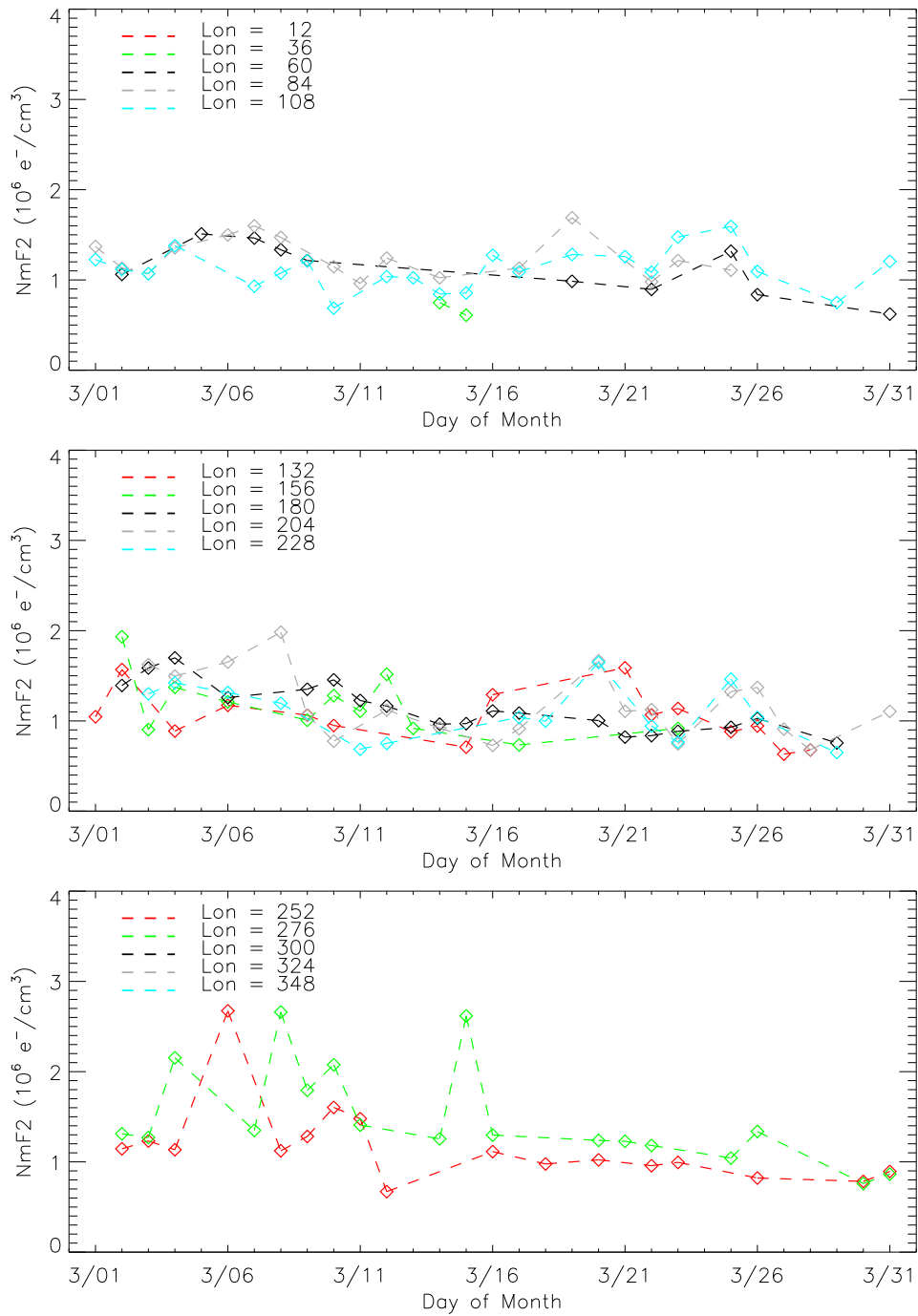
Figure 3-31 Southern anomaly crest peak density (*NmF2*) for March 2002.
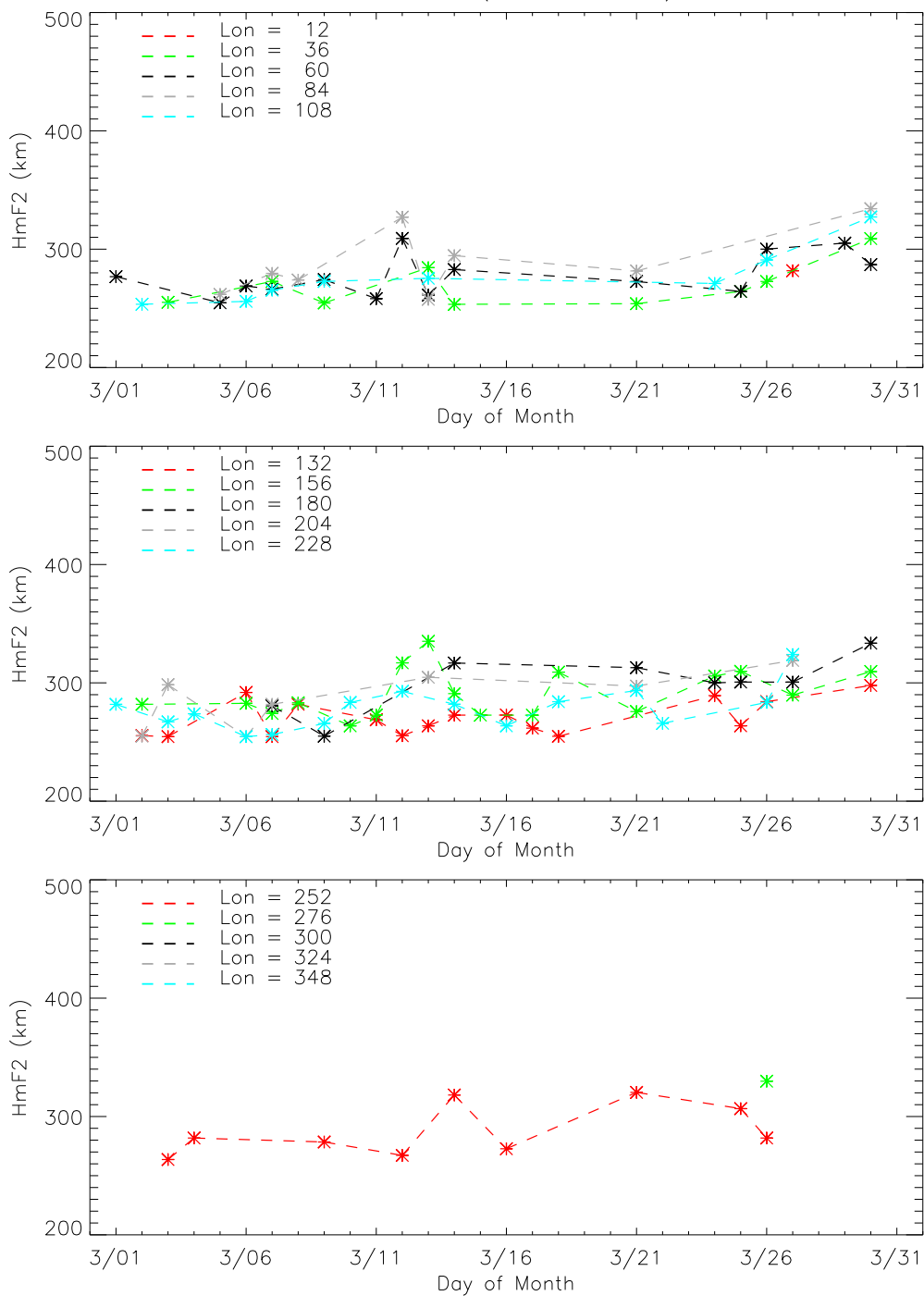
Figure 3-32 Northern anomaly crest peak height (*hmF2*) for March 2001.

119
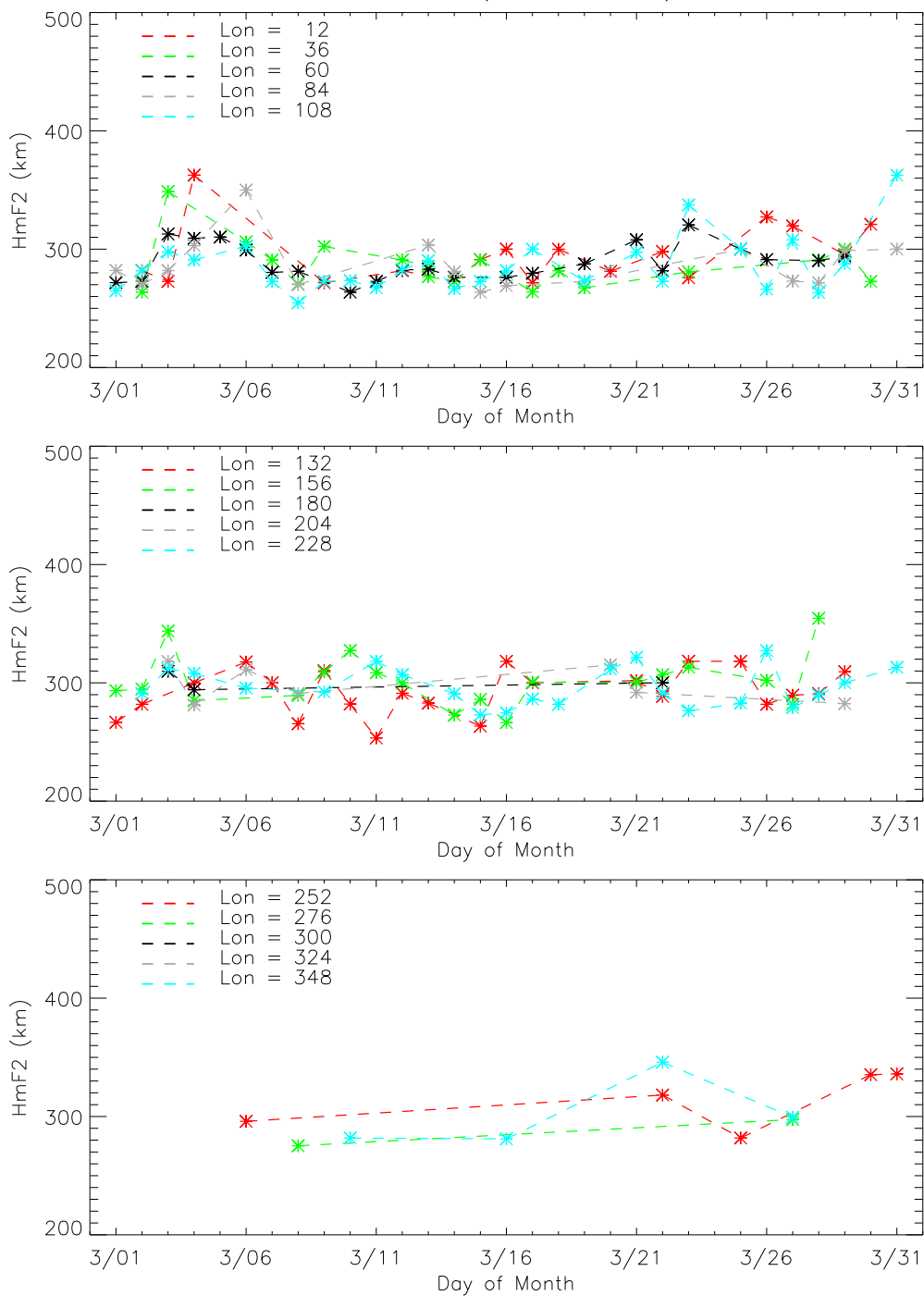
Figure 3-33 Northern anomaly crest peak height (*hmF2*) for March 2002.

120
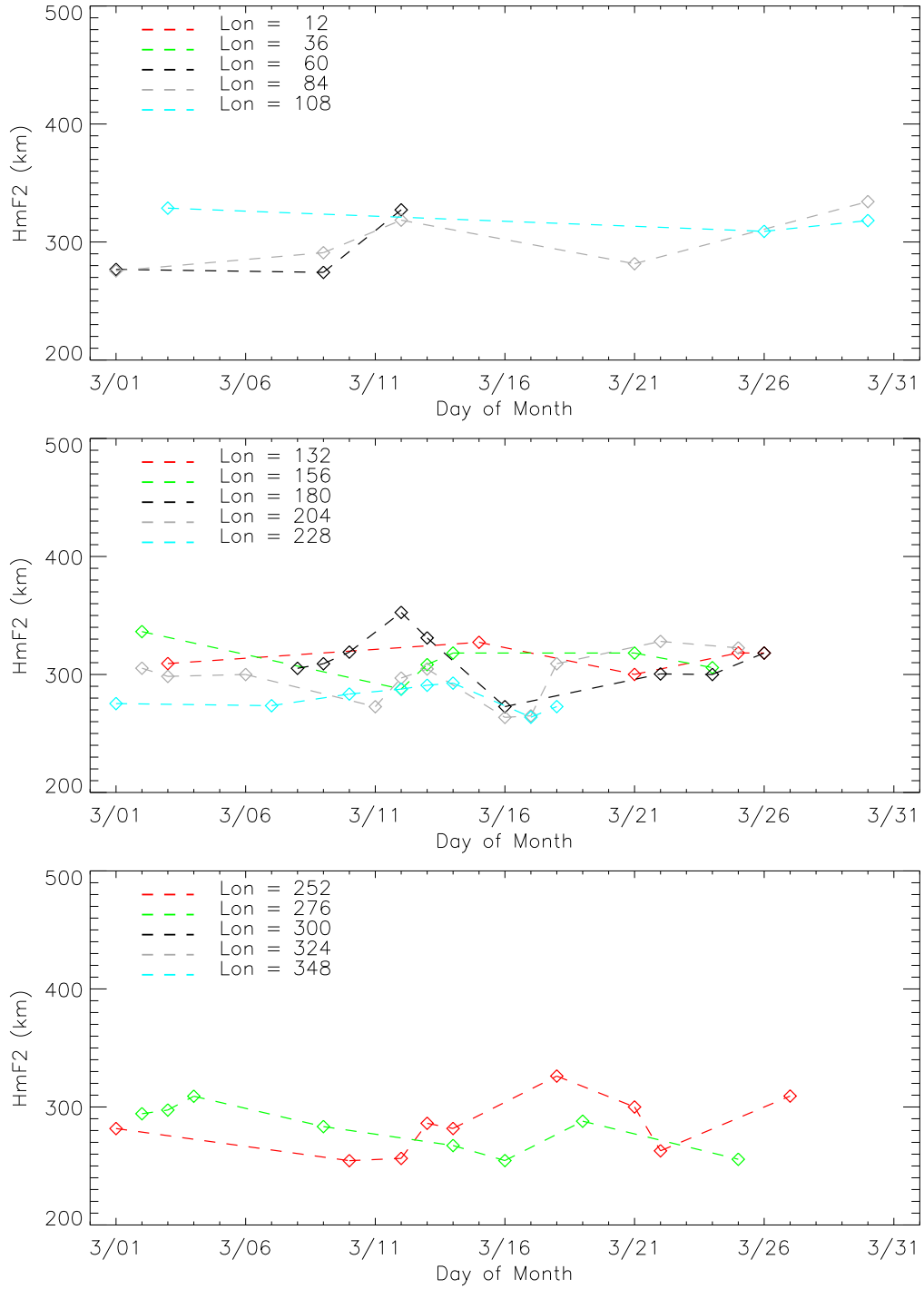
Figure 3-34 Southern anomaly crest peak height (*hmF2*) for March 2001.

121
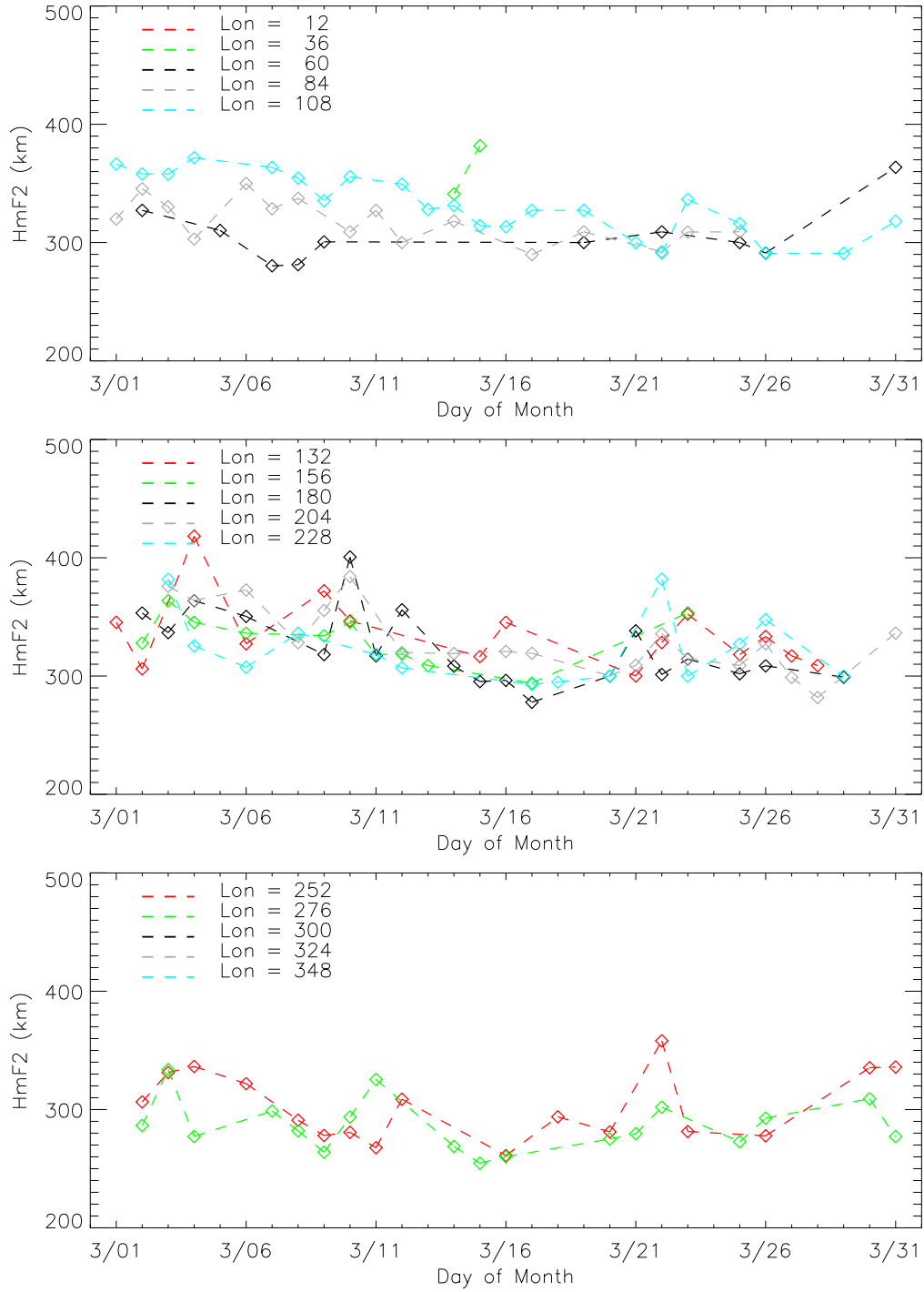
Figure 3-35 Southern anomaly crest peak height (*hmF2*) for March 2002.

122

To evaluate the monthly variability seen in the LORAAS data, we use the monthly mean (μ) and standard deviation (σ) [see for example *Forbes et al.*, 2000; *Rishbeth and Mendillo*, 2001; *Bilitza et al.*, 2004]. The relative standard deviation (RSD) is defined as the absolute value of the coefficient of variation (σ/μ) expressed as a percent:

$$RSD[\%] = \left| \frac{\sigma}{\mu} \right| \times 100. \qquad (3\text{-}4)$$

The error associated with the monthly mean is given by

$$\sigma_M = \frac{\sigma}{\sqrt{N}} \qquad (3\text{-}5)$$

where N is the number of samples in the month. The error associated with the standard deviation is

$$\sigma_S = \frac{0.71\sigma}{\sqrt{N}}. \qquad (3\text{-}6)$$

The error associated with the RSD is determined by propagating the monthly mean error and standard deviation error [*Bevington*, 1969], such that

$$\sigma_{RSD} = RSD\sqrt{\left(\frac{\sigma_M}{\mu}\right)^2 + \left(\frac{\sigma_S}{\sigma}\right)^2} . \qquad\qquad (3\text{-}7)$$

Table 3-4 summarizes the monthly mean and RSD for various observable characteristics of the equatorial anomaly across all longitudes for March 2001 and March 2002. The most variable features in both years are the latitudes, separation and widths of the anomaly crests, which vary from $40 - 67\%$. The peak densities of the crests and the north/south ratio of the densities vary on the order of 30%. This result compare well with previous studies of *NmF2* in the anomaly crest that report $25 - 35\%$ 1σ (one sigma) variability at night [e.g. *Forbes et al.*, 2000; *Rishbeth and Mendillo*, 2001]. By far, the least variable characteristic is the height of the anomaly crests, with $8 - 9\%$ variability.

Overall, slightly more variability is observed in March 2001 than March 2002, but this can be attributed to both the smaller sample size and larger variation in solar flux in the 2001 dataset. In comparison with March 2001, the March 2002 crest separation and *hmF2* are higher, while the *NmF2* is slightly lower. Though it is difficult to extract trends from only two months of data, the differences between the years could be attributed to the fact that the mean 81-day average solar flux was higher in March 2002 than in March 2001. Enhanced solar energy deposition into the thermosphere leads to stronger F region zonal neutral winds that in turn increase the prereversal $\mathbf{E} \times \mathbf{B}$ drifts; this results in a greater separation of the anomaly crests. Stronger F region winds can also explain the

124

higher altitudes of the anomaly crests. We expect the *NmF2* to also be higher with greater

solar flux, but this is not observed.

Table 3-4 Summary of Equatorial Anomaly monthly mean and RSD values.

| | March 2001 | | March 2002 | |
| | F10.7 = 166, Ap = 20.2 | | F10.7 = 191, Ap = 10.4 | |
	μ	RSD (%)	μ	RSD (%)
Separation	20.50	66.88	25.39	46.40
N. Latitude	9.26	50.86	11.45	49.96
S. Latitude	-13.05	53.72	-14.45	47.27
N. NmF2	1.28×10^6	28.91	1.12×10^6	26.79
S. NmF2	1.20×10^6	29.17	1.17×10^6	30.77
N. HmF2	282.10	7.73	292.78	7.14
S. HmF2	297.10	7.80	319.49	9.44
N/S NmF2 Ratio	1.06	32.08	1.05	30.48
N. Width	23.13	38.48	22.54	41.17
S. Width	-	-	22.39	40.96

Monthly mean and RSD values for several observable characteristics of the equatorial anomaly for March 2001 and March 2002 are shown. For March 2001, the number of N. crest observations is 113, the number of S. crest observations is 67, and there are 32 instances where both crests are observed in the same pass. For March 2002, there are 185 N. crest observations, 163 S. crest observations and 92 observations that include both crests. There is insufficient information to determine the width of the southern anomaly crests in March 2001.

Though there may be some correlation between solar flux and the average

characteristics of the equatorial anomaly, we find that the day to day variability is not

strongly associated with $F_{10.7}$, as is illustrated in Figure 3-36(a). We compare our results

with IRI-90, which shows a correlation between the density and solar flux at 2000 LT

(Figure 3-36(c)) and a weak correlation at 0230 LT (Figure 3-36(b)). Likewise, we did

not find a correlation between solar flux and *hmF2* or anomaly crest latitude. We also

investigated the possibility of correlations among the various observable characteristics.

Figure 3-37 shows *NmF2* as a function of anomaly crest latitude. At densities less than

1.7×10^6 cm^{-3}, the anomaly crests range in latitude from 0° to 35°. But at higher densities,

the crests fall within a much narrower range. The IRI-90 results show that *NmF2* increases slightly with dip latitude and the range remains fairly constant. IRI-90 also shows the southern anomaly at a higher latitude than the northern anomaly, which is consistent with the mean values shown in Table 3-4. A possible explanation for our results is that when the upward $\mathbf{E} \times \mathbf{B}$ drifts are weak, less plasma is pumped up to higher altitudes and the crests remain close to the magnetic equator. If the winds near the equator are strong, the crests may not decay very rapidly, despite being relatively low in density in the early evening. As discussed above, anomaly crests identified above 20° dip latitude may in fact be enhancements in the midlatitude ionosphere due to strong equatorward winds at these latitudes. Such midlatitude enhancements do not have particularly high densities.

We looked for correlations in an observed characteristic with longitude. For example, we attempted to determine whether or not the *NmF2* observed in one longitude sector correlated with the *NmF2* observed in another longitude sector on the same day. Determining whether such correlations exist is particularly important to the data assimilation community, where correlations between measurements can be used to provide an estimate for missing data. We found that the LORAAS data do not show any correlations between the observed characteristics of the anomaly region with longitude. This result indicates that the length scales of the dominant processes affecting the equatorial anomaly at 0230 LT are less than the size of our longitude bins (24°).
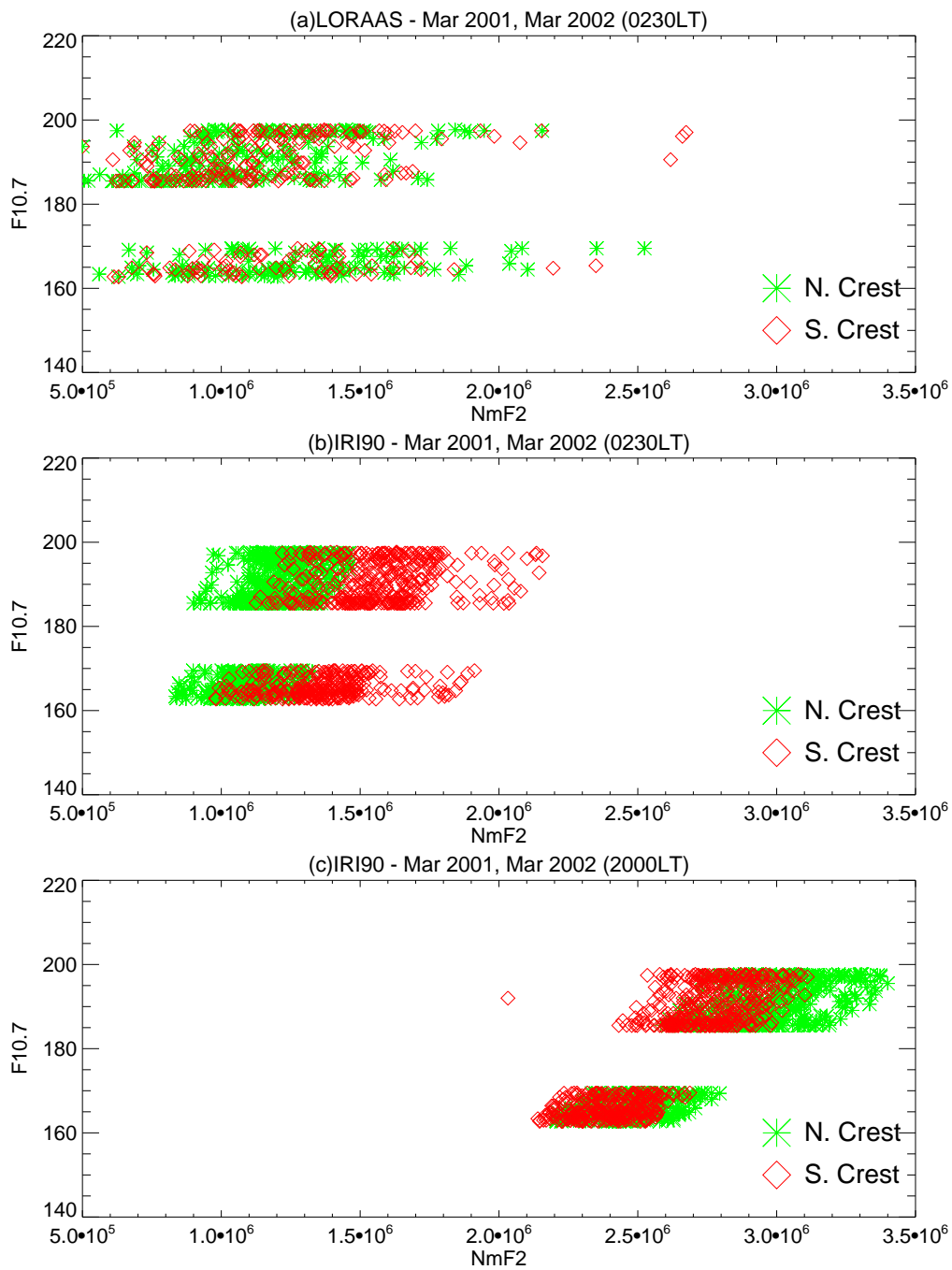
Figure 3-36 NmF2 as a function of $F_{10.7}$ for March 2001 and March 2002.

127
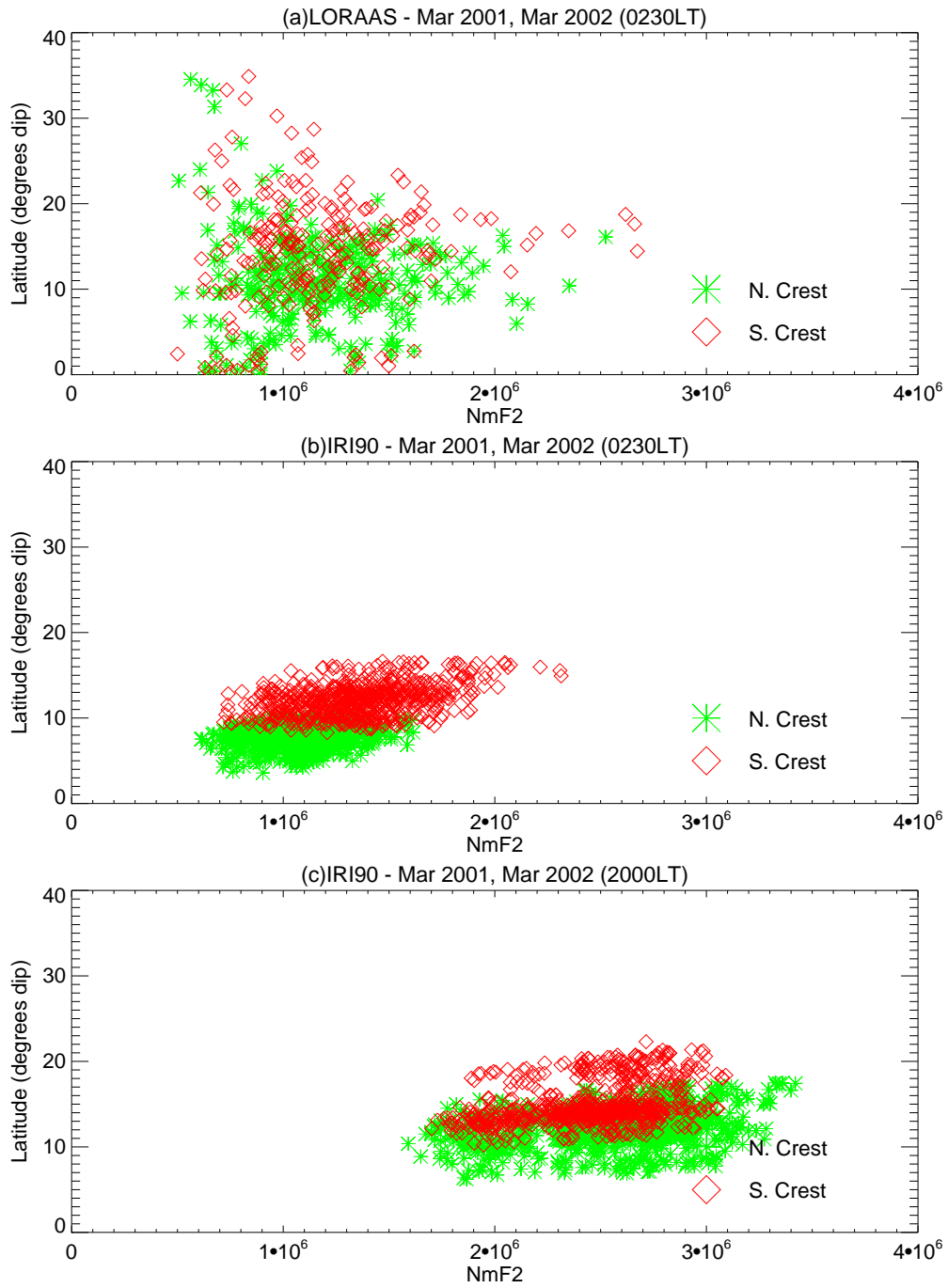
Figure 3-37 *NmF2* as a function of dip latitude for March 2001 and March 2002.

3.6 Comparisons with Models

We compare the LORAAS results with the International Reference Ionosphere (IRI-90), an empirical climatology model of the *F* region ionosphere. We use IRI-90 to calculate the vertical electron density profiles for March 2001 and March 2002 at the LORAAS tangent point latitudes and longitudes over the altitude range from 100 to 1000 km. We also use the 81-day average $F_{10.7}$ index for March 2001 and March 2002 as an input. We then combine the two months to calculate the mean and standard deviation of the mean using the same algorithms developed for the identification of the LORAAS anomaly crests. The model results are compared with the LORAAS values.

Figure 3-38 shows the mean and 1σ standard deviation from the mean of the northern and southern anomaly crest dip latitude for the LORAAS data and the IRI-90 model runs. IRI-90 shows little variation in the latitude of the anomaly crests as a function of longitude. The LORAAS data, however, show a wave-like pattern, with the anomaly crests located closer together in the 60° and 180° longitude sectors and farther apart in the 132° longitude sector. This pattern can also be seen in Figure 3-39, which shows the anomaly crest separation. In the postsunset hours, the anomaly crest separation is known to be controlled by the strength of the upward $\mathbf{E} \times \mathbf{B}$ plasma drift. Strong upward drifts occurring during the day or early evening hours push the equatorial plasma to higher altitudes, resulting in anomaly crests that form at higher magnetic latitudes. Observations with IMAGE FUV show a similar longitudinal pattern in the latitude of the northern anomaly crest [*Sagawa et al.*, 2005; *Immel et al.*, 2006]. *Immel et al.* [2006]

129

show that the longitudinal structure is likely tied to the non-migrating diurnal atmospheric tides driven by tropospheric weather in the tropics. We explore the wavelike longitudinal pattern in the LORAAS data in more detail in Chapter 4.

Figure 3-40 and Figure 3-41 show the mean and standard deviation about the mean northern and southern anomaly crest *NmF2*, respectively. The IRI-90 densities show considerable variation (~10%) due to the change in solar flux from March 2001 to March 2002, especially the southern anomaly crest. In contrast, as shown above, the variability of the LORAAS data is not strongly tied to the solar flux.

Figure 3-42 and Figure 3-43 show the mean and standard deviation about the mean *hmF2* of the northern and southern anomaly crests. The data show that the peak heights of the postmidnight anomaly crests do not vary significantly as a function of longitude and agree fairly well with IRI-90. The average altitude of the $F2$ peak is 290 km in the northern crest and 313 km in the southern crest; the IRI-90 model gives an average altitude of 304 km and 314 km respectively. We suspect the north/south height asymmetry is primarily due to seasonal hemispheric differences in the neutral winds.

Figure 3-44 and Figure 3-45 show the mean and standard deviation about the mean anomaly crest width in comparison with IRI-90. In comparison with the other parameters, IRI-90 shows considerable longitudinal variation in the widths of the northern and southern anomaly crests; but these longitudinal variations do not agree with

what is observed by LORAAS. We suspect that thermospheric winds play the largest role in determining the latitudinal extent of enhanced density in the postmidnight sector.

Overall, we find that the IRI-90 results show no significant variation from day to day or within a longitude bin, which is reflected in the small 1σ standard deviation about the mean. In most longitude sectors we do find that the model results fall within 1σ standard deviation of the LORAAS parameters. However, it is also evident that even the LORAAS mean values can significantly deviate from the model. Longitudinal trends in the LORAAS data generally do not match that of the IRI-90 results.
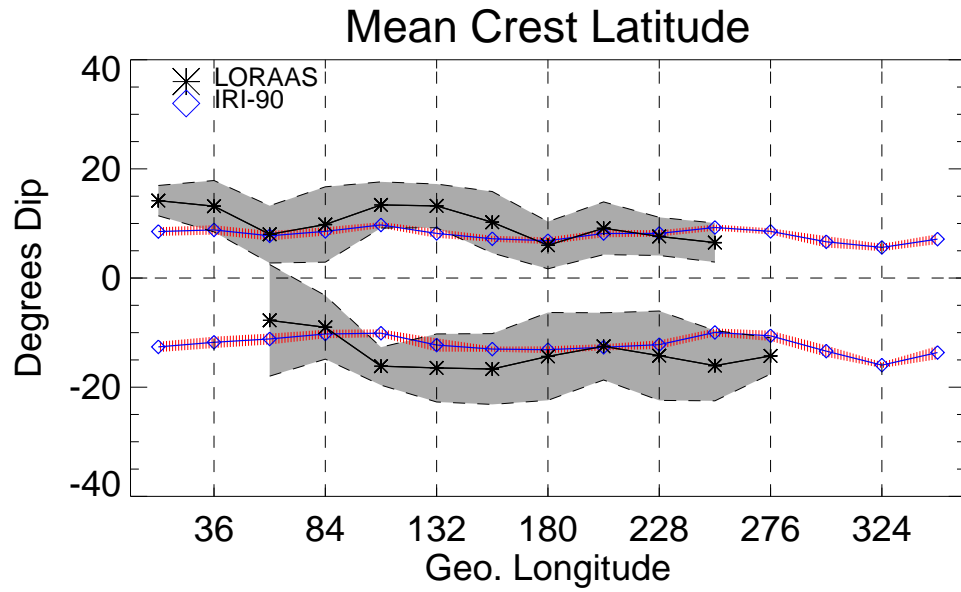
Figure 3-38 Mean and 1σ relative standard deviation about the mean north and south anomaly crest dip latitude as a function of longitude for March 2001 and March 2002 is shown for the LORAAS data and IRI-90 model.
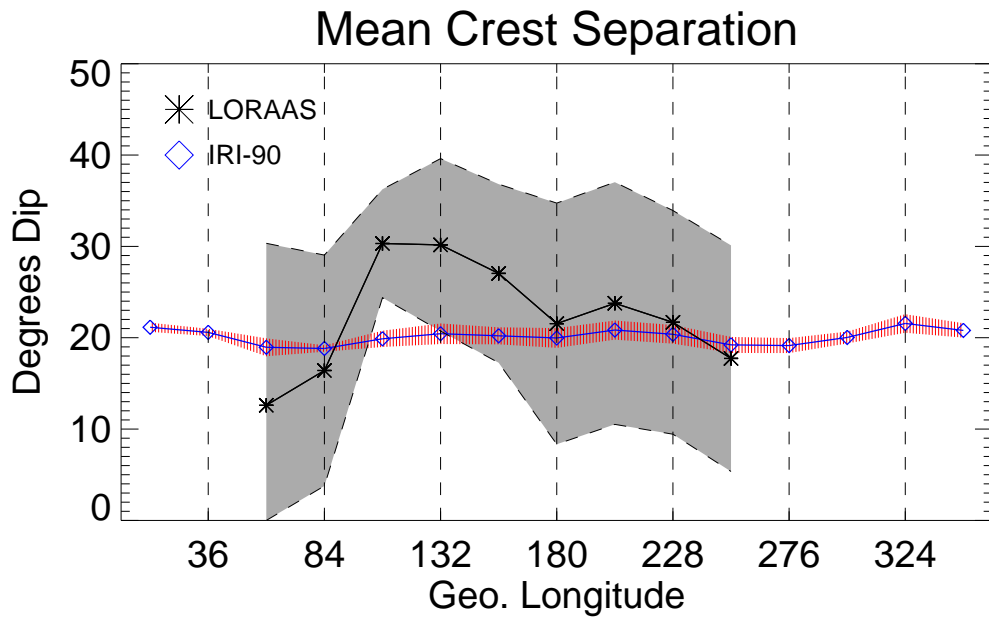
Figure 3-39 Mean and 1σ relative standard deviation about the mean north and south anomaly crest separation as a function of longitude for March 2001 and March 2002 is shown for the LORAAS data and IRI-90 model.
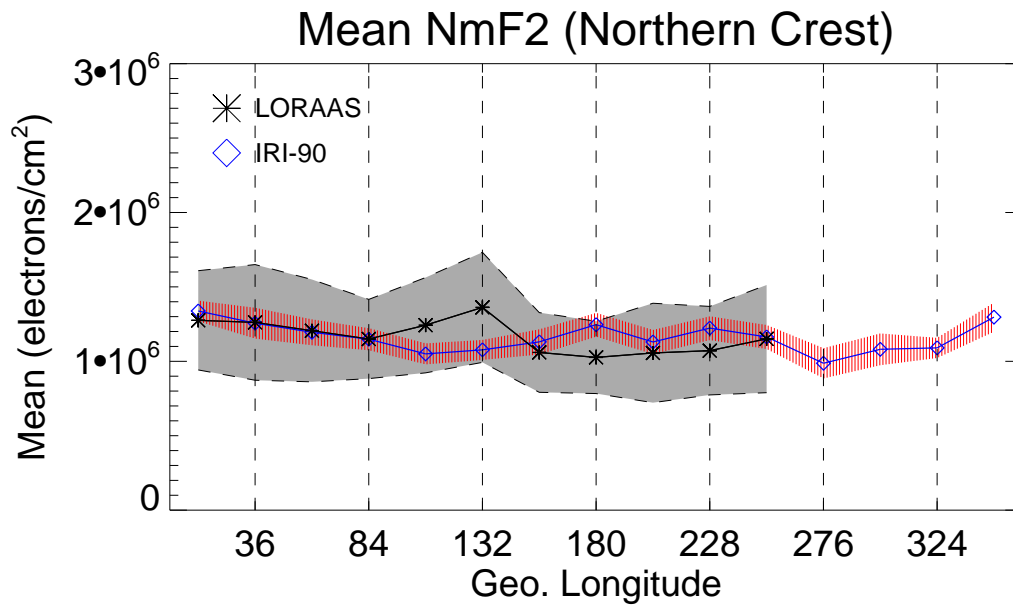
Figure 3-40 Mean and 1σ relative standard deviation about the mean northern anomaly *NmF2* as a function of longitude for March 2001 and March 2002 is shown for the LORAAS data and IRI-90 model.
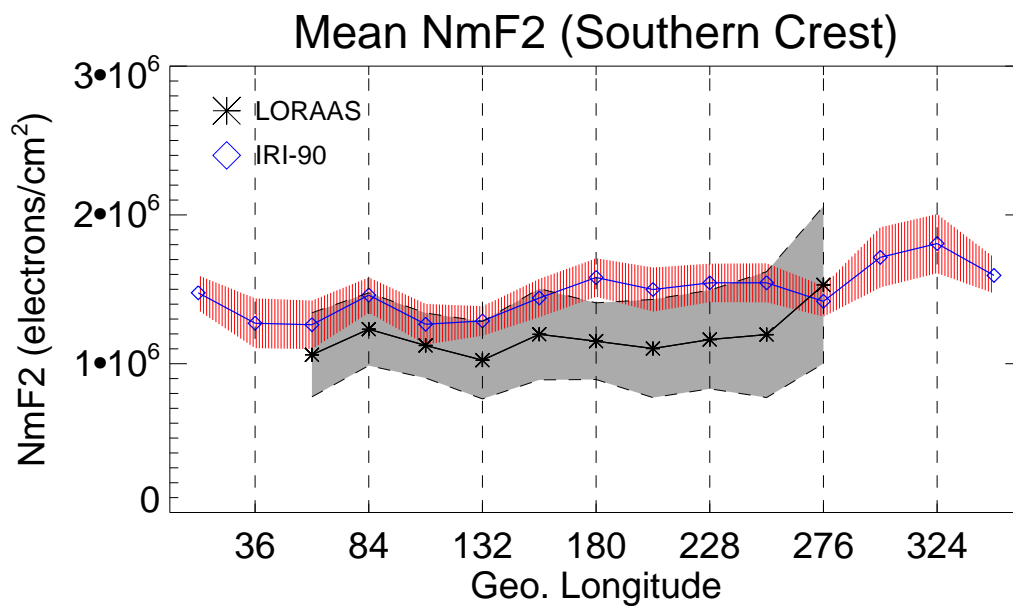
Figure 3-41 Mean and 1σ relative standard deviation about the mean southern anomaly *NmF2* as a function of longitude for March 2001 and March 2002 is shown for the LORAAS data and IRI-90 model.
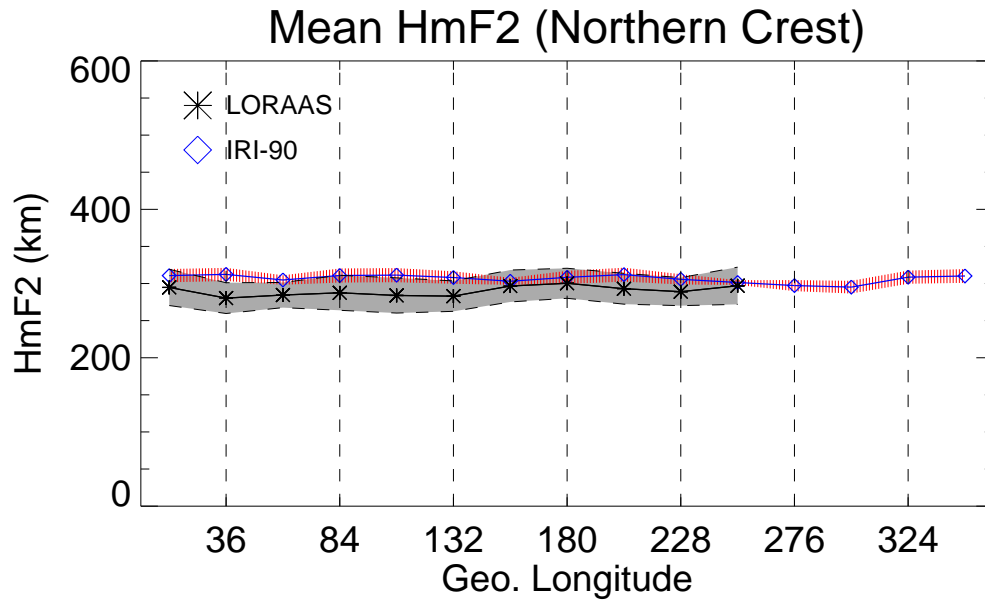
Figure 3-42 Mean and 1σ relative standard deviation about the mean northern anomaly *hmF2* as a function of longitude for March 2001 and March 2002 is shown for the LORAAS data and IRI-90 model.
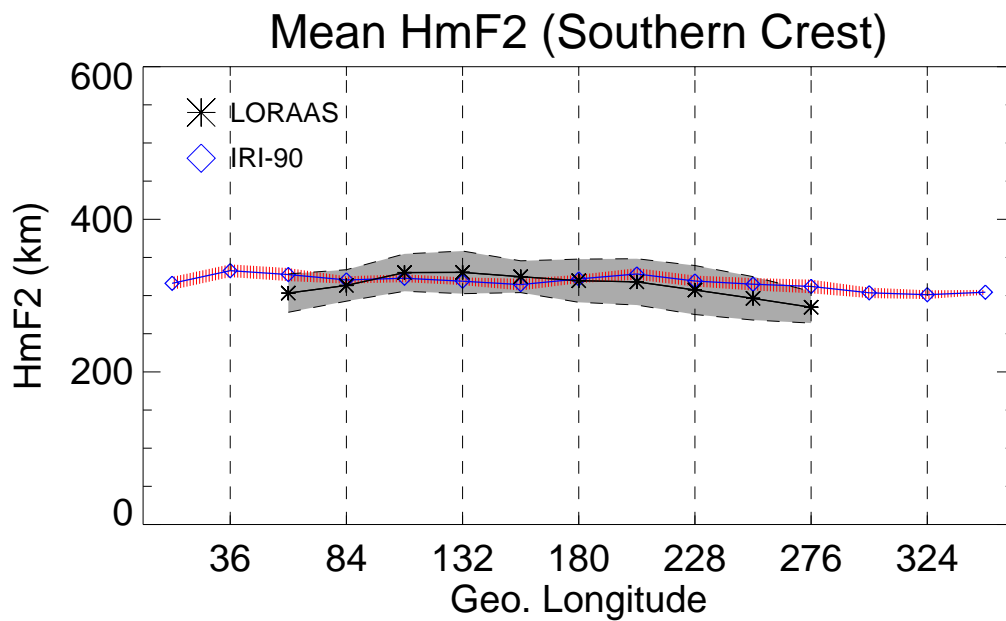
Figure 3-43 Mean and 1σ relative standard deviation about the mean southern anomaly *hmF2* as a function of longitude for March 2001 and March 2002 is shown for the LORAAS data and IRI-90 model.

134
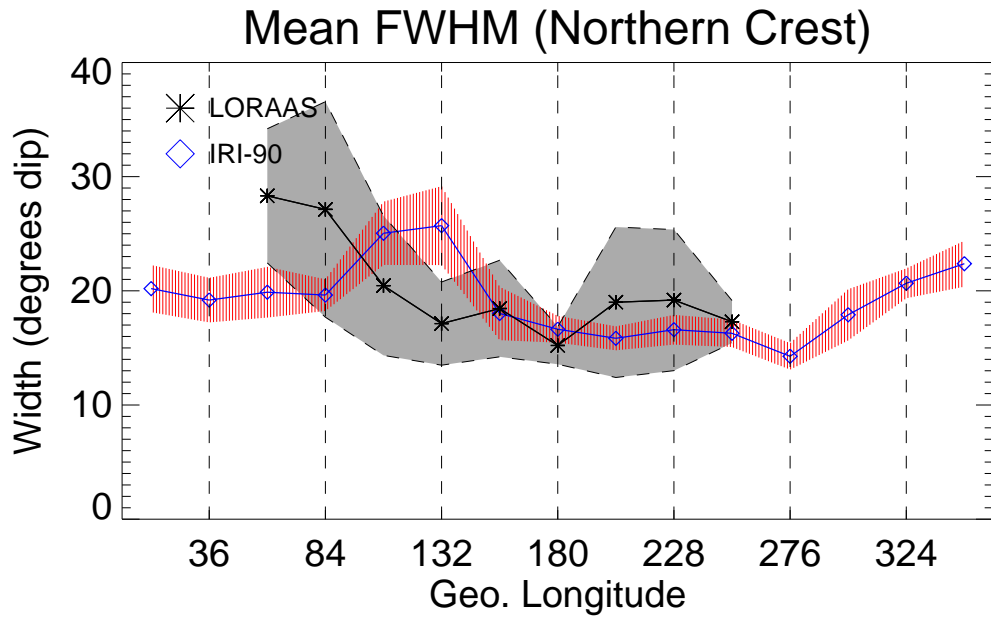
Figure 3-44 Mean and 1σ relative standard deviation about the mean width of the northern anomaly as a function of longitude for March 2001 and March 2002 is shown for the LORAAS data and IRI-90 model.
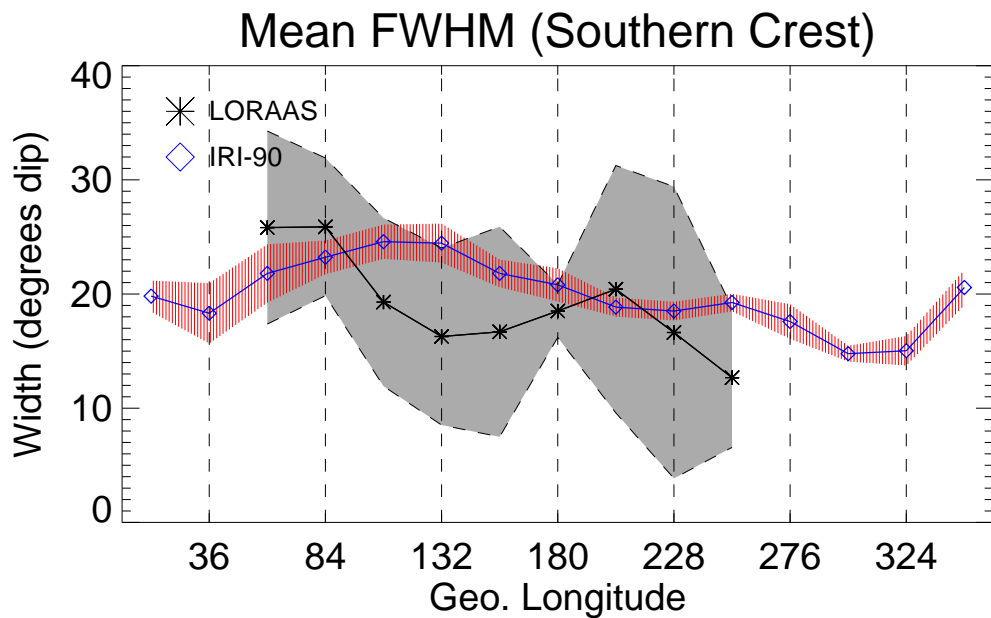
Figure 3-45 Mean and 1σ relative standard deviation about the mean width of the southern anomaly as a function of longitude for March 2002 is shown for the LORAAS data and IRI-90 model. Since March 2001 data do not include sufficient information to determine the southern anomaly crest width, only March 2002 data and model results are shown here.

135

3.7 Summary

We have used a two-dimensional inversion algorithm to derive electron densities from limb scans gathered from LORAAS measurements of the O I 135.6 nm emission feature in the nighttime F region ionosphere. We showed that the algorithm can reproduce the equatorial anomaly crests in the postmidnight sector, where densities typically fall below 1.0×10^6 cm^{-3}. Our comparisons with ionosonde data show the LORAAS $NmF2$s are often in very good agreement with that of the ionosondes, especially when the LORAAS measurements are within 3° latitude and 5° longitude of the ionosonde. The differences between the LORAAS and ionosonde densities increase with increasing distance between the measurements. Comparisons with GUVI derived densities, using the 1-D inversion algorithm, show the positions of the anomaly crests match fairly well. The mean difference in the $hmF2$ between the two datasets is 16 km. If the GUVI densities are assumed to be correct, LORAAS appears to underestimate the $NmF2$ in the anomaly crests and overestimate the $NmF2$ of the trough region. There is a mean difference of 2.0×10^5 cm^{-3} between GUVI and LORAAS $NmF2$s. It was found that the regularization parameter applied to the two-dimensional algorithm may overly smooth the densities (see Appendix), causing the discrepancy between the GUVI and LORAAS $NmF2s$. Additional investigations should be undertaken to determine if there are improvements that can be made to the inversion algorithm and regularization technique in order to produce more accurate peak densities, especially in the anomaly crests. Also, more comprehensive validation of the LORAAS densities, as well as the GUVI densities, is needed.

Next, we looked at the day to day variability of several parameters of the F region ionosphere that are associated with the equatorial anomaly. Specifically, we looked at the latitudinal separation, dip latitude, peak electron density (*NmF2*), peak height (*hmF2*), north/south ratio of *NmF2*, and the widths of the northern and southern anomaly crests as a function of longitude. We found that the anomaly crests are nearly symmetric about the dip equator to within ~5°, but the southern anomaly crests occasionally appear to be shifted southward. Preliminary modeling studies with SAMI2 suggest that the southern hemisphere enhancement may not be the southern anomaly crest but a midlatitude feature maintained by a strong equatorward wind. Additional modeling and observational studies should be conducted to determine if this is in fact the case. Our study of the anomaly crest latitudes also indicate a wave-like pattern, with the anomaly crests generally closer together in the $60° - 84°$ and $180°$ longitude sectors and farther apart elsewhere. The sectors where the anomaly crests are close together also have a higher incidence of "collapsed" crests, where only a single enhancement is observed at the dip equator. Such collapsed arcs have been observed at dusk in the African-Indian longitude sector [*Basu et al.*, 2006], thus we suggest that it would be interesting to investigate their relationship to the features we observe in the postmidnight hours.

The peak densities in the anomaly crests vary considerably from day to day. We observe that large density variations of nearly 1.0×10^6 cm^{-3} from one day to the next within a longitude sector are not uncommon. The largest variation, however, is

1.3×10^6 cm^{-3}. Peak heights in the anomaly crests generally vary less than 50 km on a day to day basis, but there are several cases where ~80 km differences in height are observed.

A comparison of the monthly mean and 1σ standard deviation of each of the anomaly parameters for March 2001 and March 2002 reveals that the most variable aspect of the anomaly crests is the latitude and separation, with the RSD varying between 46 – 67%. The least variable parameter is the *hmF2*, where the RSD was found to be 7 – 9%. The *NmF2*s and widths of the crests varied from 27 – 32%. The variability of the *NmF2* is comparable to that found by various ionosonde studies [e.g. *Forbes et al.*, 2000; *Rishbeth and Mendillo*, 2001; *Bilitza et al.*, 2004]. A comparison of the northern and southern anomaly crests shows that, on average, the densities are about the same, but that the northern crest is lower in altitude than the southern crest. The height asymmetry is likely due to hemispheric differences in the neutral winds. Comparing March 2001 with March 2002 shows that the crest separation is greater in March 2002, the *hmF2* is higher and that the *NmF2* is slightly lower. In March 2002, the 81-day average solar 10.7 index was higher than in March 2001. The enhanced solar energy can explain the greater separation in the anomaly crests and higher altitude of the *F* region ionosphere. But without additional validation of the LORAAS densities, especially the March 2001 densities, we cannot truly compare the densities between these months.

We have found that any correlation of the anomaly characteristics with solar flux is overwhelmed by the considerable day to day variability due to other sources. Also, we

found no correlation from one longitude sector to the next, indicating that the length scales of the processes that are responsible for the ionospheric variability are less than 24° longitude.

Next, we have compared the LORAAS mean values for the combined months of March 2001 and March 2002 with IRI-90 results. As expected, the model shows no significant variation in the anomaly parameters from day to day. An exception is the *NmF2*, which has some dependence on $F_{10.7}$. However, we have found that the corresponding variation of *NmF2* in the LORAAS data is not primarily related to $F_{10.7}$. Also, IRI-90 does not show significant longitudinal variation in the parameters, except for the anomaly crest widths.

3.8 Conclusion

An important result of this study is that we have demonstrated that the 2-D inversion technique for obtaining electron densities from UV limb scans is capable of characterizing important aspects of the ionosphere, such as *NmF2* and *hmF2*. *HmF2*, in particular, has not previously been well studied on global scales. We have also shown that some improvements should be made to the 2-D algorithm to improve its accuracy. Correctly identifying the amount of regularization to apply without overly smoothing the solution remains an outstanding issue.

We have used the LORAAS data to characterize the day to day variability of the postmidnight equatorial anomaly under geomagnetically quiet conditions at solar maximum. Much of the observed variability can be attributed to the actions of F region neutral winds. We did not find a significant correlation with the solar flux ($F_{10.7}$), which suggests that the lower atmosphere may be the primary driver of the variability. There is clearly a need to couple troposphere and thermosphere models to physics-based ionospheric models, such as SAMI3 and GAIM, in order to better understand the sources of variability. We anticipate that our results will be helpful in providing limits on the expected amplitude of variability that ionospheric weather models should be able to reproduce.

A future study will include an analysis of additional months in order to measure seasonal effects. Longer term studies will reveal correlations with solar flux and geomagnetic activity. Additionally, more concentrated studies on longitude specific behavior should be performed in order to gain a better understanding of the coupling between the lower atmosphere and the low latitude ionosphere.

4 Longitudinal Structure of the Low Latitude Ionosphere

Several recent studies suggest that non-migrating diurnal tides generated by tropical weather in the troposphere influence the longitudinal morphology of the low latitude F region ionosphere; in particular, a wave number four (wave-4) pattern is observed in the peak densities and magnetic latitudes of the equatorial anomaly. It is suspected that this variability is driven by E region processes on the dayside. Observations made with the Low Resolution Airglow and Aurora Spectrograph (LORAAS), which flew aboard ARGOS from May 1999 to April 2002, show additional evidence of periodic variations in the densities and latitudes of the equatorial anomaly crests. In this investigation, electron density profiles are reconstructed from limb scans of O I 135.6 nm emissions to obtain a map of the $NmF2$ at 0230 LT. Our findings show that the longitudinal variability of the $NmF2$ of the northern anomaly crest matches that of other global observations, but there is a pronounced hemispheric asymmetry in the longitudinal variations observed in the southern anomaly crest. We show that this asymmetry is tied to longitudinal variations in the neutral winds at F region altitudes, which act to enhance the observed wave-4 pattern. We discuss the role of the neutral winds by comparing the LORAAS results to both empirical (IRI-90) and physics-based models (SAMI2).

4.1 Introduction

Thermospheric neutral winds play a central role in the dynamics of the low latitude ionosphere. Winds in the lower thermosphere drive the E region dynamo producing ionospheric electric fields and currents. During daytime, the electric fields at the magnetic equator are eastward, which cause an upward plasma drift, while the reverse occurs at night. In the F region ionosphere, where electron-ion collisions are rare and charged particles interact weakly with the neutral atmosphere, electrons and ions drift together at a steady $\mathbf{E} \times \mathbf{B} / B^2$ velocity. Interaction between the E and F region dynamos and a build-up of electric charge at the sunset terminator results in a postsunset enhancement of the zonal electric field and hence the upward plasma drift in the early evening [*Woodman*,1970; *Farley et al.*, 1986]. This upward $\mathbf{E} \times \mathbf{B}$ drift, in combination with ambipolar diffusion along the geomagnetic field lines, results in a transport of ionization away from the magnetic equator toward higher latitudes [*Hanson and Moffett*, 1966]; this process is known as the "fountain effect". The plasma rises until pressure forces and gravity cause the plasma to descend along the field lines at tropical latitudes. The regions of enhanced plasma density in the $F2$ region, recognized by Appleton [*Appleton*, 1946], are known collectively as the equatorial anomaly, or Appleton anomaly.

Two direct influences on the morphology of the equatorial anomaly are the upward $\mathbf{E} \times \mathbf{B}$ drift and interhemispheric neutral winds. The strength of the $\mathbf{E} \times \mathbf{B}$ drift determines the maximum separation of the anomaly crests. A strong upward $\mathbf{E} \times \mathbf{B}$ drift

causes the plasma to drift to higher altitudes and thus diffuse down magnetic field lines to higher latitudes. Both meridional (north-south) and zonal (east-west) thermospheric neutral winds contribute to the field-aligned component of the *F* region winds that push the plasma up and down the magnetic field lines, often producing asymmetries in the densities of the northern and southern anomaly crests. Wind can move the plasma up to higher altitudes where recombination is slow, or push the plasma down the field lines to lower altitudes, where recombination is more rapid.

Seasonal and longitudinal variations in the densities and positions of the anomaly crests are attributed to the difference in 1) the alignment of the sunset terminator with the local magnetic meridian and 2) the location of the magnetic dip equator with respect to the geographic equator. The season in which the solar terminator aligns with the magnetic meridian produces a maximum in the eastward wind as well as a maximum in the longitudinal gradient of the integrated conductivity [*Abdu et al.*, 1981; *Batista et al.*, 1986], which results in a maximum $\mathbf{E} \times \mathbf{B}$ drift. The relative contribution of the zonal versus meridional winds to anomaly asymmetry varies with magnetic declination angle and hence with longitude. At the equinoxes, the meridional wind is typically at a minimum. Thus, for longitudes with small declination angles, the anomaly crests will be the strongest and most symmetric during the equinoxes. But there is substantial smaller scale variability as well as day to day variability that cannot be attributed to the aforementioned effects [e.g. *Walker et al.*, 1980; *Forbes et al*, 2000]. This variability is not well understood, but has been attributed to forcing from the lower atmosphere in the

143

form of tides [e.g. *Fesen*, 1997], planetary waves [e.g. *Forbes and Zhang*, 1997; *Altadill and Apostolov*, 2001; 2003], gravity waves [e.g. *Hocke and Schlegel*, 1996] and even infrasound [e.g. *Laštovička*, 2006; *Krasnov et al.*, 2003]. Atmospheric tides are global scale oscillations that are primarily forced by the absorption of solar radiation and large-scale latent heat release in the lower atmosphere and have periods that are harmonics of a solar day. Planetary waves are longer-period oscillations with periods ranging from 2 to 30 days. Both tides and planetary waves often dominate the meteorology of the region between 80 and 150 km [*Forbes*, 1995]. Processes that couple waves with ionospheric changes include: modifications of the thermospheric O and N_2 densities, influences on E region conductivities, modulation of temperature and wind structure of the thermosphere, and generation of electric fields through dynamo mechanisms [*Forbes*, 2000].

There have been numerous studies of longitudinal variations in the ionosphere using ground-based observations at fixed locations on the globe; though most studies have focused on large-scale differences that can be explained by the alignment of the magnetic field with the geographic coordinates [e.g. *Lyon and Thomas*, 1963; *Thomas*, 1968]. A few studies have indicated that there are also longitudinal variations on a smaller scale. *Walker et al.* [1980] observed large differences in the development of the equatorial anomaly between stations separated by only 40° longitude in East Asia and India, which were hypothesized to be due to upward propagating tides. More recently, a number of space-based observations indicate that there is a wave-like pattern (wave-4) to the longitudinal variability of various observables in the ionosphere. *Ivers et al.* [2003]

144

have used Ørsted satellite data to study the amplitude of the equatorial electrojet, an east-west current system that flows along the dip equator at ~105 km altitude, and have found that there are four maxima at 0° – 30° E, 90° – 120° E, 180° – 220° E and 260° – 290° E. *Jadhav et al*. [2002] found maxima in the width of the electrojet at 30°, 105° and 270° E using the same dataset. *Deminova* [2003] used Intercosmos-19 satellite topside sounding data to find a wavelike structure in the *F* region peak plasma frequency (*foF*2) of the nighttime low-latitude ionosphere with separations of 75° to 100° in longitude. Maxima in the anomaly crests were found to occur at longitudes near 30° E, 120° E and 200° E with little variation (less than 10° – 20°) for all local times and seasons during 1979 – 1981.

Recently, IMAGE FUV observations of the nighttime northern equatorial anomaly O I 135.6 nm emission feature have been used to discover a similar longitudinal pattern in the variation of the magnetic latitude of the anomaly crests and their peak intensity [*Sagawa et al*., 2005; *Immel et al*., 2006; *England et al*., 2006]. *Immel et al*. [2006] showed that the longitudinal structure was likely tied to non-migrating diurnal atmospheric tides driven by tropospheric weather in the tropics. Indeed, observations of the mesosphere-lower thermosphere region show that nonmigrating tides induce significant longitudinal local time variation of temperature between 80-120 km with a maximum amplitude of 8 – 20° K [*Forbes et al*., 2006]. *Immel et al*. [2006] postulate that such temperature variations modulate the *E* region dynamo electric fields and

subsequently the daytime upward $\mathbf{E} \times \mathbf{B}$ drifts, which drive the observed nighttime variations.

Measurements from the first Republic of China Satellite (ROCSAT-1) by *Kil et al.* [2007] support the claim that daytime processes drive the observed *F* region pattern. Their study revealed periodic maxima in the daytime $\mathbf{E} \times \mathbf{B}$ drift (1000 – 1100 LT) that were correlated with longitudinal maxima in the daytime plasma density at 600 km in the equatorial anomaly region. Furthermore, it was shown that the evening plasma drift did not exhibit a periodic longitudinal pattern, implying that the nighttime plasma distributions are indeed driven by the daytime drifts. However, hemispheric asymmetries in the nighttime *F* region plasma distributions were observed with both ROCSAT-1 and the Global Ultraviolet Imager (GUVI) aboard the NASA TIMED (Thermosphere Ionosphere Mesosphere Energy and Dynamics) satellite, which were suspected to be due to thermospheric neutral winds. *Lin et al*. [2007] used the FORMOSAT-3/COSMIC constellation of satellites to show a wave-4 longitudinal structure that also exhibited asymmetry between the northern and southern anomaly crests.

In this study, we present results from the Low Resolution Airglow and Aurora Spectrograph (LORAAS) that show large asymmetries in the longitudinal structure of the post-midnight electron densities. While the maxima of the northern anomaly crests are found at nearly the same longitudes as those specified by *Deminova* [2003], *Immel et al*. [2006] and *Sagawa et al.* [2005], the southern anomaly crest maxima are offset by ~60°

in longitude, roughly corresponding to the minima of the northern anomaly crests. We use modeling studies to show that neutral winds are responsible for producing the observed asymmetries of the longitudinal variations.

4.2 Observed Longitudinal Variability

To study the longitudinal variability of the low-latitude ionosphere under geomagnetically quiet conditions, we reconstructed the electron densities from LORAAS data collected in March 2001 and March 2002. March 2002 was chosen because it coincides with the timeframe of the *Sagawa et al*. [2006] and *Immel et al*. [2006] studies and it is a geomagnetically quiet month. The average $F_{10.7}$ for March 2002 was 178.4, average 3-hour Ap = 10.4 and there were two days with $Ap \geq 50$. March 2001 was chosen in order to study the year-to-year behavior of the longitudinal variability. March 2001 was also a fairly quiet month (average $F_{10.7}$ = 176.1, average 3-hour Ap = 20.2, Ap index exceeded 50 on 5 days).

We extracted the *NmF2* from the derived electron density profiles for each month, excluding active days with $Ap > 50$, and then rebinned the data into 1° latitude bins and 12° longitude bins. A map for March 2002 is shown in Figure 4-1. The equatorial anomaly region is clearly visible as the high density bands that follow the magnetic dip equator. Longitudinal variability in the separation of the anomaly crests is evident; the crests are closest together over India and furthest apart over Southeast Asia. Also quite noticeable is the wavelike longitudinal variation of the densities in the anomalies. There

147

is a lack of data over the South American and African regions due to high anomalous

counts in the instrument over the South Atlantic Anomaly (SAA). Some data are also

missing from the midlatitudes and polar regions because limb scans with insufficient

counts or with significant auroral contamination in the 135.6 nm feature were eliminated

from the inversion algorithm.
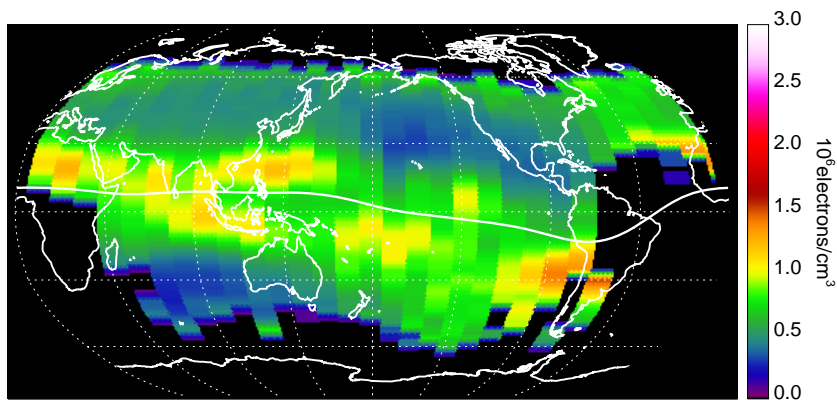
Figure 4-1 LORAAS derived *NmF2* from observations of the OI 135.6-nm emission feature at ~0230 LT. The *NmF2* data are binned and averaged over 1-31 March 2002. The dip equator is indicated. Some data are missing from the midlatitude and polar regions because limb scans with auroral contamination were excluded from the inversion algorithm. Missing data in the SAA region (South American and Africa) are due to high noise counts in the instrument as it flew over this region.
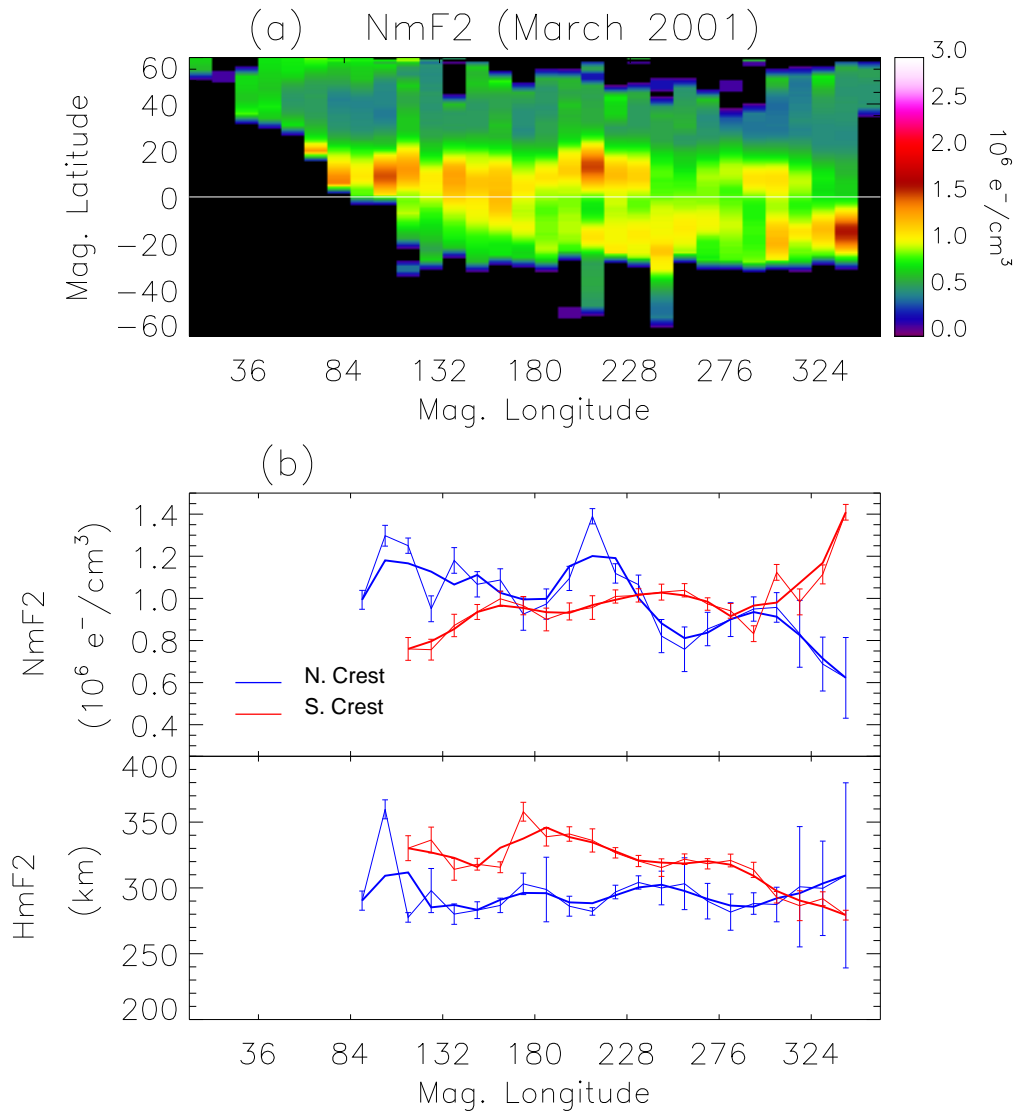
Figure 4-2 (a) LORAAS derived *NmF2* averaged over March 2001 (0230 LT). (b) *NmF2* and *hmF2* of the northern (blue) and southern (red) anomaly peak region as a function of magnetic longitude. Longitudinally smoothed data are overplotted in order to emphasize the wavelike variation of the density and height of the anomaly crests.

149

Figure 4-2 and Figure 4-3 show the monthly averages of *NmF2* for March 2001 and March 2002, respectively, as a function of geomagnetic latitude and longitude. Also shown are the *NmF2* and *hmF2* of the northern and southern anomaly regions (averaged over 5° – 20° north and south magnetic latitude, respectively). Both years show remarkably similar longitudinal patterns. As shown above in Figure 4-2, the anomaly crests are generally closer together near 150° magnetic longitude than at other longitudes; and there is a similar hemispheric asymmetry in the longitudinal variation of the peak densities.
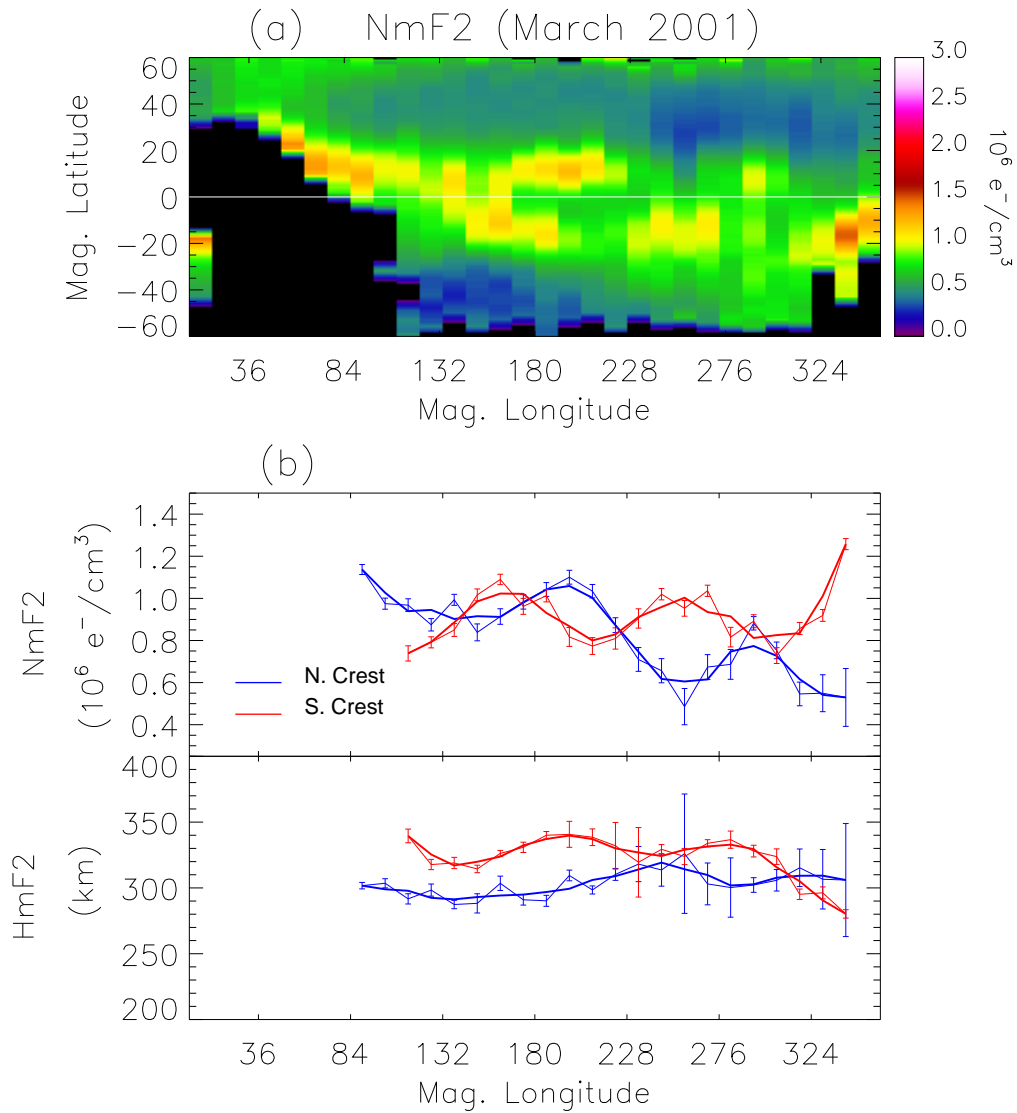
Figure 4-3 (a) LORAAS derived *NmF2*s averaged over March 2002. (b) *NmF2* and *hmF2* of the anomaly crest region as a function of magnetic longitude.

In both years, maxima in the northern anomaly *NmF2* are observed near 200° − 210° and

290° E. magnetic longitude (~126° − 138° and 220° E. geographic longitude) and

possibly near 90° – 100° E. magnetic longitude (18° – 30° E. geographic longitude). In the southern anomaly, maxima in *NmF2* are observed near 160°, 260° and 340° E. magnetic longitude (90°, 186°, and 270° E. geographic longitude). In both hemispheres, the maxima are separated by ~90° – 100°, with a ~60° offset in the longitude of the northern versus southern maxima. There is also a longitudinal variation in the *hmF2* that is roughly anticorrelated with the peaks in *NmF2*. We note that at most longitudes, the southern anomaly crests are ~30 – 40 km higher than the northern anomaly crests.

In Figure 4-4, we show the mean dip latitude of the northern and southern anomaly crests for March 2001 and March 2002, along with the 1σ standard deviation of the crest location from the mean. Here, the data for the two months are combined since the same pattern is present in both months. As observed in Figure 4-2(a) and Figure 4-3(a), there is a wavelike structure to the latitudes of the crests, with minima near 132° and 252° – 276° E. magnetic longitude and a maximum at 180°. The northern latitude maximum crest latitude at 180° and minimum latitude at 256° roughly correlate with a maximum and minimum, respectively, in the northern crest *NmF2*.
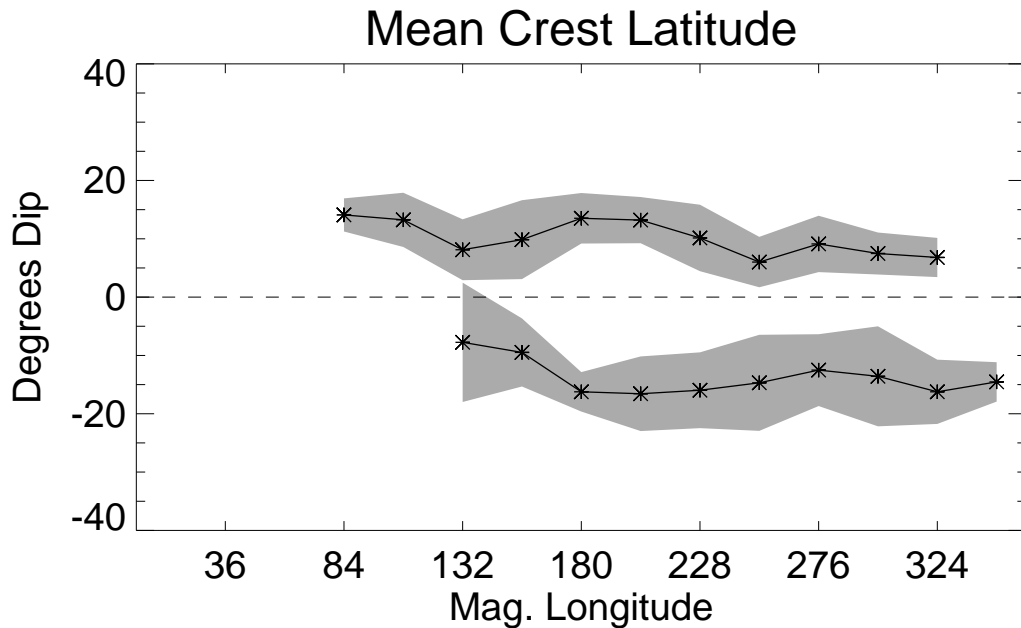
Figure 4-4 Mean dip latitude of the northern and southern anomaly crests for March 2001 and March 2002. The gray area shows the 1σ standard deviation of the crest location from the mean.

4.3 Model Comparisons

As discussed above in Section 4.1, the small-scale longitudinal variation in the equatorial anomaly region has been observed in various datasets other than LORAAS. If this variability is typically present during equinoxes, it is reasonable to expect to see similar structure in empirical models such as IRI-90. Figure 4-5 shows the IRI-90 results for March 2002. Inputs include the solar flux index ($F_{10.7}$) for 1-31 March 2002 as well as the tangent point latitude and longitude of the LORAAS measurement over this time period. The model results indicate that the *NmF2* of the anomaly region is consistent with but show less variation than the LORAAS results, with densities ranging from ~1×10^6 – 2×10^6 cm^{-3}. The *hmF2* of the IRI-90 results show that the southern anomaly is at a higher altitude than the northern anomaly in most longitude sectors, but again, there is less

variability. There is evidence of a wavelike longitudinal variation in the strength of the anomaly crests, especially in the southern anomaly, but there are more than four maxima. Maxima in the northern anomaly crests correlate with the southern maxima, which contrast with the LORAAS results.
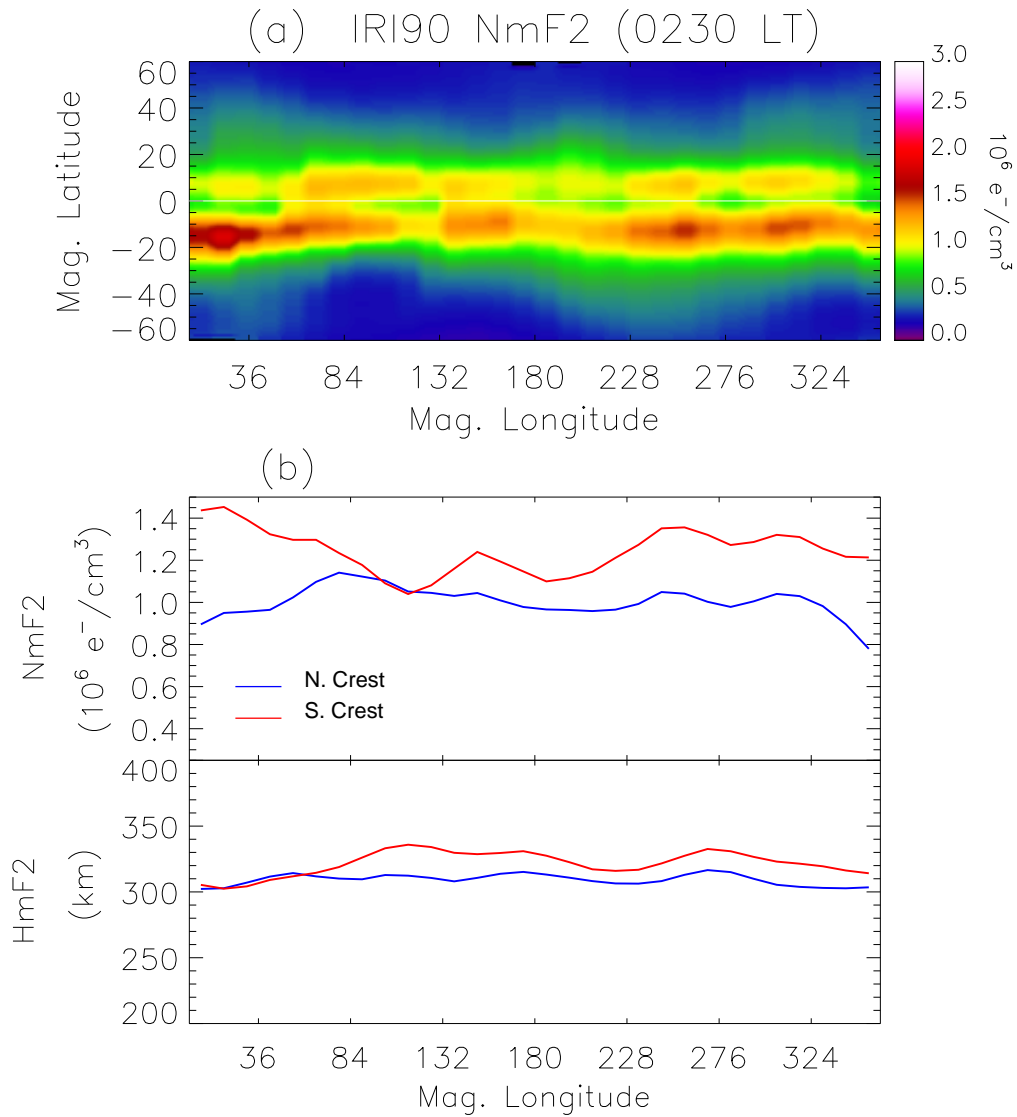
Figure 4-5 IRI *NmF2* using the geomagnetic conditions for 1-31 March 2002. Time and position input parameters are extracted from the LORAAS dataset.

To explore the role of the thermospheric neutral winds in the post-midnight

ionosphere, we used SAMI2 (cf. Section 1.9). Since wind model within SAMI2

(HWM93) includes longitudinal variations due to tidal effects, we were interested in determining if these variations were reflected in the ionospheric densities generated by SAMI2.

SAMI2 was run for 30 longitude sectors corresponding to the 12° LORAAS longitude bins for day 75 (March 16) with the average geomagnetic conditions for the 1–31 March 2002 time period (Ap = 10.4, $F_{10.7}$ = 178.4, 81-day average $F_{10.7}$ = 190.8). Figure 4-6 shows the composite SAMI2 peak densities at 0230 LT for all longitude sectors. These results are contrasted with the SAMI2 output earlier in the evening at 2000 LT (Figure 4-7). The dramatic difference between the 2000 LT and 0230 LT results is an indication that the evening neutral winds play a very large role in determining the observed densities at 0230 LT. The relatively high densities generated in the southern anomaly region in the Pacific sector are a result of strong northward meridional winds in the southern midlatitudes that persist until at least 0230 LT. A comparison of these results to IRI-90 and LORAAS shows that the HWM93 winds are not representative of the March 2001 and March 2002 conditions, especially in the southern Pacific. That the SAMI2 results do not match the observations very well is not unexpected, considering our poor knowledge of the neutral winds.
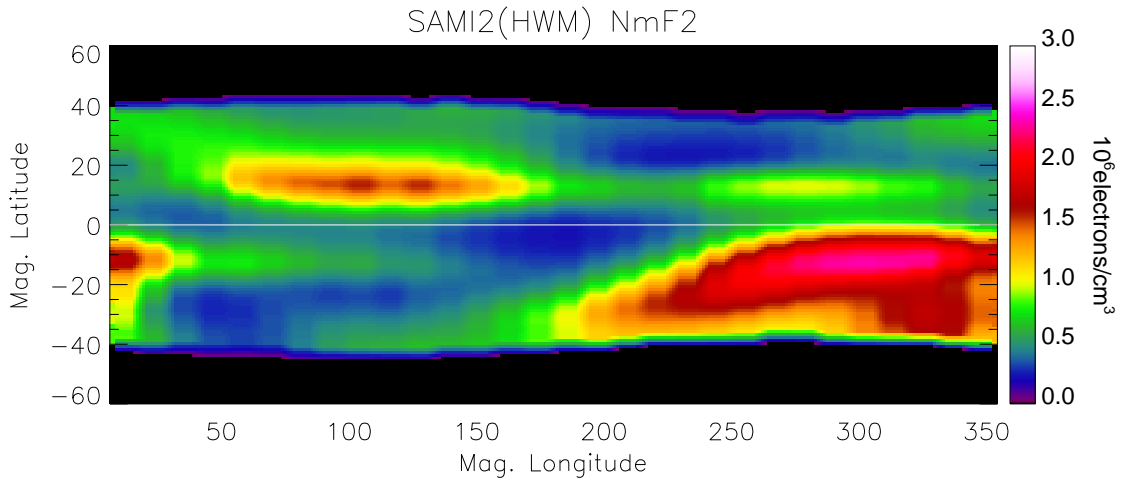
Figure 4-6 SAMI2 *NmF2*s at 0230 LT using the average geomagnetic conditions for March 2002. SAMI2 uses empirical models of the **E** × **B** drifts and neutral winds.
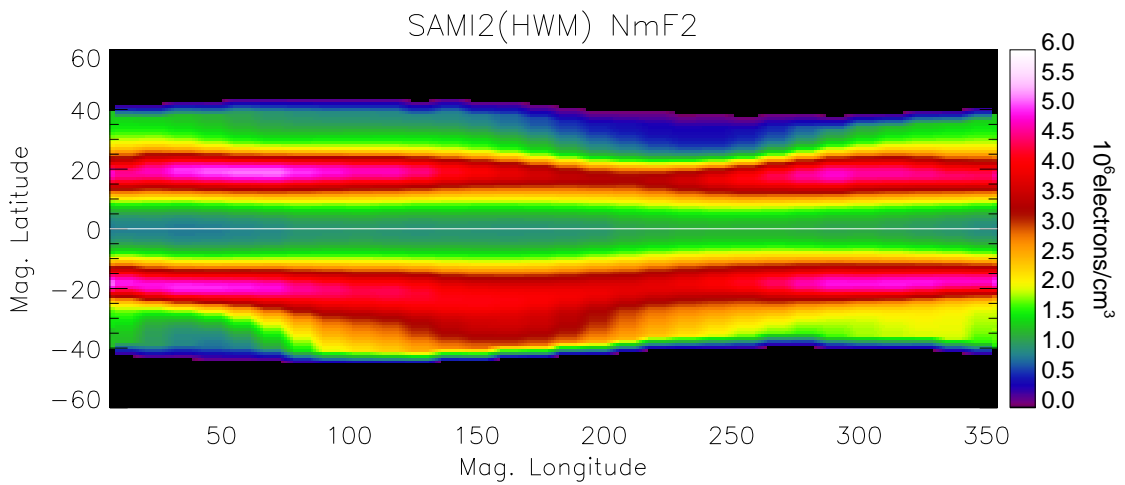
Figure 4-7 SAMI2 *NmF2*s at 2000 LT. The northern and southern anomaly features are much more symmetric about the magnetic equator early in the evening than later on.
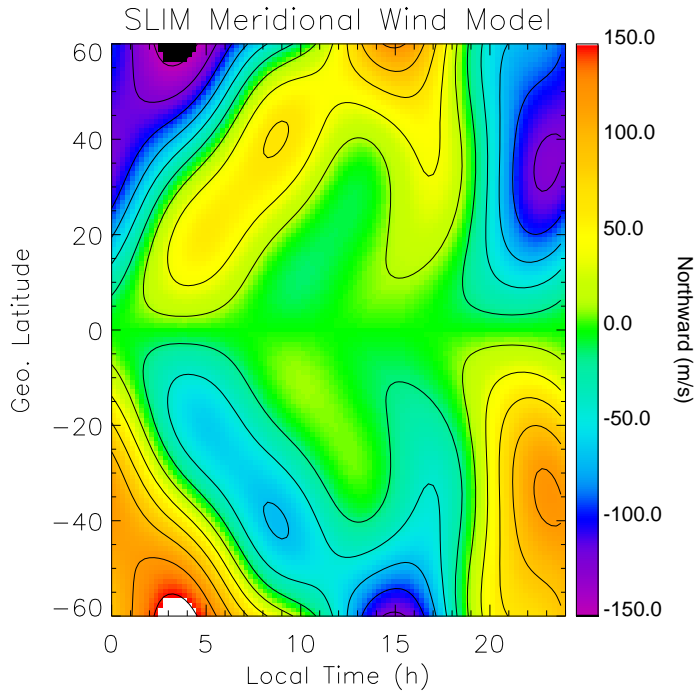
Figure 4-8 Analytic meridional wind model used within the semi-empirical low-latitude ionosphere model (SLIM) [*Anderson et al.,* 1987]. The equinox model is shown here.

We investigate the role of the winds in producing the observed densities by varying the winds within SAMI2 to match the asymmetry in the northern and southern anomaly crests. First, we describe in more detail how the winds affect the ionization. In general, the wind along the magnetic meridian is given by

$$W_M = W_N \cos \delta - W_E \sin \delta \qquad (4\text{-}1)$$

where δ is the magnetic declination and W_N and are W_E are the meridional (northward) wind and zonal (eastward) wind, respectively. The horizontal wind W_M can be resolved into a field-aligned component,

158

$$W_f = W_M \cos I \qquad\qquad (4\text{-}2)$$

and a component perpendicular to the field lines,

$$W_p = W_M \sin I \qquad\qquad (4\text{-}3)$$

where I is the magnetic dip angle. Since the plasma is confined to move along the field lines, W_p has no direct effect on the ionization. The vertical drift produced by the neutral wind can be described as an effective vertical wind

$$V = W_M \cos I \sin I . \qquad\qquad (4\text{-}4)$$

Winds near the magnetic equator, where $I = 0$, cause no change in the height of the ionization. A maximum effect occurs where $I = 45°$. Also, meridional winds are the main contributor, whereas zonal winds have a significant effect only for large δ (*cf.* equation 4-1). An upward effective vertical wind will push the plasma along the field lines to higher altitudes where recombination is slow. A downward effective wind will push the plasma to lower altitudes where there is a higher chemical loss rate such that the ionization decays more rapidly.

We replace HWM93 in SAMI2 with the analytic meridional wind model used within the semi-empirical low-latitude ionosphere model (SLIM) [*Anderson et al.*, 1987].

Figure 4-8 shows the longitudinal and altitude independent wind model that we employ. The model consists of a constant equatorward wind with diurnal, semi-diurnal and terdiurnal components. This wind model, however, does not include a zonal component. Thus, for this study we modulate the meridional wind W_N in order to obtain a field-aligned wind W_f that reproduces the observed electron densities. There are two reasons why the SLIM wind model was chosen over HWM93. First, the equinox version of this model is symmetric about the geographic equator, with winds tending to 0 m/s at the equator, which makes it easy to independently modulate the northern and southern winds by a multiplicative factor without introducing discontinuities in the wind field. Second, the SLIM wind model does not have exceptionally high southern midlatitude evening winds and therefore does not produce excessive southern midlatitude densities in the postmidnight ionosphere. Figure 4-9 shows the SAMI2 results when the SLIM wind model is used without modification. The hemispheric asymmetries are primarily due to the offset of the magnetic equator with respect to the geographic equator. For example, between 100° to 250° magnetic longitude, the southern anomaly lies closer to the geographic equator where meridional winds are minimal, whereas the northern anomaly lies in a region of stronger nighttime equatorward winds. The equatorward winds sustain the ionosphere in the northern anomaly crests while the southern anomaly nearly disappears. The reverse occurs in the longitudes where the magnetic equator falls in the southern hemisphere.

.
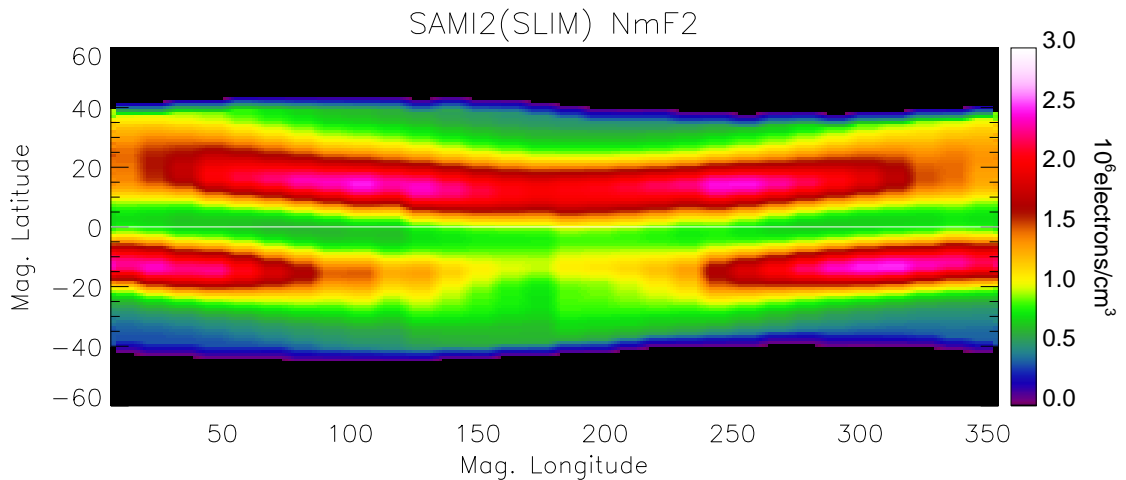
Figure 4-9 SAMI2 *NmF2* at 0230 LT using the SLIM wind model, as discussed in the text.

As illustrated in Figure 4-10, we modulate the meridional winds by multiplying the SLIM wind by a separate factor in each hemisphere. *N* is the multiplicative factor applied to the northern hemisphere, and *S* is the factor applied to the southern hemisphere. No wind (*S*=0, *N*=0) leads to a weak anomaly with symmetric crests on either side of the magnetic equator. Application of the unmodified SLIM wind (*S*=1, *N*=1) leads to a strong northern anomaly crest and weaker southern crest due to an offset of the geographic equator by nearly 9° south of the magnetic equator. Because of this offset, a 50% reduction in the northern winds (*S*=1, *N*=0.5) reduces the density in both anomaly crests; whereas a reduction in the southern winds (*S*=0.5, *N*=1) primarily affects the southern anomaly crest. We note that even small differences in meridional wind speeds (on the order of 5-10 m/s) acting over several hours can have a significant impact

161

on the ionospheric densities at 0230 LT. In this particular example, a 50% reduction of the wind speed (S=0.5, N=0.5) leads to a 30% reduction in the southern anomaly crest.

With this simple parameterization of the SLIM winds, we can adjust N and S to bring the peaks of the northern and southern anomaly crests into better agreement with the LORAAS observations. We emphasize that in this study we only attempt to match the densities of the anomaly crest peaks and not the entire latitudinal profile. We also do not attempt to match the latitudinal positions of the anomaly crests, which would require adjustments to the $\mathbf{E} \times \mathbf{B}$ drifts within the model. Our approach to modulating the winds is not a method for extracting the true winds; rather it provides a means to qualitatively explore the longitudinal differences in the wind patterns that drive the density asymmetries.
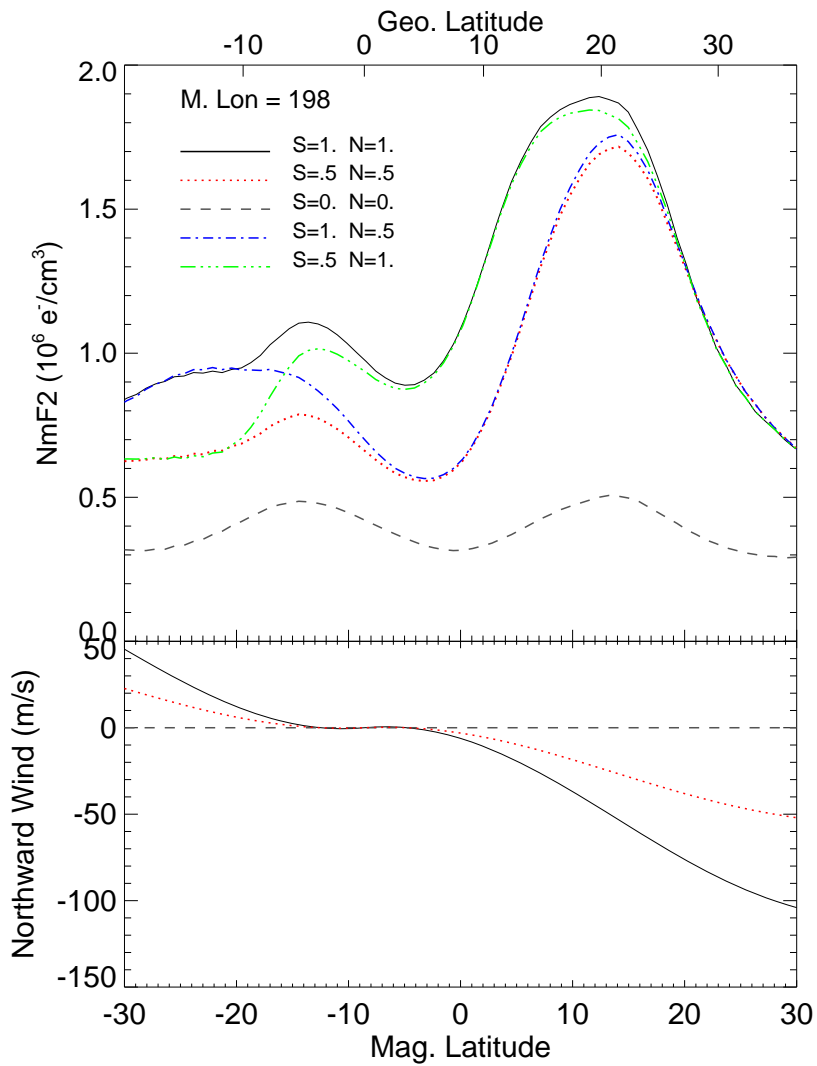
Figure 4-10 SAMI2-SLIM *NmF2* profiles at 0230 LT for several combinations of north/south wind modulation factors and the average evening wind profiles. N is the multiplicative factor applied to the northern hemisphere winds in SLIM, and S is the factor for the southern hemisphere winds.

Figure 4-11 shows comparisons between LORAAS densities and those obtained

with SAMI2-SLIM. The model results for both the unmodified (*S*=1, *N*=1) winds and

modulated winds are shown. *NmF2*s are shown for the four magnetic longitudes (198°,

258°, 294° and 342° E) that correspond to the observed longitudinal peaks in the LORAAS results for March 2002. We first discuss the LORAAS densities then compare them to the model results.

The LORAAS data show stronger northern anomaly crests at 198° and 294°, whereas the southern crests are stronger at 258° and 342°. To first order, the meridional winds blow equatorward in the night and are stronger in magnitude at higher latitudes (see Figure 4-8). Anomalies that form at higher geographic latitudes typically decay more slowly than those that develop closer to the geographic equator because the effective vertical wind due to higher horizontal winds and higher inclination angles at these latitudes maintain the plasma at altitudes where recombination is slow. This argument can explain the observed densities at 198°, where the northern crest is stronger than the southern crest, and at 342° where the southern crest is quite strong and the northern crest has vanished. At 258° and 294°, where the dip equator is near the geographic equator and the declination is similar in both longitudes (~10°), the orientation of the magnetic field cannot explain the different asymmetries observed in these two locations. Thus, we suspect that longitudinal variations in the neutral wind field are the cause of the asymmetry.

At each of the four longitudes, we modulate the SLIM wind by a northern (N) and southern (S) factor for the winds north and south of the geographic equator. The factors used in each case are displayed at the bottom of each image in Figure 4-11. At 198°, the

unmodified SAMI2-SLIM model does produce a larger northern than southern crest, but the densities are brought into better agreement with LORAAS when the northern wind is scaled by a factor of 0.28 and the southern wind is scaled by 0.90. Here, the southern hemisphere wind has a minimal effect because the southern anomaly is near the geographic equator. At 258°, the SAMI2-SLIM model shows a different asymmetry than observed by LORAAS. In order to reduce the density of the southern anomaly crest, the wind is scaled by a factor of 0.36; the northern hemisphere wind must be reduced in strength and reversed in direction so that the field-aligned evening winds are blowing poleward in order to promote decay of the northern anomaly crest. The asymmetry of the SAMI2-SLIM densities at 294° is also opposite that of LORAAS. In this case the southern hemisphere wind is reduced in strength slightly more than the northern hemisphere wind. At 342°, the SAMI2-SLIM model shows a considerable northern anomaly. To decrease the density in this region, the northern hemisphere wind is reduced in strength and reversed in direction; the southern wind is scaled by a factor of 0.54. At all longitudes, we are able to match the densities of the anomaly crest peaks quite well, but the LORAAS densities in the trough region between the crests are generally much higher than the model. This is due to the smoothing introduced by the 2-D inversion algorithm as well as smoothing due to averaging over a month of data.

Our data-model comparisons show that the northern hemisphere field-aligned wind alternates between blowing equatorward when there is a maximum in the northern anomaly crest and poleward when there is a maximum in the southern anomaly crest. Of

165

course, this does not mean that the winds are always blowing in these directions, but that this is on average what is happening during the evening hours when the winds have the most direct influence on the densities in the equatorial anomaly. Since we are effectively modulating the field-aligned wind within SAMI2 to match the observations, we cannot separate the relative contributions of the zonal versus meridional components of the wind. It is likely that longitudinal structure in both the zonal and meridional winds contribute to the observed density asymmetries and the maintenance of the wavelike pattern in both hemispheres. Indeed, recent observations of zonal winds at the magnetic equator using the CHAMP (CHAllenging Minisatellite Payload) accelerometer do exhibit a wave-4 pattern [*Häusler et al.*, 2007].
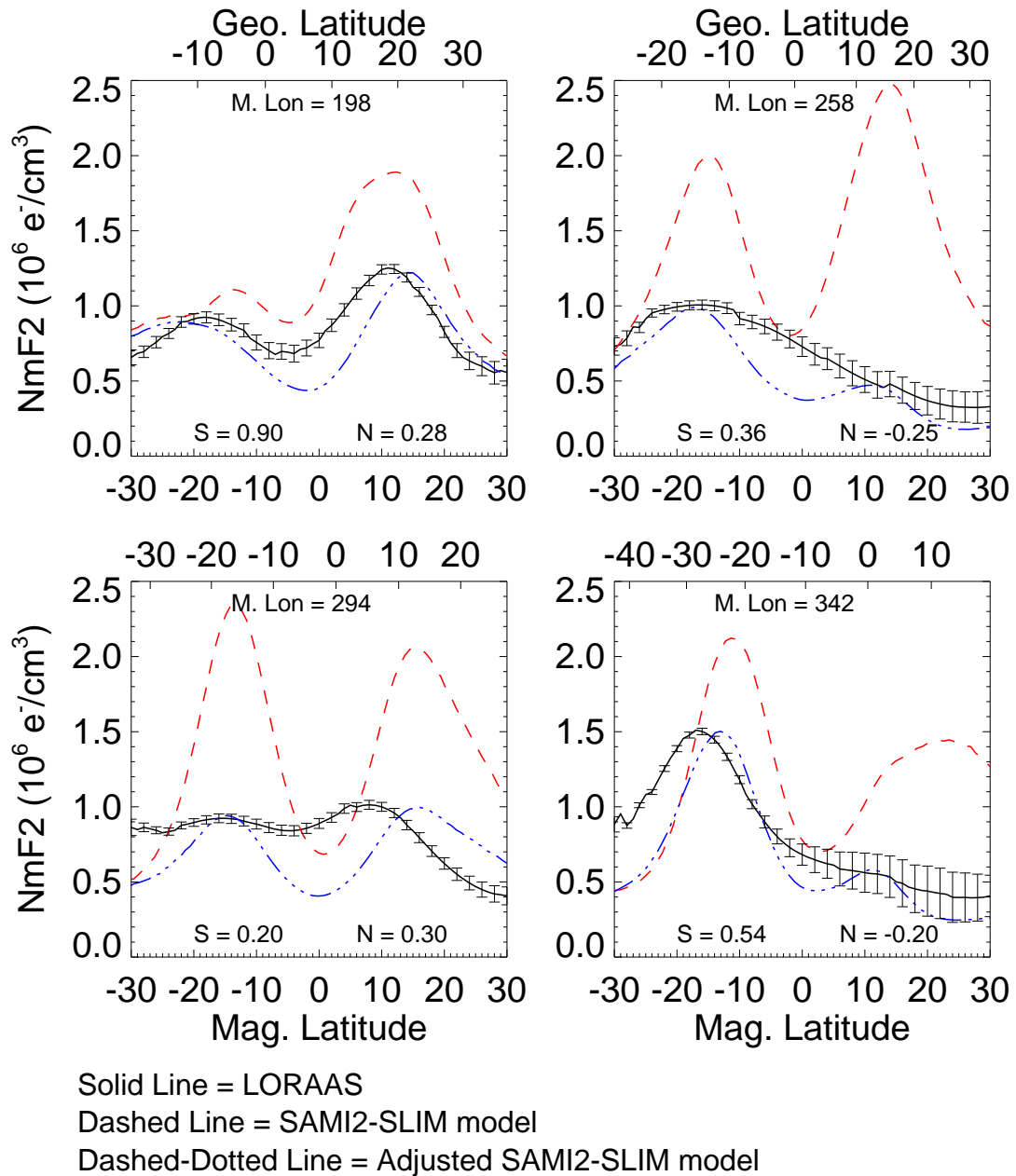
Figure 4-11 Latitudinal profiles of *NmF2* at four longitudes corresponding to longitudinal maxima in the anomaly crests. The LORAAS profiles are in black (solid line), the SAMI2 model with the unmodified SLIM winds are in red (dashed line), and the SAMI2 model with modulated SLIM winds are in blue (dashed-dotted line). Geographic latitude is shown in the upper x-axis and magnetic latitude is shown in the lower x-axis. Also shown are the N and S multiplicative factors applied to the SLIM model in each case.

4.4 Discussion

The LORAAS results for March 2001 and March 2002 show a wavelike (wave-4) pattern in the longitudinal variation of *NmF2* in the equatorial anomaly region. We have found that the northern anomaly has maxima near 18° – 30°, 126° – 138°, and 223° E geographic longitude. The locations of the maxima in the *NmF2* in the northern anomaly agree quite well with previous observations, which are in general agreement that the maxima are relatively fixed at 10° – 30°, 100° – 120°, 180° – 230°, and 260° – 280° E [*Deminova*, 2003; *Ivers et al.*, 2003; *Jadhav et al.*, 2003; *Sagawa et al.*, 2005; *Immel et al.*, 2006; *England et al.*, 2006]. We compared our results with the IMAGE/FUV observations of the 135.6 nm emission feature during April 2002 at ~2030 LT [*Immel et al.*, 2006; *England et al.*, 2006] and found that the LORAAS maxima at 0230 LT were generally 10° – 20° eastward. This finding is consistent with a 2° to 4° per hour eastward plasma drift of the longitude structures, which is consistent with low latitude plasma drift speeds measured by FUV [*Immel et al.*, 2003].

The LORAAS data additionally show there is a similar longitudinal variation in the densities of the southern anomaly crests. However, the locations of these maxima are offset ~60° eastward of the northern anomaly maxima. Though *Immel et al.* [2006] does not discuss the southern anomaly, *England et al.* [2006] in their reanalysis of the IMAGE/FUV and GUVI data from March-April 2002 do mention that the wave-4 pattern is observed in the magnetic latitude of the southern anomaly crest of the GUVI data but not in the brightness. (GUVI results for both hemispheres are presented by *Henderson et*

al. [2005].) Though the GUVI and LORAAS data are both from spring equinox 2002, they are separated ~5 hours in local time. That a pattern is not observed in the brightness of the southern anomaly crests earlier in the evening may indicate that the meridional winds were already dominating and shifting the longitudinal density structure in the southern latitudes.

It is interesting that the longitudinal variation in the anomaly region is consistent in two different years, suggesting a stationary or seasonal longitudinal pattern in the *F* region meridional winds, although clearly more studies are needed to confirm this. Recently, *Emmert* [2001] studied the global climatology of the *F* region winds using extensive measurements by the Wind Imaging Interferometer (WINDII) instrument on board the Upper Atmospheric Research Satellite (UARS) and found that the meridional winds are more northward in the American sector at night. Our results at 342° magnetic longitude are in agreement with this finding. We also find that the field-aligned wind is northward near 258°, which may indicate northward meridional winds at this longitude, however this is not observed in the WINDII data. Differences may be attributed to the fact that the WINDII longitudinal study used over 60° longitude bins, which smoothes out smaller scale features, and that the majority of the WINDII data used in the study were collected during quieter conditions (average $F_{10.7} = 120$) than solar maximum conditions of the LORAAS observations.

We observed a wavelike pattern in the anomaly crest latitude, with some evidence

of a correlation between the crest latitude and northern anomaly densities, though the

correlation is not as strong as observed by *Immel et al*. [2006]. The same pattern is

observed in both March 2001 and March 2002. That there is a correlation with the

northern, and not the southern, anomaly crest densities is consistent with our findings that

the neutral winds have altered the longitudinal pattern of the southern anomaly. The fact

that the correlation is not particularly strong indicates that the *F* region processes that

dominate in the nighttime ionosphere have altered the anomaly latitudes.

4.5 Summary

We have used electron densities derived from the O I 135.6 nm emissions in the

nighttime *F* region ionosphere observed by the LORAAS limb scanning instrument to

show longitudinal variation in the anomaly crests in both hemispheres during March 2001

and March 2002. The locations of the northern anomaly maxima correspond well with

previous observations. The LORAAS instrument was contaminated with noise in the

American-African sector and therefore only detected three maxima in the densities;

however our results do not contradict the possibility of a wave-4 variation. Our results

show that the *F* region winds, the dominant force affecting the plasma distribution in the

post midnight equatorial ionosphere, have not altered the longitudinal features observed

by IMAGE FUV at an earlier local time; in fact, the winds have enhanced these

seemingly stationary features. Interestingly, the LORAAS data reveal an asymmetry in

the locations of the maxima in the southern hemisphere with respect to the northern

hemisphere. Again, three maxima are detected but are offset from the northern maxima by ~60°. We have shown that the asymmetries are a result of a combination of the offset of the geomagnetic field with respect to the geographic equator and longitudinal variability of the meridional winds. We have also observed a wavelike pattern in the longitudinal variation of the anomaly crest latitude that roughly correlates with the northern anomaly densities. A comparison of our results with that of *Immel et al.* [2006] during the same month and year but at an earlier local time, show that during equinox the postmidnight northern anomaly densities show a close connection with processes that dominate in the daytime and early evening hours. *F* region processes dominate the longitudinal pattern observed in the anomaly latitudes and the southern anomaly densities.

We have compared our results with an empirical model, IRI-90, and have found a wavelike structure in the peak densities of the IRI-90 anomaly crests, especially in the southern anomaly. The peaks appear at the same longitudes in both hemispheres, in contrast to the observed asymmetries of the LORAAS results. IRI-90 also displays five peaks, rather than the wave-4 pattern present in the March 2002 observations.

In an attempt to understand the behavior of the neutral winds and their impact on the post-midnight densities, we performed model runs using SAMI2. SAMI2 was run using HWM93 and found to compare poorly with the LORAAS densities. It was found that even small differences in meridional wind speeds (on the order of $10 - 20$ m/s) acting

171

over several hours have a significant impact on the ionospheric densities at 0230 LT. We then replaced HWM93 with the SLIM analytic model of the neutral winds and modulated the northern and southern components of this wind to match the SAMI2 densities to the LORAAS observations. We found that the field-aligned winds vary with longitude with the northern hemisphere evening winds alternating between equatorward and northward. Our results indicate that the *F* region winds help preserve the wave-4 pattern in the anomaly densities well into the evening, especially in the northern crests. The fact that the wave-4 pattern is visible in many different satellite observations of the densities (or brightnesses) of the anomaly crests could be due to both daytime lower atmosphere effects (as discussed by *Immel et al.* [2006] and *Sagawa et al.* [2005]) as well as *F* region processes. This study also highlights the importance in understanding the longitudinal behavior of the thermospheric winds. Clearly, more wind measurements are needed, especially if we are to gain a better understanding of the observed densities in the evening hours when the winds begin to dominate the ionospheric morphology. Future work will involve employing a model, such as SAMI3, which includes a more accurate representation of the Earth's magnetic field, along with a wind model with both zonal and meridional components, to obtain a better understanding of the relative contributions of each of the wind components.

5 Conclusions

One of the motivations for studying the ionosphere is that many of our current space-borne and ground-based technological systems used for communication, navigation, surveillance and research are susceptible to ionospheric weather. Geomagnetic storms are particularly disruptive and resultant satellite system failures can be quite significant. But even quiet-time disturbances such as scintillation and spread-F events can wreak havoc on high frequency radio communications, especially in equatorial regions. In order to develop better prediction capabilities, we must obtain a better understanding of the drivers of the observed variability. And to identify drivers, it is important to accurately characterize the observed variability. The purpose of this study has been to use recent ionospheric measurements, particularly UV radiances, along with recently developed analysis techniques to better characterize the day to day and longitudinal variability of the low-latitude ionosphere. Such global observations provide much needed data to help validate existing ionospheric models and contribute to the development of ionospheric weather prediction techniques.

5.1 Summary of Results

5.1.1   Variability in the Occurrence of Scintillation

In Chapter 2, we investigated the variability of the occurrence of scintillation in two longitude sectors. Within a 24 hour period, strong scintillation was observed in one region, but no scintillation was recorded in the other, despite identical geomagnetic conditions. We showed that the combination of several different datasets along with a data assimilation model can serve as a powerful tool for investigating the global time evolution of the large scale structure of the ionosphere. We were able to verify that strong scintillation is associated with large ionospheric depletions (bubbles). Our analysis of the two longitude sectors showed that there were significant differences in the evolution of the *TEC* distributions from 1800 LT to 2400 LT, which were likely the result of differences in the daytime and post-sunset vertical plasma drifts in the two sectors. Previous studies showed that such differences in plasma distributions are observed on a day to day basis in a single longitude sector [e.g. *Valladares et al.*, 2001]. Our study showed that similar differences are observed in different longitude sectors on the same day.

Though this study did not clearly indicate why scintillation was not observed in the Far-East Asian sector, it did highlight the fact that studies limited to the characterization of large-scale plasma distributions may not be sufficient to uncover the physical processes underlying the development or suppression of scintillation on a given

174

day. Investigations that involve the study of smaller scale ionospheric and thermospheric variations are needed. Possible seeding and suppression mechanisms need to be explored.

An additional outcome of this study was that it was the first to test the capabilities of GAIM as a scientific tool. It was found that GAIM performs quite well in regions where there is significant measurement data to be assimilated. However, at the time of this study, the GAIM preprocessors did not have the ability to appropriately handle data that contain depletions due to bubbles. Clearly, this deficiency must be addressed before GAIM can be truly useful. Also, as expected, GAIM does not perform well in regions with little or no data.

5.1.2   Day to Day Variability of the Equatorial Anomaly

Next, we continued to investigate the large-scale characteristics of the low latitude region under geomagnetically quiet conditions. In particular, we looked at the equatorial anomaly feature, a prominent feature of the nighttime ionosphere. To do this, we used UV limb scans from the LORAAS instrument that flew aboard ARGOS from 1999 to 2002. LORAAS was the first of a new generation of limb scanning instruments that are flying aboard the current DMSP satellite block. We used a new 2-D technique [*Dymond et al.*, 2001] for inverting the O I 135.6 nm radiances to obtain electron density profiles and altitude-latitude maps of the low-latitude nighttime ionosphere.

We compared the LORAAS derived densities with ionosonde measurements of *NmF2* and found good agreement, especially when the LORAAS measurements were within 3° latitude and 5° longitude of the ionosonde. Comparisons with GUVI densities, derived with the 1-D inversion algorithm, showed the latitudes and altitudes of the anomaly crests matched fairly well. The average difference between the GUVI and LORAAS *NmF2s* was less than 20%. We found that the geometry of the LORAAS limb scans made it difficult to extract accurate densities in the trough region between the anomaly crests. Additionally, the regularization parameter may overly smooth the densities in some cases, leading to lower densities in the anomaly crests and higher densities in the region between the crests. Despite the limitations of the 2-D inversion technique, it provides a fairly accurate representation of the morphology of the equatorial anomaly.

Using two months of LORAAS data (March 2001 and March 2002), we characterized the day to day variability of several parameters of the *F* region ionosphere that are associated with the equatorial anomaly. Specifically, we looked at the latitudinal separation, dip latitude, peak electron density (*NmF2*), peak height (*hmF2*), north/south ratio of *NmF2*, and the widths of the northern and southern anomaly crests as a function of longitude. Though there have been many studies of *NmF2*, this is one of a few that investigate the global day to day variability of the height of the ionospheric peak over an extended period of time. A comparison of the monthly mean and 1σ standard deviation of each of the anomaly parameters revealed that the most variable aspects of the anomaly

crests is their latitude and separation, with the RSD varying between 46 – 67%. The least variable parameter is the *hmF2*, where the RSD was found to be 7 – 9%. The *NmF2*s and widths of the crests varied from 27 – 32%, which is consistent with previous studies [e.g. *Forbes et al.*, 2000; *Rishbeth and Mendillo*, 2001; *Bilitza et al.*, 2004]. A comparison of the northern and southern anomaly crests showed that, on average, the densities are about the same, but that the northern crest is lower in altitude than the southern crest.

Comparisons with a climatological model of the ionosphere (IRI-90) showed that while the model showed no significant variations in parameters from day to day or with longitude, the model results fell within the 1σ standard deviation of the LORAAS data in most longitude sectors. Longitudinal trends in the LORAAS data generally did not match that of the IRI-90 results.

No correlation was found between parameters in any particular longitude sector versus another on a given day. We attributed this finding to the possibility that the scale lengths of the drivers (i.e. winds) of the low-latitude electron density distributions are smaller than the longitudinal bin size of 24°. Correlation between the anomaly parameters and solar flux or geomagnetic activity was not found, due to the significant day to day variation from other effects.

We have demonstrated that the 2-D inversion technique for obtaining electron densities from UV limb scans is capable of characterizing important large-scale features of the ionosphere, such as *NmF2* and *hmF2*.

5.1.3   Longitudinal Variability of the Equatorial Anomaly

In Chapter 3, it was discovered that there was a wavelike variation in the separation of the anomaly crests, with the anomaly crests generally closer together in the 60° – 84° and 180° longitude sectors and farther apart elsewhere. In Chapter 4, we used the LORAAS data to investigate in more detail the longitudinal variation of the anomaly crests in March 2001 and March 2002.

Three maxima in the anomaly region densities were found, both in the northern and southern hemispheres. The longitudinal separation of the maxima suggested a wave-4 variation, which is consistent with a recent study by *Immel et al*. [2006]. But unlike previous studies of longitudinal variability, a pronounced hemispheric asymmetry in the location of the maxima was found. The source of this asymmetry was investigated and we showed that it could be explained by longitudinal variations in the thermospheric neutral winds.

5.2 Limitations

5.2.1   LORAAS Inversion Algorithm

In our analysis of the LORAAS UV limb data, we made use of a 2-D algorithm to invert the line of sight radiances to vertical electron density profiles. Though we found that this technique was adequate for the purposes of our work, there are several improvements that can be made to the algorithm. For example, it should be possible to reduce the model grid size so that better than 5° latitude resolution is achieved. We have performed some initial work in this area and have found that reducing the grid size by a factor of two improves the resolution of the anomaly crest and trough region. Another way to improve the reconstruction is to use a more sophisticated interpolation scheme within the algorithm. We have successfully done this, but the improved interpolation algorithm significantly impacts the speed of the inversions.

Another area that requires additional investigation is the choice of regularization. This is an active area of study in engineering, physics and applied mathematics where solutions of the Fredholm equation of the 1st kind are important. Tikhonov regularization, which we employ, is the most common method in use, but optimal selection of the regularization parameter is still an unsolved problem. As described in the Appendix, some smoothing is required in order to find the best solution to the inverse problem, however there is a bit of an art to choosing the correct implementation of this smoothing. We chose to use the "L" curve technique and sampled several inversions in order to find the optimal regularization parameter. A single regularization parameter, applied to all

data over a month, rather than each inversion, does tend to overly smooth some of the data. We also found that even though a regularization parameter may be optimal as determined by the "L" curve technique for a specific dataset, it may still overly smooth the inversion.

Also, additional validation of the derived electron density profiles is required in order to determine whether or not a Chapman profile is a reasonable assumption. In our work, we have not investigated how well the topside ionosphere is reproduced.

5.2.2   LORAAS Observations

Considerable noise in the LORAAS dataset limited the number of electron density profiles available for analysis. Noise due to energetic particles in the South Atlantic Anomaly region severely limited our ability to analyze the equatorial anomaly in the American and African longitude sectors.

In Chapters 3 and 4, our studies have been limited to the postmidnight, 0230 LT, time sector. By this time, we are observing the integrated effect of the various processes that control the ionospheric densities. Without additional information at earlier times, it is not possible to extract the relative contributions of the various drivers. For example, both the $\mathbf{E} \times \mathbf{B}$ drifts and thermospheric winds play a role in the maintenance, or depletion, of the equatorial anomaly. This limits our ability to interpret the observations.

5.3 Suggestions for Future Research

We have looked at LORAAS data from March 2001 and March 2002. At the time of this work, this is what was available to us. However, LORAAS collected data from November 1999 through March 2002, though it is not clear if or when this data will become available. Ideally, electron densities should be reconstructed for the entire mission, which would allow for seasonal studies that could be compared with the equinox results shown here. The effect that thermospheric winds have on the evening plasma distributions is known to vary considerably with season. Asymmetries in the northern and southern anomaly crests are enhanced during the solstices. Though *Immel et al.* [2006] did not observe a wave-4 variation at times other than near the equinoxes, others have observed nearly fixed maxima in all seasons [*Deminova*, 2003]. Additional analysis of the complete set of LORAAS observations would improve our understanding of the source of the observed variations.

We have not explored the dayside ionosphere that was also observed by LORAAS in the 1430 LT time sector. Comparisons of the daytime equatorial anomaly with the nighttime observations could provide insight into the degree to which the daytime upward $\mathbf{E} \times \mathbf{B}$ drifts affect the postmidnight distributions. Additionally, longitudinal variations in the dayside ionosphere should also be investigated and compared with nighttime results. These daytime observations would help determine if the longitudinal structure is set up by daytime processes.

Clearly, thermospheric neutral winds play a large role in the day to day and longitudinal variability observed in the LORAAS data. We have shown with model studies using SAMI2 that relatively small differences in wind speeds (on the order of 10 m/s) can have a large effect on ionospheric density distributions. But there is limited knowledge of the neutral winds. Current models, such as HWM93, are inadequate. For example, in Chapter 4 we have shown that HWM93 cannot reproduce the observed electron densities at 0230LT. More wind measurements are needed in order to develop improved empirical models of the global wind field that can be used as inputs in ionospheric models such as SAMI2 and SAMI3. With improved wind models, the dynamical effects of neutral winds on the F region distributions can be better explored. For example, the longitudinal variability of winds needs further investigation. We used SAMI2 along with different wind models to investigate the longitudinal variability of the field-aligned neutral winds. Additional studies using SAMI3, which includes a better magnetic field model, along with improved global models of zonal and meridional winds may provide additional insight into the consequences of wind variability.

Appendix: Regularization

The inverse problem

$$I = \alpha_{135.6} \int n_e n_{O^+} \, ds \qquad \text{(A-1)}$$

is a Fredholm equation of the 1st kind, which can be expressed as

$$\int_a^b K(s,t) f(t) dt = g(s) \qquad \text{(A-2)}$$

where $K(s,t)$ is a known kernel function, $g(s)$ is a known function, and $f(t)$ is the unknown to be solved. In our case, $g(s)$ is the line of sight radiances measured by the LORAAS instrument and the $f(t)$ is the product of the electron and O^+ densities.

Fredholm equations of the 1st kind with smooth kernels are inherently ill-posed problems; this means that the solution is extremely sensitive to perturbations in the input data, which can arise from random experimental or measurement errors. The reason for the sensitivity is that integration is a smoothing process, so its inverse is just the opposite [Heath, 1997]. Solving for $f(t)$ tends to introduce high-frequency oscillations in the result. In such problems, regularization is often used as a technique to filter out the high

frequency components associated with singular values. This is a reasonable approach because we are seeking a smooth solution. In particular, we make use of the regularization method proposed by *Tikhonov and Arsenin* [1977] and, independently, by *Phillips* [1962]. It is popularly referred to as the Tikhonov method.

Discretization of Equation (A-2) leads to the linear, discrete ill-posed problem of the form

$$\min_{x} \| Ax - b \|_2 \qquad\qquad\qquad (A\text{-}3)$$

where A is a matrix, b consists of the measurements, and x are the unknowns.

The Tikhonov method defines the regularized solution x_λ as the solution to the following problem

$$\min \left\{ \| Ax - b \|_2^2 + \lambda^2 \| L(x - x_0) \|_2^2 \right\}. \qquad\qquad (A\text{-}4)$$

L is the regularization operator chosen to obtain a solution with desirable properties, such as a small norm ($L = I$) or good smoothness (where L is a discrete approximation to a derivative operator), and $\lambda > 0$ is a scalar parameter. The central question in Tikhonov regularization is how to choose the parameter λ in order to produce a solution x_λ close to the true solution x [*O'Leary*, 2001]. The goal is to obtain as much information as possible

from our measurements, *b*. Too much regularization will overly smooth the solution by

leaving out information available in *b*; too little regularization will produce a solution

dominated by errors [*Hansen, 1992*].

To determine the regularization parameter, we will adopt the L-curve approach

proposed by *Hansen* [1992]. The L-curve is a plot of the side constraint ||L(x-x₀)||₂ versus

the residual norm ||Ax-b||₂. In the case of Tikhonov regularization, the L-curve is a

parameterized curve whose parameter is λ. In many problems, the resultant plot looks

somewhat like an L-shape. The corner of the "L" represents the optimal regularization

parameter because it balances the minimization of the residual norm with the

minimization of the side constraint. In other words, it is the parameter that will lead the

solution that is closest to the true solution without overly smoothing the result.

Now, we will show how regularization is applied to our problem defined in

Equation (A-1). As discussed in Section 3.2, we use an iterative Levenberg-Marquardt

scheme to minimize the Chi-squared statistic. Regularization was implemented by adding

a "roughness" norm (side-constraint) to the conventional chi-square as follows:

$$\chi_i^2 = \sum_j [(y_j - m_j^i)/\sigma_j]^2 + \lambda^2 \sum_k L^2(d_k^i), \qquad \text{(A-5)}$$

where y_j are the measurements, m_j^i is the fit at the *i*th iteration, σ_j is the measurement

uncertainty, d_k^i is the density at the *i*th iteration, λ is the regularization parameter, and *L* is

185

the regularization operator [*Dymond and Thomas*, 2001]. We use the percent difference

between the density at the ith iteration and a 3×3 boxcar average of the density as the

regularization operator. Note that one regularization parameter is used for the three

Chapman parameters (*NmF2*, *hmF2* and O^+ Scale Height). It is possible that better results

can be achieved if each of the parameters is given its own regularization parameter.

Choosing the optimal regularization parameter for each inversion requires

significant computation time. In order to efficiently process months of LORAAS data, it

is preferable to choose a fixed regularization parameter that works well for the majority

of the data. The optimal regularization parameter was chosen by plotting the L-curves for

six randomly chosen datasets, where λ^2 ranged from 10 to 1000 (Figure A-1). The

specific values of λ^2 are: 10, 20, 30, 40, 50, 60, 70, 80, 90, 100, 120, 140, 160, 180, 200,

250, 300, 600, and 1000. In four of the six cases, the corner of the "L" was found at $\lambda^2 =$

120. Fortunately, for our inverse problem a wide range of regularization parameters

produces nearly identical results. For example, Figure A-2 shows a LORAAS electron

density reconstruction without regularization ($\lambda^2 = 0$), with near-optimal regularization

($\lambda^2 = 90$), with optimal regularization ($\lambda^2 = 120$), and with over-regularization ($\lambda^2 =$

1000). Note that the regularization parameters 90 and 120 produce very similar results,

especially in the anomaly region. Figure A-3 shows the peak densities (*NmF2*) and peak

heights (*hmF2*) for these regularization parameters. Again, we compare the values

obtained for $\lambda^2 = 90$ and 120.

This study shows that regularization is required in order to solve the inverse problem given in Equation (A-1). Fortunately, in most cases our solution is not overly sensitive to the choice of the regularization parameter. We have selected six random LORAAS nightside passes to provide us with an "optimal" value for the regularization, and have found that $\lambda^2 = 120$ works well for March 2002. We have also selected LORAAS passes from March 2001 in order to determine that $\lambda^2 = 120$ is optimal for this month as well. However, we have also found that in some cases the optimal regularization weight overly smoothes the densities. For example, Figure A-4 shows the L-curve for March 11, 2002 at 79° longitude. The regularization weight of $\lambda^2 = 120$ falls near the corner of the L-curve, however the equatorial anomaly features are smoothed out, as shown in Figure A-5(a). Figure A-5(b) shows that the northern and southern anomaly crests are more distinct when a smaller regularization weight ($\lambda^2 = 60$) is used.
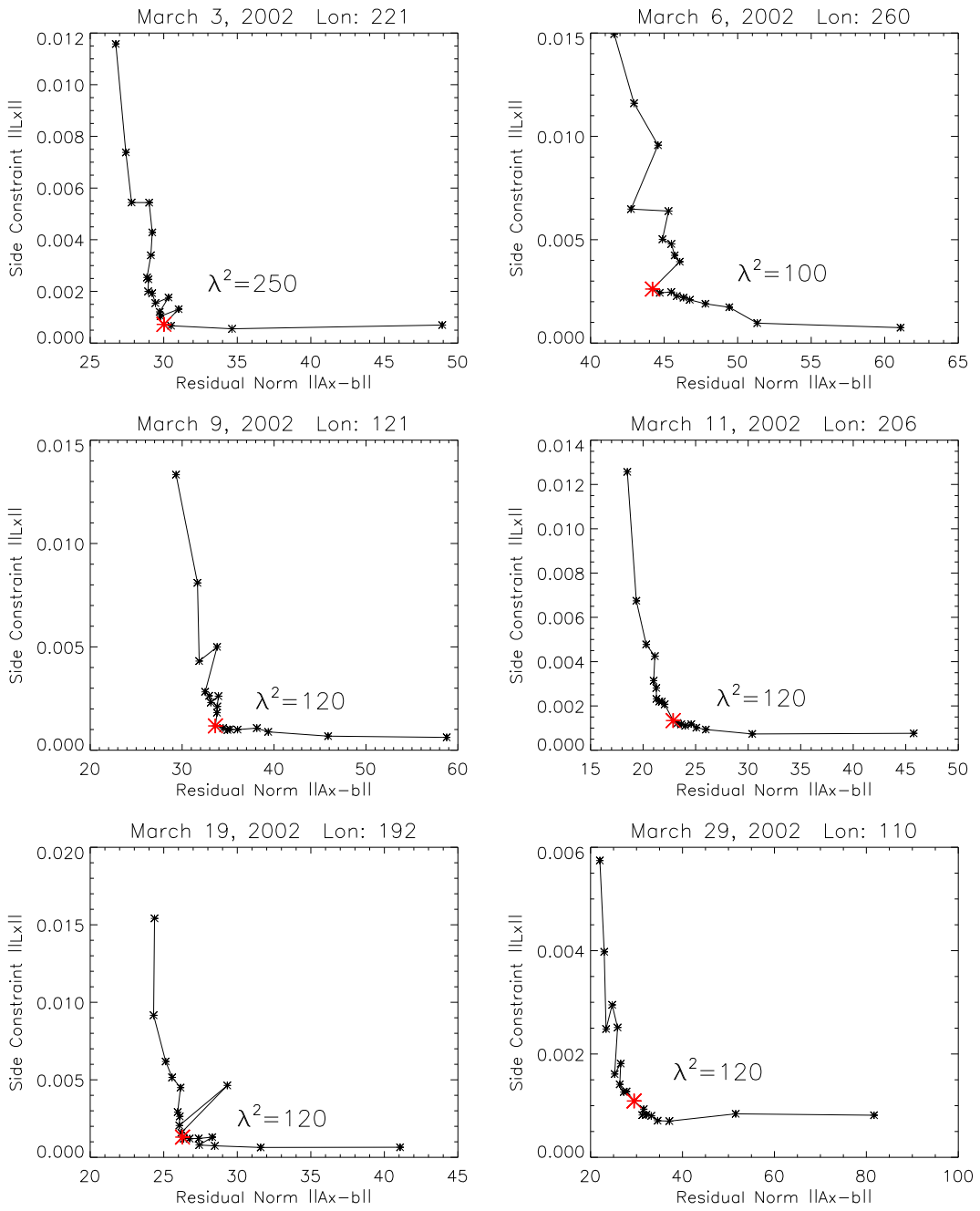
Figure A-1 L-Curves for selected LORAAS night-side passes on March 2002. The regularization parameters are [10,20,30,40,50,60,70,80,90,100,120,140,160,180,200,250,300,600,1000].
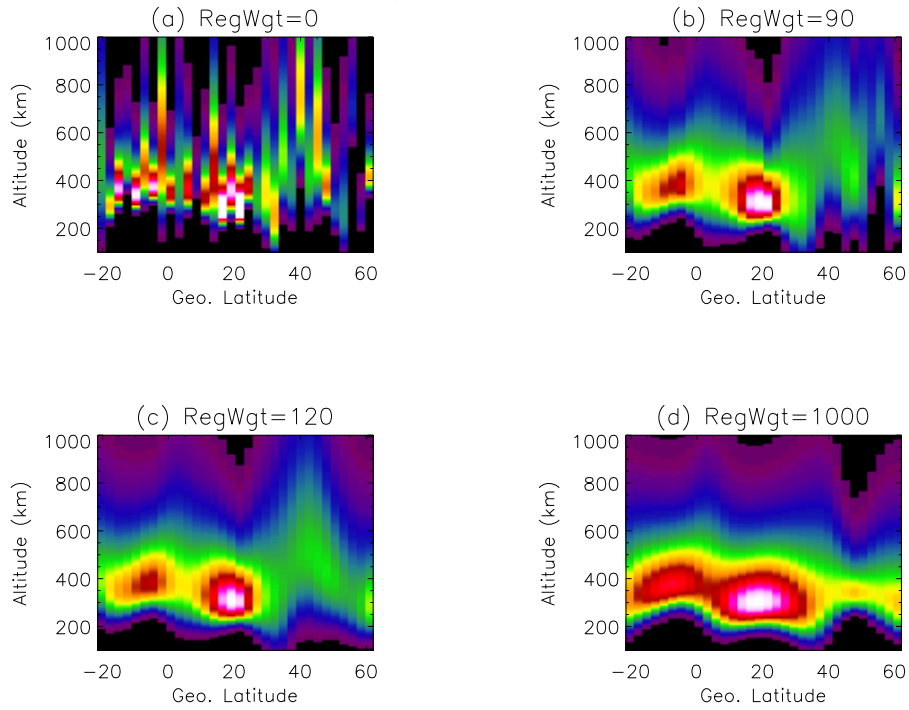
Figure A-2 Example of LORAAS electron density reconstruction with (a) no regularization, (b) near optimal regularization (λ^2=90), (c) optimal regularization (λ^2=120), and (d) extreme regularization (λ^2=1000).

Figure A-3 (a) *NmF2* and (b) *hmF2* for selected regularization parameters.
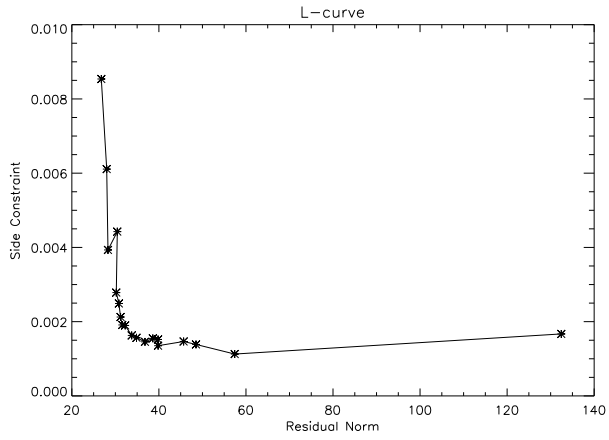
Figure A-4 L-curve for March 11, 2002 at 79˚ longitude.
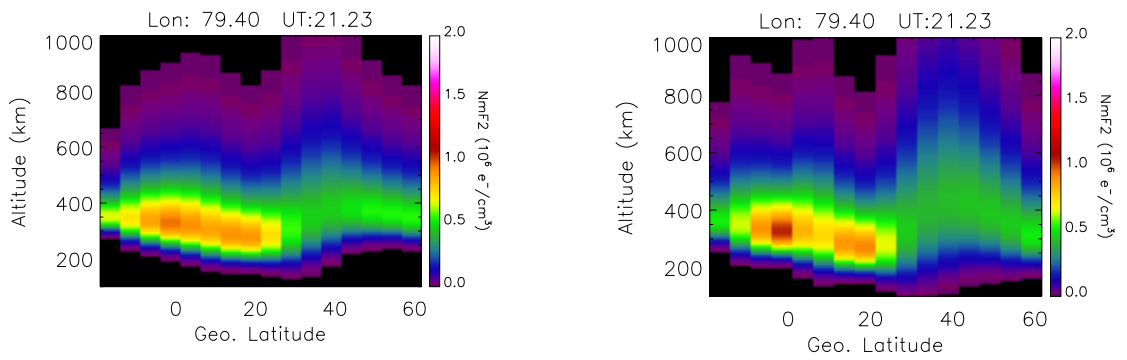
Figure A-5 (a) $\lambda^2 = 120$, (b) $\lambda^2 = 60$.

REFERENCES

REFERENCES

Aarons, J., J.P. Mullen, J.P. Koster, R.F. daSilva, J.R. Medeiros, R.T. Medeiros, A. Bushby, J. Pantoja, J. Lanat, and M.R. Paulson (1980), Seasonal and geomagnetic control of equatorial scintillations in two longitude sectors, *J. Atmos. Terr. Phys*., *42*, 861.

Abdu, M.A., Bittencourt, J.A., and Batista, I.S. (1981), Magnetic declination control of the equatorial F region dynamo electric field development and spread F, *J. Geophys. Res*., *86*, 11443-11446.

Abdu, M.A., I.S. Batista, and J.H.A. Sobral (1992), A new aspect of magnetic declination control of equatorial spread *F* and *F* region dynamo, *J. Geophys. Res.*, *97*, 14897-14904.
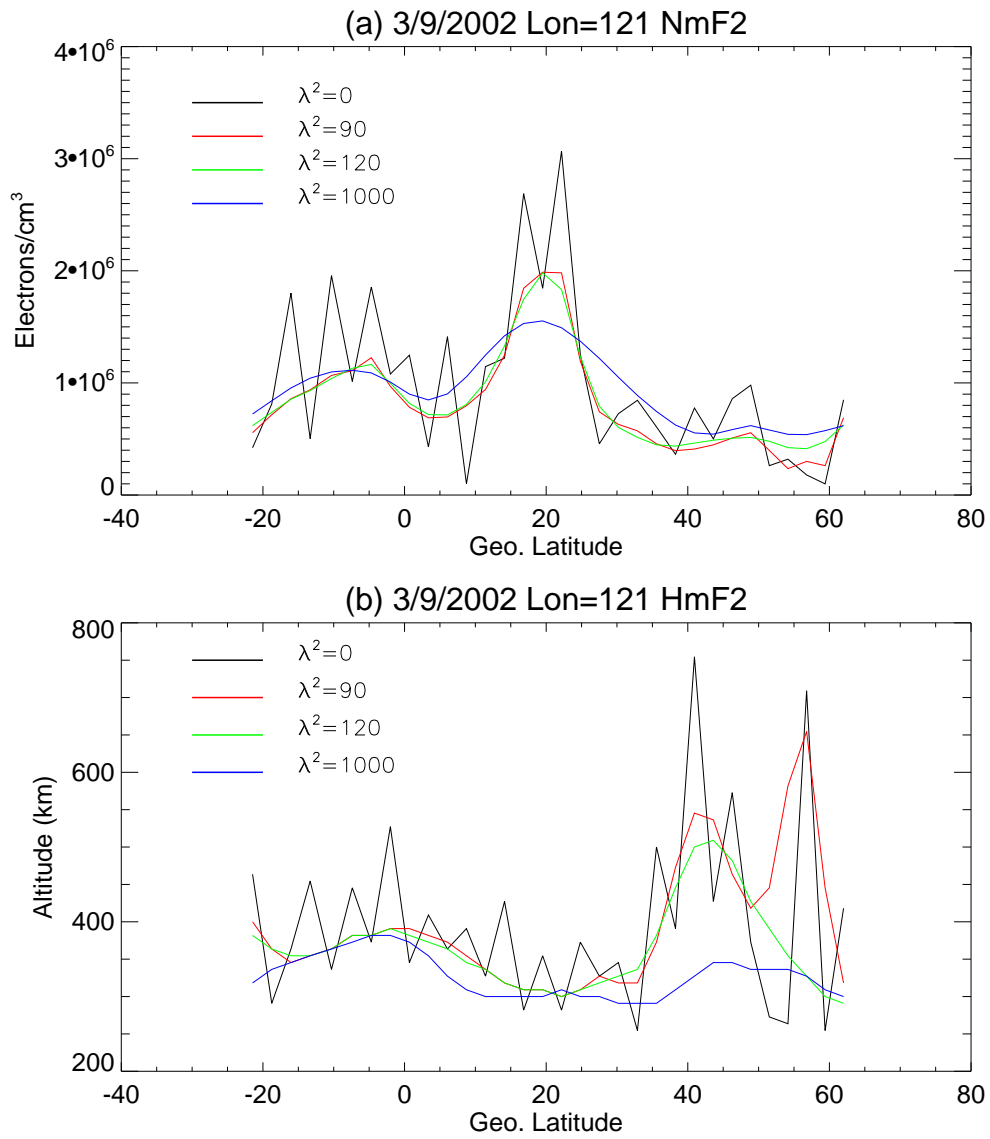
Altadill, D., and E.M. Apostolov (2001), Vertical propagating signatures of wave type oscillations (2- and 6.5-days) in the ionosphere obtained from electron density profiles, *J. Atmos. Solar-Terr. Phys*., *63*, 823-834.

Altadill, D., and E.M. Apostolov (2003), Time and scale size of planetary wave signatures in the ionospheric F region. Role of the geomagnetic activity and mesosphere/lower thermosphere winds, *J. Geophs. Res*., *108*(A11), 1403.

Appleton, E.V. (1946), Two anomalies in the ionosphere, *Nature*, *157*, 691.

Anderson, D.N. (1973a), A theoretical study of the ionospheric *F* region equatorial anomaly- I Theory, *Planet. Space Sci*., *21*, 409-419.

Anderson, D.N. (1973b), A theoretical study of the ionospheric *F* region equatorial anomaly- II Results in the American and Asian sectors, *Planet. Space Sci*., *21*, 421-442.

Anderson, D.N. and R.G. Roble (1981), Neutral wind effects on the equatorial *F*-region ionosphere, *J. Atmos. Terr. Phys*., *43*(8), 835-843.

Anderson, D.N., B. Reinisch, C. Valladares, J. Chau, and O. Veliz (2004), Forecasting the occurrence of ionospheric scintillation activity in the equatorial ionosphere on a day-to-day basis, *J. Atmos. Solar-Terr. Phys*., *66*, 1567-1572.

Anderson, D.N., M. Mendillo, and B. Herniter (1987), A semi-empirical low-latitude ionospheric model, *Radio Science*, *22*(2), 292-306.

Anderson, D.N., and Roble, R.G. (1981), Neutral wind effects on the equatorial *F*-region ionosphere, *J. Atmos. Terr. Phys.*, *43*, 835.

Araujo-Pradere, E.A., T.J. Fuller-Rowell, and D. Bilitza (2004), Ionospheric variability for quiet and perturbed conditions, *Adv. Space Res.*, *34*, 1914-1921.

Aravindakshan, P., and K.N. Iyer (1993), Day-to-day variability in ionospheric electron content, *J. Atmos. Terr. Phys.*, *55*(11/12), 1565-1573.

Aravindan, P., and K.N. Iyer (1990), Day-to-day variability in ionospheric electron content at low latitudes, *Planet. Space Sci.*, *38*(6), 743-750.

Banks, P.M. and G. Kockarts (1973), *Aeronomy. Part B*, Academic Press, New York.

Basu, S., E. Kudeki, Su. Basu, C.E. Valladares, E.J. Weber, H.P. Zengingonul, S. Bhattacharyya, R. Sheehan, J.W. Meriwether, M.A. Biondi, H. Kuenzler, and J. Espinoza (1996), Scintillations, plasma drifts, and neutral winds in the equatorial ionosphere after sunset, *J. Geophys. Res.*, *101*(A12), 26795-26809.

Basu, S., S. Basu, J. Huba, J. Makela, E. Miller, and K. Groves (2006), Modeling of equatorial anomaly development and collapse at dusk observed by TIMED/GUVI, *Eos Trans. AGU*, *87*(52), Fall Meet. Suppl., Abstract SH22A-03.

Basu, S. and Su. Basu (1981), Equatorial Scintillations – A review, *J. Atmos. Terr. Phys.*, *43*, 473.

Basu, Su. and S. Basu (1985), Equatorial Scintillations: Advances since ISEA-6, *J. Atmos. Terr. Phys.*, *47*, 753-768.

Batista, I.S., Abdu, M.A., and Bittencourt, J.A. (1986), Equatorial F-region vertical plasma drifts: seasonal and longitudinal asymmetries in the American sector, *J. Geophys. Res.*, *91*, 12055-12064.

Bauer, S.J. (1973), *Physics of Planetary Ionospheres*, Springer-Verlag, New York.

Bevington, P.R. (1969), *Data Reduction and Error Analysis for the Physical Sciences*, McGraw Hill, New York.

Bilitza, D. (1990), International Reference Ionosphere 1990, *NSSDC/WDC-A-R&S 90-20*, Natl. Space Sci. Data Center., Greenbelt, MD.

Bilitza, D., O.K. Obrou, J.O. Adeniyi, and O. Oladipo (2004), Variability of foF2 in the equatorial ionosphere, *Adv. Space Res.*, *34*, 1901-1906.

Budzien, S.A., K.F. Dymond, S.E. Thonnard, A.C. Nicholas, D.M. Diez, and R.P. McCoy (2002), On-orbit characterization and performance of the HIRAAS instruments aboard ARGOS: LORAAS sensor performance, *Proc. SPIE*, 4485, 349-360.

Caton, R.G., W.J. McNeil, K.M. Groves, and S. Basu (2004), GPS proxy model for real-time UHF satellite communication scintillation maps from the Scintillation Network Decision Aid (SCINDA), *Radio Science*, *39*, RSIS22, doi:10.1029/2002RS002821.

Chandra, S., E.I. Reed, R.R. Meier, C.B. Opal, and G.T. Hicks (1975), Remote sensing of the ionospheric *F* layer by use of O I 6300-Å and O I 1356-Å Observations, *J. Geophys. Res.*, *80*(16), 2327-2332.

Chamberlain, J.W. and Hunten, D.M. (1987), *Theory of Planetary Atmospheres: An Introduction to Their Physics and Chemistry,* 2nd ed., Elsevier, New York.

Chapman, S. (1931), The absorption and dissociative or ionizing effect of monochromatic radiation in an atmosphere on a rotating earth, *Proc. Phys. Soc.*, *43*(1), 26-45; The absorption and dissociative or ionizing effect of monochromatic radiation in an atmosphere on a rotating earth. II. Grazing incidence, *Proc. Phys. Soc.*, *43*(5), 483-501.

Christensen, A.B., L.J. Paxton, S. Avery, J. Craven, G. Crowley, D.C. Humm, H. Kil, R.R. Meier, C. –I. Meng, D. Morrison, B.S. Ogorzalek, P. Straus, D.J. Strickland, R.M. Swenson, R.L. Walterscheid, B. Wolven, and Y. Zhang (2003), Initial observations with the Global Ultraviolet Imager (GUVI) in the NASA TIMED satellite mission, *J. Geophys. Res.*, *108*(A12), 1451, doi:10.1029/2003JA009918.

Coker, C., E.E. Henderlight, K.F. Dymond, S.E. Thonnard, S.E. McDonald, A.C. Nicholas, S.A. Budzien, and R.P. McCoy (2004), Comparison of ionospheric observations from UV limb scans and radar altimetry, *Radio Sci.*, *39*, RS6003, doi:10.1029/2003RS003012.

Coley, W.R., J.P. McClure, and W.B. Hanson (1990), Equatorial fountain effect and dynamo drift signatures from AE-E observations, *J. Geophys. Res.*, *95*, 21285-21290.

de la Beaujardière, O., L. Jeong, B. Basu, S. Basu, T. Beach, P. Bernhardt, W. Burke, K. Groves, R. Heelis, R. Holzworth, C. Huang, D. Hunton, M. Kelley, R. Pfaff, J. Retterer, F. Rich, M. Starks, P. Strauss, and C. Valladares (2004), C/NOFS: A Mission to forecast scintillations, *J. Atmos. Solar-Terr. Phys.*, *66*, 1573-1591.

DeMajistre, R., L.J. Paxton, D. Morrison, and J.-H. Yee (2004), Retrievals of nighttime electron density from Thermosphere Ionosphere Mesosphere Energetics and Dynamics (TIMED) mission Global Ultraviolet Imager (GUVI) measurements, *J. Geophys. Res.*, 109, A05305, doi:10.1029/2003JA010296.

Deminova, G.F. (2003), Fine structure of foF2 longitudinal distribution in the night-time low-latitude ionosphere derived from Intercosmos-19 topside sounding data, *Adv. Space Res.*, *31*(3), 531-536.

Devasia, C.V., N. Jyoti, K.S.V. Subbarao, K.S. Viswanathan, D. Tiwari, and R. Sridharan (2002), On the plausible linkage of thermospheric meridional winds with the equatorial spread F, *J. Atmos. Solar-Terr. Phys.*, *64*, 1-12.

Dymond, K.F., and R.P. McCoy (1993), Ultraviolet spectrographs for thermospheric and ionospheric remote sensing, in *Small Satellite Technology and Applications III*, edited by B.J. Horias, *Proc. SPIE Int. Soc. Opt. Eng.*, *1940*, 117-127.

Dymond, K.F., and R.J. Thomas (2001), An algorithm for inferring the two-dimensional structure of the nighttime ionosphere from radiative recombination measurements, *Radio Sci.*, *36*(5), 1241-1254.

Dymond, K.F., S.A. Budzien, A.C. Nicholas, S.E. Thonnard, R.P. McCoy, and R.J. Thomas (2001), Electron densities determined by inversion of ultraviolet limb profiles, *J. Geophys. Res.*, *106*(A12), 30,315-30,322.

Emmert, J.T. (2001), Climatology of upper thermospheric daytime neutral winds from satellite observations, PhD Doctoral Dissertation, Utah State University, Logan, UT.

England, S.L., T.J. Immel, E. Sagawa, S.B. Henderson, M.E. Hagan, S.B. Mende, H.U. Frey, C.M. Swenson, and L.J. Paxton (2006), Effect of atmospheric tides on the morphology of the quiet time, postsunset equatorial ionospheric anomaly, *J. Geophys. Res.*, *111*, A10S19, doi:10.1029/2006JA011795.

Farley, D.T., E. Bonelli, B.G. Fejer, and M.F. Larsen (1986), The prereversal enhancement of the zonal electric field in the equatorial ionosphere, *J. Geophys. Res.*, *91*(A12), 13723-13728.

Fejer, B.G. (1997), The electrodynamics of the low-latitude ionosphere: recent results and future challenges, *J. Atmos. Solar-Terr. Phys.*, *59*, 1465.

Fejer, B.G., E.R. de Paula, L. Scherliess, and I.S. Batista (1996), Incoherent scatter radar, ionosonde, and satellite measurements of equatorial F region vertical plasma drifts in the evening sector, *Geophys. Res. Lett.*, *23*(14), 1733, doi:10.1029/96GL01847.

Fejer, B.G., E.R. de Paula, R.A. Heelis, and W.B. Hanson (1995), Global equatorial ionospheric vertical plasma drifts measured by the AE-E satellite, *J. Geophys. Res*, *100*(A4), 5769-5776.

Fejer, B.G. and L. Scherliess (2001), On the variability of equatorial F-region vertical plasma drifts, *J. Atmos. Terr. Phys.*, *63*, 893-897.

Fejer, B.G., L. Scherliess, and E.R. de Paula (1999), Effects of the Vertical Plasma Drift Velocity on the Generation and Evolution of Equatorial Spread F, *J. Geophys. Res.*, *104,* 19859 – 19869.

Fejer, B.G., and M.C. Kelley (1980), Ionospheric irregularities, *Rev. Geophys. Space Phys.*, *18*, 401-450.

Ferguson, E.E. (1971), D-Region Ion Chemistry, *Rev. Geophys. Space Phys.*, *9*, 997-1008.

Fesen, C.G. (1997), Theoretical effects of tides and auroral activity on the low latitude ionosphere, *J. Atmos. Solar-Terr. Phys.*, *59*(13), 1521-1532.

Forbes, J.M. (1995), Tidal and planetary waves, in *The Upper Mesosphere and Lower Thermosphere: a Review of Experiment and Theory*, Geophysical Monograph Series, *87*, edited by R.M. Johnson and T.L. Killeen, American Geophysical Union, Washington DC, 67-87.

Forbes, J.M., J. Russell, S. Miyahara, X. Zhang, S. Palo, M. Mlynczak, C.J. Mertens, and M.E. Hagan (2006), Troposphere-thermosphere tidal coupling as measured by the SABER instrument on TIMED during July-September 2002, *J. Geophys. Res.*, *111*, A10S06, doi:10.1029/2005JA011492.

Forbes, J.M., R.G. Roble, and C.G. Fesen (1993), Acceleration, heating and compositional mixing of the thermosphere due to upward propagating tides, *J. Geophys. Res.*, *98*, 311-322.

Forbes, J.M., S.E. Palo, and X. Zhang (2000), Variability of the ionosphere, *J. Atmos. Solar-Terr. Phys.*, *62*, 685-693.

Forbes, J.M., and X. Zhang (1997), Quasi 2-day oscillations of the ionosphere: A statistical study, *J. Atmos. Solar-Terr. Phys.*, *59*(9), 1025-1034.

Fuller-Rowell, T.J., and D. Rees (1980), A three-dimensional and time-dependent global model of the thermosphere, *J. Atmos. Sci.*, *37*, 2545-2567.

Gelb, A. (1974), *Applied Optimal Estimation*, MIT Press, Cambridge, MA.

Gombosi, T. (1998), *Physics of the Space Environment*, Cambridge University Press, Cambridge, UK.

Groves, K.M., S. Basu, E.J. Weber, M. Smitham, H. Kuenzler, C.E. Valladares, R. Sheehan, E. MacKenzie, J.A. Secan, P. Ning, W.J. McNeill, D.W. Moonan, and M.J. Kendra (1997), Equatorial scintillation and systems support, *Radio Science*, *32*(5), 2047-2064.

Hansen, P.C. (1992), Numerical tools for analysis and solution of Fredholm integral equations of the first kind, *Inverse Problems*, *8*, 849-872.

Hanson, W.B., and R.J. Moffett (1966), Ionization transport effects in the equatorial *F* region, *J. Geophys. Res.*, *71*(23), 5559-5572.

Häusler, K., H. Lühr, S. Rentz, and W. Köhler (2007), A statistical analysis of longitudinal dependences of upper thermospheric zonal winds at dip equator latitudes derived from CHAMP, *J. Atmos. Solar-Terr. Phys.*, *69*, 1419-1430, doi:10.1016/j.jastp.2007.04.004.

Heath, M.T. (1997), *Scientific Computing: An Introductory Survey*, McGraw-Hill, New York.

Hedin, A. E., E.L. Fleming, A.H. Manson, F.J. Scmidlin, S.K. Avery, R.R. Clark, S.J. Franke, G.J. Fraser, T. Tsunda, F. Vial and R.A. Vincent (1996), Empirical Wind Model for the Upper, Middle, and Lower Atmosphere, *J. Atmos. Terr. Phys., 58*, 1421.

Heelis, R.A., P.C. Kendall, R.J. Moffett, D.W. Windle, and H. Rishbeth (1974), Electrical coupling of the E- and F-region and its effects on F-region drifts and winds, *Planet. Space Sci.*, *22*, 743.

Henderson, S.B., C.M. Swenson, A.B. Christensen, and L.J. Paxton (2005), Morphology of the equatorial anomaly and equatorial plasma bubbles using image subspace analysis of Global Ultraviolet Imager data, *J. Geophys. Res.*, *110*, A11306, doi:10.1029/2005JA011080.

Hocke, K., and K. Schlegel (1996), A review of atmospheric gravity waves and traveling ionospheric disturbances: 1982 – 1995, *Ann. Geophys.*, *14*(9), 917-940.

Huba, J. D., G. Joyce, and J.A. Fedder (2000), SAMI2 (Sami2 is Another Model of the Ionosphere): A New Low-latitude Ionosphere Model, *J. Geophys. Res., 105*(A10), 23035-23053.

Hysell, D.L., and J.D. Burcham (2002), Long term studies of equatorial spread *F* using the JULIA radar at Jicamarca, *J. Atmos. Solar-Terr. Phys.*, *64*, 1531-1543.

Imel, D.A. (1994), Evaluation of TOPEX/Poseidon dual frequency ionosphere correction, *J. Geophys. Res.*, *99*, 24895-24906.

Immel, T.J., S.B. Mende, H.U. Frey, and L.M. Peticolas (2003), Determination of low latitude plasma drift speeds from FUV images, *Geophys. Res. Lett.*, *30*(18), 1945, doi:10.1029/2003GL017573.

Immel, T.J., E. Sagawa, S.L. England, S.B. Henderson, M.E. Hagan, S.B. Mende, H.U. Frey, C.M. Swenson, and L.J. Paxton (2006), Control of equatorial ionospheric morphology by atmospheric tides, *Geophys. Res. Lett.*, *33*, L15108, doi:10.1029/2006GL026161.

Ivers, D., R. Stening, J. Turner, and D. Winch (2003), Equatorial electrojet from Ørsted scalar magnetic field observations, *J. Geophys. Res.*, *108*(A2), 1061, doi:10.1029/2002JA009310.

Jadhav, G., M. Rajaram, and R. Rajaram (2002), A detailed study of equatorial electrojet phenomenon using Ørsted satellite observations, *J. Geophys. Res.*, *107*(A8), 1175, doi:10.1029/2001JA000183.

Julienne, P.S., and J. Davis (1976), Cascade and radiation trapping effects on atmospheric atomic oxygen emission excited by electron impact, *J. Geophys. Res.*, *81*(7), 1397-1403.

Kelley, M.C., M.F. Larsen, C.A. LaHoz, and J.P. McClure (1981), Gravity wave initiation of equatorial spread F: A case study, *J. Geophys Res.*, *84*, 1898.

Kelley, M.C. (1989), *The Earth's Ionosphere: Plasma Physics and Electrodynamics, Int. Geophys. Ser., vol. 43*, Academic Press, San Diego, CA.

Kil, H., S.-J. Oh, M.C. Kelley, L.J. Paxton, S.L. England, E. Talaat, K.-W. Min, and S.-Y. Su (2007), Longitudinal structure of the vertical $\mathbf{E} \times \mathbf{B}$ drift and ion density seen from ROCSAT-1, *Geophys. Res. Lett.*, *34*, L14110, doi:10.1029/2007GL030018.

Krasnov, V.M., Ya.V. Drobzheva, J.E.S. Venart, and J. Lastovicka (2003), A re-analysis of the atmospheric and ionospheric effects of the Flixborough explosion, *J. Atmos. Solar-Terr. Phys.*, *65*, 1205-1212.

Laštovička, J. (2006), Forcing of the ionosphere by waves from below, *J. Atmos. Solar-Terr. Phys.*, *68*, 479-497.

Lin, C.H., W. Wang, M.E. Hagan, C.C. Hsiao, T.J. Immel, M.L. Hsu, J.Y. Liu, L.J. Paxton, T.W. Fang, and C.H. Liu (2007), Plausible effect of atmospheric tides on the equatorial ionosphere observed by the FORMOSAT-3/COSMIC: Three-dimensional electron density structures, *Geophys. Res. Lett.*, *34*, L11112, doi:10.1029/2007GL029265.

Lyon, A.J. and L. Thomas (1963), The *F2*-region equatorial anomaly in the African, American and East Asian sectors during sunspot maximum, *J. Atmos. Terr. Phys.*, *25*, 373-386.

Maruyama, T., and N. Matuura (1984), Longitudinal variability of annual changes in activity of equatorial spread F and plasma bubbles, *J. Geophys. Res.*, *89*, 10903-10912.

McCoy, R.P., K.F. Dymond, G.G. Fritz, S.E. Thonnard, R.R. Meier, and P.A. Regeon (1992), Far- and extreme-ultraviolet limb imaging spectrograph for the DMSP satellites, in *Instrumentation for Planetary and Terrestrial Atmospheric Remote Sensing*, edited by S. Chakrabarti and A.B. Christensen, *Proc. SPIE Int. Soc. Opt. Eng.*, *1745*, 310-321.

McCoy, R.P., K.F. Dymond, G.G. Fritz, S.E. Thonnard, R.R. Meier, and P.A. Regeon (1994), Special Sensor Ultraviolet Limb Imager: An Ionospheric and Neutral Density Profiler for the Defense Meteorological Satellite Program Satellites, *Opt. Eng.*, *33*, 423.

Meier, R.R. (1991), Ultraviolet spectroscopy and remote sensing of the upper atmosphere, *Space Sci. Rev.*, *58*, 1-185.

Meléndez-Alvira, D.J., R.R. Meier, J.M. Picone, P.D. Feldman, and B.M. McLaughlin (1999), Analysis of the oxygen nightglow measured by the Hopkins Ultraviolet Telescope: Implications for ionospheric partial radiative recombination rate coefficients, *J. Geophys. Res.*, *104*, 14901-14914.

O'Leary, D.P. (2001), Near-Optimal Parameters for Tikhonov and Other Regularization Methods, *SIAM J. Sci. Comput.*, *23*(4), 1161-1171.

Paxton, L.J., C.I. Meng, G.H. Fountain, B.S. Ogorzalek, E.H. Darlington, S.A. Gary, J. Goldsten, S.C. Lee, K. Peacock (1992), SSUSI: An Horizon-to Horizon and Limb Viewing Spectrographic Imager - UV Remote Sensing, *SPIE International Symposium on Optical Applied Science and Engineering, Ultraviolet Technology IV,* SPIE paper 1764-15, Ultraviolet Technology IV.

Philips, D.L. (1962), A technique for the numerical solution of certain integral equations of the first kind, *J. ACM*, *9*, 84-97.

Picone, J. M., A.E. Hedin, D.P. Drob, and A.C. Aikin (2003), NRL-MSISE-00 Empirical Model of the Atmosphere: Statistical Comparisons and Scientific Issues, *J. Geophys. Res.*, doi:10.1029/2002JA009430.

Rastogi, R.G., and S. Alex (1987), Day-to-day variability of ionospheric electron content at low latitudes, *J. Atmos. Terr. Phys.*, *49*(11/12), 1133-1137.

Reinisch, B.W., and X. Huang (1983), Automatic Calculation of Electron Density Profiles from Digital Ionograms. III - Processing of Bottomside Ionograms, *Radio Science*, *18*, 477-492.

Rees, M.H. (1989), *Physics and Chemistry of the Upper Atmosphere*, Cambridge University Press, Cambridge.

Richmond, A.D. (1995), The ionospheric wind dynamo: effects of its coupling with different atmospheric regions, in *The Upper Mesosphere and Lower Thermosphere*: *A Review of Experiment and Theory, Geophysical Monograph Series*, *87*, edited by R.M. Johnson and T.L. Killeen, American Geophysical Union, Washington, DC, 49-65.

Richmond, A.D., and S. Matsushita (1975), Thermospheric response to a magnetic substorm, *J. Geophys. Res.*, *80*, 2839-2850.

Richmond, A.D., S. Matsushita, and J.D. Tarpley (1976), On the production mechanisms of electric currents and fields in the ionosphere, *J. Geophys. Res.*, *81*, 547.

Rishbeth, H. (1971), The F layer dynamo, *Planet. Space Sci.*, *19*, 263.

Rishbeth, H., and M. Mendillo (2001), Patterns of *F*2-layer variability, *J. Atmos. Solar-Terr. Phys.*, *63*, 1661-1680.

Rishbeth, H., and O.K. Garriott (1969), Introduction to Ionospheric Physics, *Int. Geophys. Ser.*, *14*, Academic Press, New York.

Rodger, A.S., and M.J. Jarvis (2000), Ionospheric Research 50 years ago, today and tomorrow, *J. Atmos. Solar-Terr. Phys.*, *62*, 1629-1645.

Rush, C.M., and J. Gibbs (1973), Predicting the day-to-day variability of the mid-latitude ionosphere for application to HF propagation predictions, *AFCRL-TR-73-0335*, Air Force Geophysics Laboratory, Hanscom AFB, MA.

Sagawa, E., T.J. Immel, H.U. Frey, and S.B. Mende (2005), Longitudinal structure of the equatorial anomaly in the nighttime ionosphere observed by IMAGE/FUV, *J. Geophys. Res.*, *110*, A11302, doi:10.1029/2004JA010848.

Scherliess, L., and B.G. Fejer (1999), Radar and satellite global equatorial *F* region vertical drift model, *J. Geophys. Res.*, *104*, 6829.

Schunk, R.W., and A.F. Nagy (2000), *Ionospheres: Physics, Plasma Physics, and Chemistry*, Cambridge University Press, Cambridge, UK.

Schunk, R.W., L. Scherliess, J.J. Sojka, D.C. Thompson, D.N. Anderson, M. Codrescu, C. Minter, T.J. Fuller-Rowell, R.A. Heelis, M. Hairston, and B. Howe (2004), Global Assimilation of Ionospheric Measurements (GAIM), *Radio Science*, *39*, RS1S02, doi:10.1029/2002RS002794.

Stening, R.J. (1981), A two-layer ionospheric dynamo calculation, *Geophys. Res. Lett.*, *86*, 3543-3550.

Thomas, L. (1968), The *F2*-region equatorial anomaly during solstice periods at sunspot maximum, *J. Atmos. Terr. Phys.*, *30*, 1631-1640.

Tikhonov, A.N., and V.Y. Arsenin (1977), *Solutions of Ill-Posed Problems*, Wiley, NY.

Titheridge, J.E. (1995), Winds in the ionosphere – a review, *J. Atmos. Terr. Phys.*, *57*, 1681.

Tsunoda, R.T. (1985), Control of the seasonal and longitudinal occurrence of equatorial scintillations by the longitudinal gradient in integrated *E* region Pedersen conductivity, *J. Geophys. Res.*, *90*, 447-456.

Tsunoda, R.T. (2005), On the enigma of day-to-day variability in equatorial spread F, *Geophys. Res. Lett.*, *32*, L08103, doi:10.1029/2005GL022512.

Valladares, C.E., S. Basu, K. Groves, M.P. Hagan, D. Hysell, A.J. Mazzella Jr., and R.E. Sheehan (2001), Measurement of the Latitudinal Distributions of Total Electron Content during Equatorial Spread *F* Events, *J. Geophys. Res.*, *106*, 29133-29152.

Walker, G.O., J.H.K. Ma, R.G Rastogi, M.R. Deshpande, and H. Chandra (1980), Dissimilar forms of the ionospheric equatorial anomaly observed in East Asia and India, *J. Atmos. Terr. Phys.*, *42*, 629-635.

Walker, G.O., and T. Chan (1970), A study of scintillations at low latitudes during a period from sunspot minimum to sunspot maximum, *J. Geophys. Res.*, *72*, 2517.

Whalen, J.A. (2001), The equatorial anomaly: Its quantitative relation to equatorial bubbles, bottomside spread F, and the $\mathbf{E} \times \mathbf{B}$ drift velocity during a month at solar maximum, *J. Geophys. Res.*, *101*(A12), 29125-29132.

Woodman, R.F. (1970), Vertical drift velocities and east-west electric fields at the magnetic equator, *J. Geophys. Res.*, *75*(31), 6249-6259.

Zalesak, S.T., S.L. Ossakow, and P.K. Chaturvedi (1982), Nonlinear equatorial spread *F*: The effect of neutral winds and background Pedersen conductivity, *J. Geophys. Res.*, *87*, 151.

CURRICULUM VITAE

Sarah E. McDonald graduated from Albert G. Lane Technical High School in Chicago, Illinois in 1986. She received her Bachelor of Arts in Physics from Northwestern University in Evanston, Illinois in 1990 and her Masters of Arts in Physics from Johns Hopkins University in Baltimore, Maryland in 1992. She has been a research physicist at the Naval Research Laboratory in Washington D.C. since 1998.